KFKI-2002-02/G
REPORT

Z. HÓZER
P. WINDBERGER
I. NAGY
L. MARÓTI
L. MATUS
M. HORVÁTH
A. PINTÉR

CODEX-AIT-1 EXPERIMENT: CORE DEGRADATION TEST UNDER AIR INGRESS

Hungarian Academy of Sciences
CENTRAL
RESEARCH
INSTITUTE FOR
PHYSICS
BUDAPEST

CODEX-AIT-1 EXPERIMENT: CORE DEGRADATION TEST UNDER AIR INGRESS

Z. Hózer, P. Windberg, I. Nagy, L. Maróti, L. Matus, M. Horváth, A. Pintér
KFKI Atomic Energy Research Institute
H-1525 Budapest, P.O.Box.49, Hungary

A. Czitrovszky, P. Jani
Research Institute for Solid State Physics and Optics
H-1525 Budapest, P.O.Box.49, Hungary

Abstract

Z. Hózer, P. Windberg, I. Nagy, L. Maróti, L. Matus,
M. Horváth, A. Pintér, A. Czitrovszky, P. Jani:
CODEX-AIT-1 EXPERIMENT: CORE DEGRADATION TEST UNDER AIR INGRESS

The CODEX (COre Degradation EXperiment) facility was used to provide experimental data on the behaviour of real fuel bundles under air oxidation conditions. The CODEX-AIT-1 experiment was carried out with electrically heated 9-rod PWR type bundle. Temperature, flowrate, pressure measurements were recorded during the tests. Pyrometers and high temperature thermocouples were used for temperature measurements. Aerosol release was measured using on-line particle counters and cascade impactors. The test indicated the acceleration of oxidation phenomena and core degradation processes during the late phase of the vessel melt through accident, when the air can have access to the residual fuel bundles in the reactor core. The degradation process was accompanied with zirconium-nitride formation and release of U-rich aerosol.

Kivonat

Hózer Z., Windberg P., Nagy I., Maróti L., Matus L.,
Horváth M., Pintér A., Czitrovszky A., Jani P.:
A CODEX-AIT-1 KÍSÉRLET: ZÓNASÉRÜLÉSES MÉRÉS LÉGBETÖRÉSSEL

A CODEX (COre Degradation EXperiment) berendezésben fűtőelemkötegek viselkedését vizsgáltuk levegős oxidációs körülmények között. A CODEX-AIT-1 mérésben elektromosan fűtött PWR típusú köteget használtunk. A hőmérséklet, nyomás és forgalom adatokat folyamatosan gyűjöttük a mérés során. Pirométereket és magas hőmérsékletű termoelemeket használtunk a hőmérséklet mérésekhez. Az aeroszol kibocsátás mérését on-line részecskeszámláló és kaszkád aeroszol csapdák tették lehetővé. A mérés jelezte, hogy az oxidációs folyamatok és a zónasérülés felgyorsul a súlyos baleset utolsó szakaszában, amikor a tartályfenék átolvadása után levegő áramlik be és lép reakcióba a zóna szélén még ép fűtőelemekkel. A zónasérülést cirkónium-nitrid képződés és uránban gazdag aeroszolok kibocsátása kísérte.

Contents

List of tables

List of figures

1. INTRODUCTION

The degradation of the normal heat transfer and fluid flow conditions in a nuclear reactor can lead to severe accident conditions characterised by the interaction of core materials at high temperature. The oxidation of metal components accelerates in the presence of air, which can enter the reactor after the failure of the bottom head.

The TMI-2 accident examination showed that even after the relocation of the central core region into the lower plenum and molten pool formation, the peripheral fuel assemblies remained intact. It can be expected that after vessel failure large mass of core components remains in the reactor vessel. Following the lower head failure air can enter the primary system and the character of the degradation process can be changed compared to steam atmosphere conditions. The interaction of air with Zr alloys and UO_2 pellets can strongly affect the evolution of severe accident scenarios through heat generation, increased core degradation and fission product release. The interaction of air with fission products can influence the radiological source term due to the volatilisation of ruthenium oxide [1]. The Zr oxidation in air is characterised by faster reaction kinetics, lower heat transfer to fluid and it produces for 85% more heat than in steam.

The consequences of air oxidation on the core degradation and fission product release in a reactor case can not be well estimated today. The CODEX-AIT-1 air ingress test presented here was the first integral test with air ingress conditions. The experimental programme was carried out in the OPSA project of the 4th EU Framework Programme [2].

2. THE CODEX FACILITY

The CODEX facility was built in 1995 for the investigation of the behaviour of small fuel bundles under severe accident conditions. The first test series was devoted to the experimental study of VVER type fuel assemblies. Escalation in steam and quenching at high temperatures were analysed in 7-rod hexagonal bundles made of VVER materials.

The main components of the facility are shown in Fig.1 and the most important parameters are summarised in Table 1. The details of aerosol sampling are given in the picture of the upper part of the bundle and of the cooler (Fig. 3). Fig. 4 presents the vertical view of the heated and unheated (central) rods and Fig. 2. the horizontal cross section of the bundle.

In the Air Ingress Tests (AIT) 9-rod PWR type bundles were used. The rods were arranged on a square lattice, 8 peripheral rods were electrically heated with tungsten bars (Fig. 2). The central rod was not heated, it was used for instrumentation. Two spacer grids were applied to fix the bundle. The heated length of the bundle was 600 mm (Fig. 4). The cladding material was Zircaloy, the shroud part was made of a 2 mm thick Zr2%Nb alloy. Inside of the fuel rods annular UO_2 pellets were placed between the heater bars and the cladding. Around the shroud ZrO_2 thermal insulation was added.

The test section was connected to the preheater and to the cooler sections as coolant inlet and outlet respectively (Fig. 1). An additional junction was connected to the bottom part of the bundle to inject cold (room temperature) air. The preheater unit was able to supply either hot gases or steam to the test section. The off-gas streaming out of the test section was cooled down by the cooler/condenser unit and before releasing it into the atmosphere it was conducted through an aerosol trap and filtered by a special system. For the investigation of the aerosol release a cascade impactor system was connected to the upper plenum of the cooler (Fig. 3) and two pipelines allowed the continuous measurement of aerosols by means of laser particle counters.

The instrumentation of the facility consisted of the measurements of the operational parameters as heating power, flowrates, temperatures, levels and pressures. Thermocouples were placed in several positions in the heat insulation material, on the heat shield, on the external surface of the shroud, on the fuel rods and inside of the central (unheated) rod (Table 2). Two pyrometers were located at 450 and 535 mm elevations. Flowmeters, pressure transducers and analog multiplayer using shunt current and total voltage were applied.

The on-line aerosol measurements were made with two Laser Airborne Particle Counters (APC-03-2 and PAPC-03-2). The measuring principle of these airborne particle counters is based on laser light scattering. The data evaluation system comprises opto-electronic detecting and filtering, multichannel signal analysing interface and lap-top PC. The velocity of the gas stream was about 1 l/s. The APC method resulted in particle concentrations directly, dividing the light scattering signals into 6 ranges, 0.3-0.5, 0.5-1, 1-3, 3-5, 5-10 and >10 μm interval. The particle concentrations could be detected up to $5x10^6$ particles/l values.

In the CODEX-AIT experiments the sampling head of the PAPC-03-2 counter was mounted on the top of the cooler using a ~20 cm long copper tube. The APC-03-2 counter was placed out of the container and coupled with a 2 m long cable to the cooler head.

Bundle type:	PWR
Bundle size:	9 rods
Number of heated rods:	8
Number of unheated rods:	1
Pitch:	14.3 mm
Rod outside diameter:	10.75 mm
Cladding thickness:	0.725 mm
Cladding material:	Zircaloy-4
Heater material:	Tungsten (W)
Heater length:	600 mm
Heater diameter:	6 mm
Fuel pellets - heated rods:	UO_2 annular pellets
Fuel pellets - unheated rod:	UO_2 annular pellets
Pellet outer diameter:	9.1 mm
U-235 enrichment:	0.2%
Pellet stack:	600 mm
Grid spacer material:	Zircaloy-4
Grid spacer location:	lower: -15 mm, upper: 535 mm
Shroud material:	Zr2%Nb
Shroud wall thickness:	2 mm
Shroud inside dimensions:	48 x 48 mm
Shroud insulation material:	ZrO_2 fibre
Shroud insulation thickness:	19 mm
Shroud insulation elevation:	-50 - 620 mm
Max. inlet argon, steam and air temperature	800 ºC
Max. inlet argon flow:	10 g/s
Max. argon + 25%O_2 flow:	10 g/s
Max. air flow:	5 g/s
Max. system pressure	3.5 bar
Max. power of tungsten heaters	5 kW
Max power of steam generator	9 kW
Max. power of superheater	3 kW

Table 1 Main characteristics of the CODEX-AIT facility

The following parameters were measured and recorded during the experiments:

- central (unheated) rod temperatures
- heated rod temperatures, shroud temperatures
- heat insulation temperatures, heat shield temperatures
- steam, air, argon flowrates
- gas inlet/outlet temperatures at the test section, cooler inlet/outlet temperatures
- water temperature in steamgenerator, pyrometer temperature measurements

- electric power, system pressure, argon, air and impactor valve positions.

Elevation, mm	Heat insulation outside R=130mm	Heat shield R=80mm	Shroud outside	Heated rod cladding	Unheated (central) rod
760					NiCr-Ni
570			W- WRe	W- WRe	W- WRe
535	NiCr-Ni	NiCr-Ni		W- WRe	W- WRe
450	NiCr-Ni	NiCr-Ni	W- WRe	W- WRe	W- WRe
375					W- WRe
300	NiCr-Ni	NiCr-Ni	Pt-PtRh	Pt-PtRh	W- WRe
150	NiCr-Ni	NiCr-Ni	NiCr-Ni	NiCr-Ni	NiCr-Ni
50	NiCr-Ni	NiCr-Ni	NiCr-Ni		NiCr-Ni
0					NiCr-Ni
-20					NiCr-Ni
-350					NiCr-Ni

Table 2 Position and material of thermocouples in the test section

3. THE CODEX EXPERIMENTAL PROGRAMME

In AEKI an experimental programme was initiated focusing on the high temperature behaviour of VVER fuel and core materials. The interactions of Zr1%Nb cladding with UO_2 pellet, stainless steel spacer and boron steel absorber were studied in small scale separate effect tests [3]. On the basis of the experience gained in these tests the CODEX integral test facility was constructed to continue this work under more prototypic conditions.

First the capabilities of the facility were demonstrated carrying out the CODEX-1 experiment with Al_2O_3 pellets. The test section was heated up with argon, then the electric power was increased. When the rod bundle degradation was indicated by temperature measurements, the power was switched off and the section was cooled down by argon. The post-test examination showed that the rod bundle partially damaged, the further melting was stopped in time. So the facility proved to be applicable to the experimental analysis of controlled core degradation processes.

In the second experiment similar procedures were taken, but the Al_2O_3 pellets were replaced with UO_2 [4,5]. The CODEX-3/1 and CODEX-3/2 experiments were performed with quick water cooling [6,7]. Air ingress conditions were simulated in the AIT-1 and AIT-2 tests with PWR fuel rods [2]. The B4C test was devoted to the examination of control rod degrdadation and gas production during a severe reactor accident. The main parameters of the test matrix are given in Table 3.

Test	Bundle type	Pellet	Year	Test type
CODEX-1	7-rod VVER	Al_2O_3	1995	scoping test
CODEX-2	7-rod VVER	UO_2	1995	escalation and slow cooling down
CODEX-3/1	7-rod VVER	UO_2	1996	water quench at 1150 ^oC
CODEX-3/2	7-rod VVER	UO_2	1997	water quench at 1500 ^oC
CODEX-AIT-1	9-rod PWR	UO_2	1998	air ingress
CODEX-AIT-2	9-rod PWR	UO_2	1999	steam oxidation and air ingress
CODEX-B4C	7-rod VVER	UO_2,B_4C	2001	control rod degradation

Table 3 Main parameters of CODEX test matrix

4. COMMISSIONING TEST

When a complex integral facility is put into operation, generally a commissioning test is performed, because of at least two reasons. Firstly, during the commissioning test the adequate functioning of all the operational and experimental measurement channels is tested. Secondly, the thermal properties of the complex test facility cannot be determined from the data of the components, but it should be extracted from the results of the commissioning test.

The commissioning test at the CODEX facility equipped with the AIT-1 test section was accomplished according to the common proposal of the experimental and analytical teams, i.e.

- pre-heat in argon at 700 ^oC with electrical power for 1 hour,
- step change in power to reach maximum clad temperature of 750 ^oC, hold for 1 hour,
- step change in power to reach maximum clad temperature of 850 ^oC, hold for 1 hour,
- step change in power to reach maximum clad temperature of 1050 ^oC, hold for 1 hour,
- power off, cool in argon.

The most important results of the commissioning test are the temperature histories at the different points of the test section. The results have been successfully applied for fitting the heat capacities and conductivities of the facility to get correct heat balance. The time variation of the measurement data is illustrated in Figs. 5-8. The commissioning test was carried out with the CODEX-AIT-1 bundle. The available measurement data makes possible the tuning of heat loss simulation and the checking of the system thermal response.

5. THE CODEX-AIT-1 EXPERIMENT

Air ingress is generally preceded by steam oxidation of the cladding. The resulting oxide layer depending on its thickness provides different degrees of protection against further oxidation. Based on some supporting pre-oxidation experiments and on the results of pretest calculations, it has been decided to continue the pre-oxidation in the first test only up to 50 μm oxide layer thickness. To avoid H_2 generation, the pre-oxidation was made by Ar+25%O_2 gas mixture. The aim of the experiment was to see how the temperature escalation will go on in the test bundle containing fuel rods oxidized up to 50 μm oxide layer thickness. The termination of the test and cooling down of the test bundle were foreseen at 2100 °C maximum cladding temperature.

The CODEX-AIT-1 started with a heating-up period and stable temperature distribution was reached with 900 °C maximum rod temperature. The pre-oxidation phase was initiated with the reduction of argon flow and injection of oxygen at the same time. Strong temperature excursion (Figs. 15-19) took place during the pre-oxidation which could be stopped only by switching off the power (Fig. 53) and stopping the oxygen injection (Fig.5). This temperature maximum was ~1500 ^{o}C on the upper spacer grid and close to 2000 ^{o}C on some fuel rods in the upper part of the bundle. After this unexpected transient a stabilisation period took place with power regulation in argon atmosphere.

The air ingress phase was initiated at ~900 ^{o}C maximum temperature with the injection of room temperature air. Argon injection was stopped and power was kept constant. The cold air cooled down the lower part of the bundle (Figs. 13-15), but in the upper part lead to temperature excursion (Figs. 17-19). 2000 ^{o}C was reached on the upper spacer grid (Fig. 19) and on some fuel rods, when the cooling down phase was initiated by switching of power, stopping air injection and injecting cold argon.

The time variation of the most important parameters during the test is shown in Figs. 9-59. The measured data recorded by the data acquisition system have been converted into the form suitable for further elaboration and have been sent to the analytical teams for post test calculations.

6. BUNDLE POST-TEST EXAMINATION

The AIT-1 bundle suffered limited damage, the rod-like structure remained almost intact. Failure of some rods was observed close to the top of the bundle, the spacer grid was heavily oxidised and broken. The upper spacer was oxidised and fragmented in a larger extent than the cladding. The highest temperature area was at about 535 mm elevation. The value of maximum temperature can be estimated from the effect that the β-phases were melted and escaped but the α-phase remained back. It limits the temperature between 1800 and 2100°C. The oxide layer did not keep the melted β-phase, it escaped through small cracks. The β-phase has flown out even from cladding area where the α-phase was advanced into the β-scale on the crystal boundaries. It proves the low viscosity of melted β-phase, as well. Pellet-clad interaction appeared only at the very high temperature sites, if the contact between pellet and clad was sufficiently good. The nitride phase formed only at the high elevations, its thickness reached 100-300 μm. The oxide layer thickness had an average 150-220 μm value in the upper part of the bundle. Cladding break up and peel off from pellet

performed during the cooling period, no oxide layer was seen on the inner side of the cladding. Spacer oxidised and fragmented on larger extent than cladding, certainly because of lower heat capacity. At the elevations of 535 and 555 mm asymmetry took place in the extent of degradation, certainly one side of the bundle was at higher temperature than the other.

The visual observation of the bundle showed strong oxidation on the external surface of the shroud, but no structural damage was seen. The 600 mm long UO_2 pellet filled stage of experimental bundle was cut and polished and grinded at the following elevations (in mm):

a.) 50 (Fig. 60)
b.) 150 (Fig. 61)
c.) 300 (Fig. 62)
d.) 450 (Fig. 63)
e.) 535 (Fig. 64)
f.) 555 (Fig. 65)

During the grinding process multiple embedding of the surface with epoxy resin was applied in order to avoid any breakout of the brittle materials.

The outlook of polished slices have been thoroughly investigated to identify the high temperature physical and chemical processes playing main role at change of bundle parameters.

For better identification the rods in the cross sections were numbered. Looking at the slice with outer thermocouple tube at the top, the upper right is the No. 1 and the numbering advances clockwise, the No. 9 is the rod in the middle.

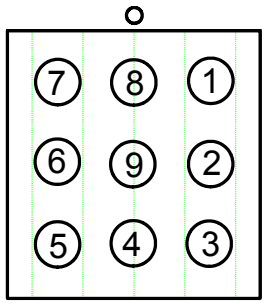

The general picture of the bundle showed very limited damage. The fuel rods below 450 mm elevation remained intact, and only some of the rods at higher elevations were failed. The most severe damage was related to the upper spacer grid, which was oxidised and broken into pieces. The photos of the whole cross sections are shown in Figs. 60-65 for elevations 50, 150, 300, 450, 535 and 555, respectively.

a.) 50 mm elevation

Slight oxidation on the outer surface of cladding and thin oxide and α-Zr layer were observed. The main part of the cladding wall shows typical earlier β-phase character. No pellet-clad interaction (PCI) can be identified.

b.) 150 mm elevation

The main part of the cladding wall thickness remained as earlier β-phase. The α-phase and oxide slightly thicker and at some places thin oxide layer is abrupted from the surface (Fig. 66). No PCI.

c.) 300 mm elevation

Even at this level the cladding remained β-phase in large extent. However, the α-phase is thicker (5-10%) and on outer surface layered oxide scale can be seen. No nitride phase can be seen. Typical view is shown in Fig. 67. No PCI took place in this segment.

d.) 450 mm elevation

The β-phase remained back on different extent on the tubes depending on their positions. Oxide and nitride phases can be seen on the outer surface. Fig. 68 shows some stages of rod No. 1. In Fig. 68/c about 30% of the wall thickness remained β-phase with thin α-scale on the outer side. Outwards these are followed by substantial nitride, further with oxide. At Fig. 68/b similar character appeared on the outer surface, but a nitride and α-phase can be seen at the pellet side, too. No PCI can be identified. Fig. 68/a presents a site where the outer oxide is broken through and in the vicinity thin oxide sheets peeled off. Under the oxide scale strong nitride formation appeared.

Fig. 69 shows a cladding stage of rod 2 with thicker β-scale than at rod 1. Again peel-off from the outer oxide layer took place. On the rod No. 6 (Fig. 70) a regular β-phase with thin α-layer appeared. The rod No. 8 (Fig. 71) near to the No. 1 shows again more irregular outer oxidation. It seems that the temperature maximums at rods No. 1 and 8 were higher than at the others. The central unheated rod No. 9 (Fig. 72) shows a temperature maximum between the No. 1, 8 and the others. On cladding inner surface thin α-layer can be seen. It is originated from air in the rod but not from PCI.

Fig. 73 shows a mosaic illustration of shroud and spacer at this elevation. The shroud remained in large extent β-phase but the spacer converted entirely to oxide and α-phase. Peeled-off oxide layers appeared on both metal sheets. The spacer had substantially higher temperature than the shroud and was oxidised on larger extent.

Looking over all the rods on slice of 450 mm, no pellet-clad interaction has been found.

e.) 535 mm elevation

The highest extent of oxidation and degradation appeared at this elevation. The Fig. 64 shows an overview of the slice. There are strong differences between the rods of different positions.

The lowest degradations are at rods No. 2 and 3. Both of them remained without rupture of cladding, strong oxidation was found only on their outer surfaces (Figs. 74/a, 75).

Even the β-layer remained back with substantial thickness. Pellet and clad interaction can be seen only at some areas where their contact was good enough (Fig. 74/a).

On the rod No. 1 stronger oxidation can be seen, not more than half of the original thickness remained back as metal, α-phase, with very thin β-layer at the pellet side. A typical view is shown in Fig. 76.

The rods No. 4-8 were at temperatures when the β-phase metal melted and flowed out at many places. The Fig. 77/a presents a site where the α-scale has opened on rod No. 4, melted β-phase escaped through the slit and the α-phase remained back around the cavity. Near to that (Fig. 77/b) the β-phase has flowed out also and some nitride formed on the inner side of the α-layer. Slightly more further (Fig. 77/c) the thickness of escaped metal seems to be thinner and some β-scale remained back on the surface of the α-metal phase. On the outer side of the α-layer nitride and oxide layers can be seen. At this place the cavity extended to half of the tube circumference. In Fig. 77/d the end of the cavity can be seen. It shows clearly that the melting stopped by disappearance of β-scale. The two α-layers formed through outer oxidation and by pellet-clad interaction got in contact with each other and disappeared the β-phase of lower melting point. The PCI effect can be seen also on the upper right corner of picture showing the characteristic U-Zr formation near to the contact line of UO_2 and Zr-alloy. Areas of the same rod with further PCI-s are shown in Fig. 78.

Strong oxidation and PCI of rod No. 5 can be seen in Fig. 79/a. The pellet has many break lines and nitride scale appeared between the ZrO_2 and α-phase. Fig. 79/b shows a cladding site where the β-layer escaped so that the outer α-layer moved near close to the pellet. Fig. 79/c shows a site where nitride is formed at the pellet-clad gap. Presumably air was circulating through the damaged rod.

The strong oxidation and PCI effect related to rod No. 6 can be seen in Figs. 80/a and 80/b. The second gives a view about the layers from the tungsten heater to the outer zirconium oxide. The thick epoxy layer between W and UO_2 is originated from the broken pellet.

At rod No. 7 again escape of melted phase was recognised (Figs. 81/a, 81/b). Presumably the metal was oxidised in larger extent and the α-phase had been advanced into the metal on the surfaces of crystals, like it was found at many earlier experiments. At the melting of β-scale it has flown out indicating very low viscosity of the liquid phase.

On rod No. 8 (Fig. 82) the oxidation was lower, only a part of β-scale was melted. Supposing an oxygen concentration difference in the β-phase, the estimated temperature maximum for this site was between 1760-1900°C.

The central rod was also rather oxidised, no β-phase remained and PCI appeared on a high extent (Fig. 83).

f.) 555 mm elevation

At this level the spacer is even more degraded than at 535 mm but the oxidation and deformation of the rods are slightly lower.

The rods No. 1, 6, 7 and 8 are oxidised on an extent that no β-scale can be seen. The PCI appeared with irregular probability.

The cladding of rod No. 1 is transformed entirely to α- and oxide layers, as it can be seen in Fig. 84.

Fig. 85 for rod No. 2, Fig. 86 for rod No. 3 and Fig. 87 for rod No. 4 show that a large part of the metal remained β-phase. The same was found for rod No. 5.

The clad of rod No. 6 was oxidised so strongly that no β-phase remained back. However, the lack of PCI indicates a lower value at the maximum temperature than at 535 mm level (Fig. 88).

The cladding of rod No. 7 has been broken and slightly moved away from the pellet. Fig. 89 shows that the piece of cladding has only α-phase, nitride and oxide. Because of the peeled off cladding has no oxide layer on its inner side, we suppose that the breaking off happened in the cooling stage when it was surrounded by argon.

The cladding of rod No. 8 has been oxidised to oxide and α-scale, without leaving back any β-phase. In spite of that, no interaction between the pellet and clad was identified (Fig. 90).

The central rod (No. 9) cladding again contained a substantial amount of β-phase, near half of the original thickness. PCI can not be identified. The oxidation of cladding performed certainly at lower temperature (Fig. 91).

6.1 LAYER THICKNESS MEASUREMENTS

The detailed investigation of bundle cross sections was carried with optical microscope. Using the image analytical features the different layers of the cross section structures were measured. Detailed measurement data in form of tables are attached to the Figs. 92-97, the thickness is given in μm units.

The layer thickness measurement of fuel rods included the determination of α and β phases, oxide and nitride layers, and also the pellet clad interaction layers.

The thickness of different layers on the rod circumference was not homogeneous, but in some cases had large variations. For this reason each layer on each rod was measured at least 5 times at different positions. For more complicated cases up to 10-12 measurements were taken and the average value was defined for the given rod. These average values are given in the tables.

The α and β phase thicknesses gave a complementary to each other picture. In the lower part of the bundle the total cladding thickness remained in β phase. At higher elevations it disappeared and only α phase was present. This distribution is in agreement with the temperature measurements. (Figs. 92-93)

The oxide layer thickness has an average 150-220 μm value in the upper part of the bundle. Rod No.1. has higher values, which indicates some local heat-up in the cross sections. (Fig. 94) Due to the very limited rod failures the internal surface of the cladding was not oxidised. The presented values were measured as the thickness of the external oxide layer.

Nitride formation was seen on the rods above 450 mm elevation. The thickness of nitride layer reached 100-300 μm. The nitride distribution showed also some asymmetry: at elevation 450mm rods No. 4-5-6 and 9 have nitride layers only. (Fig. 95)

Pellet-clad interaction took place only in the hottest part of the bundle and was observed at elevations 535mm and 555mm. The interaction layer was measured at the UO_2 side and at the β layer side.(Fig. 96) The measured values of interaction layers were between 50-130 μm. The pellet-clad interaction was observed only in 5 of the 9 rods.

The shroud part of the cross sections was also analysed with the optical microscope. The oxide layer thickness on the outside and on the inside of the shroud, and the α layer thickness also on the two sides of the shroud were measured. The shroud survived strong oxidation on both sides, the layer thicknesses on the two sides were comparable to each other. (Fig. 97.) The oxide layer thickness reached 100 μm on both sides at the top of the bundle.

6.2 INVESTIGATION OF PELLET - CLADDING INTERACTION

Sample was prepared for SEM+EDS studies at the elevation of 515 mm, where a reaction zone was revealed by metallography. Philips SEM 505 type of scanning microscope was applied together with a LINK AN 10/55S EDS analyser suitable for microanalysis from Na up to U.

Backscattered electron (BEI) image with 80 times of magnification (No. 0260.) shows a region, where the UO_2 annular pellet was touching the Zircaloy cladding. At the other side of the cladding the oxide layer could be seen. A large flaw could be recognised starting from the UO_2 pellet and proceeding across almost the whole cladding.

Layers with various brightness could be seen at the interface of the UO_2 and the cladding. The thickness of the first layer was about 35 – 40 μm. Inside there were small sized brighter particles with U content. However this layer contained more Zr as it can be seen in Table 4, showing the elemental composition of the various layers and phases at the interface. The second layer had about 100 μm thickness. There were also particles with brighter contrast. There was a thin gap between this and the next layer which had the brightest contrast. There were particles (phases) with bright contrast also in the next part of the cladding. The elemental composition data in the Table 1 have indicated that the particles shown in Fig. 98 with bright contrast were enriched in U. It means that the U went inside of the cladding to about 100 – 200 μm. As it can be seen from the elemental analysis data small amounts of Cr, Fe and Ni were present at various parts of the interaction zone.

EDS analysis position No.**	Element	Line	Amount (in at %)	Amount (in at %)

1	U	M a	88	33
	Sn	L a	0,8	1,6
	Fe	K a	0,1	0,4
	Ni	K a	0,1	0,5
	O*	K a	11	65,5
2	U	M a	87	32,7
	Zr	L a	0,2	0,2
	Sn	L a	0,8	1,6
	Fe	K a	0,2	0,3
	O*	K a	11,8	65,2
3	U	M a	2,2	0,8
	Zr	L a	94,9	90,9
	Sn	L a	1,2	0,9
	Cr	K a	0,2	0,3
	Fe	K a	0,3	0,5
	O*	K a	1,2	6,6
4	U	M a	20,9	8,1
	Zr	L a	74,8	75,2
	Fe	K a	1,6	2,6
	Ni	K a	0,2	0,3
	O*	K a	2,5	13,8
5	U	M a	49,3	24,4
	Zr	L a	48,6	62,7
	Cs	L a	0,1	0,1
	Cr	K a	0,4	1
	O*	K a	1,6	11,8
6	U	M a	92,6	77,6
	Zr	L a	4,8	10,6
	Cs	L a	0,5	0,7
	Cr	K a	0,3	1,1
	Fe	K a	1,3	4,5
	Ni	K a	0,1	0,4
	O*	K a	0,4	5,1
7	U	M a	64,7	41,2
	Zr	L a	35,1	58,4
	Cs	L a	0,1	0,1
	Cr	K a	0,1	0,3
	O*	K a	0	0
8	U	M a	0	0
	Zr	L a	97,3	91,3
	Sn	L a	0,7	0,5
	Ni	K a	0,6	0,8
	O*	K a	1,4	7,4

Table 4 EDS investigation results

Notes:

* Oxygen can not be analysed with the EDS. Its amount was calculated by the instrument with normalisation to 100 %.

** EDS positions can be seen in the digital SE image.(Fig. 98)

6.3 MEASUREMENT OF NITROGEN

Light elements such as oxygen, nitrogen, boron etc. can be analysed by electron beam microanalyser if they are present in about 5 m%. The spectral line of nitrogen K alfa photons is relatively wide, with a maximum at 90,23 mm. The place of the maximum is slightly varied in function of the nature of the chemical bond.

Sample for electron beam microanalyser was prepared from the bundle at elevation of 495 mm, where the presence of zirconium nitride was suspected. There was a failure at the edge of the outer ZrO_2 layer where the material was open up. Yellowish areas could be seen by optical microscope at the interface between the Zircaloy cladding and the UO_2.

For searching and analysing nitrogen in the cladding were done by a JEOL Superprobe 733 type of electron beam microanalyser using a crystal spectrometer with stearate crystal. 10 kV accelerating voltage and 3×10^{-8} A beam current were used. As standard sample boron nitride from Taylor Co. was applied.

The following method was used for the studies:

1. By means of an optical microscope interesting areas were selected and marked. They were searched by the optical microscope of the microanalyser. The electron beam was directed and left on the selected spots on the cladding for the measurement.

2. Spectral lines of nitrogen K alfa photons were taken from the interesting areas and from the Zr matrix by measuring the intensity of the X-rays while the stearate crystal was moved from 84 mm to 94 mm with a step of 0,5 mm. X-ray intensities were stored on disk for further evaluation.

Results are shown in the Fig. 99, where the *y phase* relates to the nitride with yellow colour. The maximum intensity of nitrogen K alfa photons was about a quarter of the one measured for the boron nitride standard. It might be supposed that the nitrogen content of the studied cladding was about 15 m%.

7. AEROSOL MEASUREMENTS

For the measurement of the aerosols generated during the pre-oxidation and air ingress phases of AIT-1 two laser particle counters and ten cascade impactors were applied [8]. The connection of the detectors to the facility is illustrated in Fig.2.

During the test all particle counter devices were working successfully, without any malfunction. The data were measured and stored continuosly without any losses. The peaks at oxidation and after oxidation were measured simultaneously by internal and external

counters (Figs. 54-59). The pre-oxidation and air ingress peaks correspond to the appropriate temperature peaks in the preheating and heating period. The dynamic range of the total concentration measured by APC-03-2 was ~ 10^5 (from 10^1 –10^2 particles/litre in the beginning of the experiment up to 1-2x10^6 particles/litre at excursion peak). This range is in the measurable range of the particle counter. These devices had no saturation, overloading or contamination due to the high concentration. At the end of the measurements the measured results show the same values as in the beginning of the experiment. The particle counters survived high temperature of gas flow. The results of the measurements were obtained in particle and mass concentration at various size ranges. During the AIT-1 test the cooling period was characterised by a large scale aerosol release.

Altogether there were 20 impactor plates in the cascade impactors. Each unit contained two plates and at the outlet of the unit a filter plate was mounted (Fig. 100). The impactors were switched on during the air ingress phase of the test. They were operated in series and each was operated for 60 sec while 1 litre/min released gas was sucked through the impactor unit. The 10 x 60 = 600 s time functioning period means that the most important phase of the test was covered by impactor sampling. The first unit was switched on when the test section temperature reached 1200°C. At this moment the process time was 29640 s. This data enables to adjust the aerosol sampling to the process temperature curve illustrated in Figs. 9-59.

The objective of the post test examination of the collector and filter plates was the investigation of the size, shape and elemental composition of aerosol particles released during the air ingress test performed in the CODEX facility. Special interest was given to look whether there is any uranium release and if so, what is the size and shape of the aerosol particles bearing it.

Aerosol particles were collected by 10 impactors having two collector plates with small sized Si wafers and one quartz fibre filter. Ni impaction plate was placed near to the cooler to collect aerosol particles, too. A quartz fibre filter was placed into each impactor assembly before the outlet to collect the particles not deposited earlier on the divertor and collector plates. Samples settled on the first collector plates are marked by B, while the ones on the second by D. Neither carbon, nor Au was evaporated to the surface of the 20 collector plates, i.e. the as received surfaces were studied. The quartz fibre filters were cut out from fibre produced for filtering environmental aerosols and analysing them usually by X-ray fluorescence methods. To avoid the background of impurities from the filter material they were made of high purity quartz fibre delivered by Binzer & Munktell Filter GmbH. Samples for spark source mass spectrometry were prepared by mixing and thoroughly pulverising the quartz filters together with high purity graphite powder (ULTRACARBON Ultra Superior Quality). The weight of the filters were about 6 mg, the graphite added to them was 100 mg. These mixtures were used to prepare the electrodes for the sparking. They were filled into a special polyethylene form and pressed together up to 1000 MPa. This procedure resulted in a small graphite rod suitable for sparking in the ion source. Because of the small amount of mixture they were used only in the tip of the electrodes, a longer part was pure graphite. As inner standard 20 at ppm Pt was mixed into the graphite.

Scanning electron microscopy (SEM) combined with image analysis was used for studying the size and shape of the aerosol particles settled on the collector plates and on the

Ni impaction plate. Elemental composition of single particles and aggregates of them was examined by *energy dispersive microanalysis* (EDX), while analysis of particles collected by the filters was done by *spark source mass spectrometry*(SSMS). Classification of the aerosol particles by their elemental composition was done by a particle characterisation program.

7.1 MORPHOLOGICAL STUDIES AND IMAGE ANALYSIS

There were aerosol particles on each collector plate, but the coverage of the surfaces of the Si wafers by aerosol particles was different for the aerosol samples taken at different time periods. By visual examination of the surface of the collector plates it was found that the greatest number of particles and also the largest ones were settled on sample 1B. On the second collectors (D) there is generally a centre part on the Si wafer which is more densely covered by particles than the surrounding part of the wafer. The diameter of this part is about 1 mm. The degree of coverage is decreasing by increasing time duration, but there is a smaller "peak" in respect of degree of coverage at sample 7 and 8.

On the surface of each sample holder there were areas where individual aerosol particles could be distinguished. However there were bundles and/or aggregates of single particles, too. The shape of the particles was mostly slightly elongated. Globular particles, long plates and rectangular grains were also found. Beside aerosol particles with 0,1 - 0,3 μm, there are plate-like particles and bundles of smaller particles. The length of the plates is several tens of μm, while the width of them is about 2-3 μm. The size of the single aerosol particles ranges from about 0,1 μm up to a few μm and generally has not extend over 5-6 μm. These results correspond to that of the aerosol particle counter. The bundles or aggregates of the individual aerosol particles may have a size of several tens and even more than 100 μm. They were formed probably by resuspension of the aerosol particles.

The largest percentage of the smallest particles was detected for sample 10D, i.e. at the end of the sample collection in air ingress test. It is quite obvious that the largest particles were bigger for samples taken at the beginning and in the middle stage of the procedure than the ones taken at the end of the process. In the middle stage of the sample collection, there were aerosol particles in the larger diameter intervals. The SEI images have shown that large platelets were mostly found at the beginning of the sample collection, however some amounts of plate-like structures were found in almost every sample. This was proven by the results of particle shape characterised by the ratio of the minimum and maximum Feret diameters. At the beginning of the sample collection (i.e. for sample 1 B and D) there are more amount of particles having more elongated shape. Sample 5D has a maximum at slightly higher value than the others. However the shape of the aerosol particles deposited in different time periods did not show so large differences than the size of them. All these findings are corresponding to the results of the laser particle analyser where the greatest number of particle has the smallest diameter and there is a second peak for the larger particles at samples 5-8.

7.2 ELECTRON BEAM MICROANALYSIS AND PARTICLE CLASSIFICATION

At the beginning of the sample collection, i.e. following the high temperature region of the air ingress test, most of the individual particles present on the first collector of impactor

No.1 (sample 1B) contain tin (Sn) originating probably from the Zircaloy cladding. Zr was also detected. The plate-like structure contains Zr in form of very fine sized particles building up the plate. They are probably ZrO_2 emitted by the insulating material. Plates are not always Zr-rich, some of them are silicates. In the order of decreasing quantity the following elements were found: Al, S, Cl, Cr, Mg, Fe, Ni, Ti, W, Cu and Na. Some of them were present only in some particles. These elements are originated mostly from the structural materials including the insulating materials such as ZrO_2 and Al_2O_3 used in the test, however some others, such as S, Cl and Na might be originated from the neighbourhood. Typical ED spectra together with the SEM image are shown in Fig. 101.

At the middle stage of the aerosol sample collection (e.g. sample collector No. 6) the emission of Sn and Zr was also significant, besides the presence of Fe, Cr, Ni and Ti containing particles is worth to mention.

At the end of the aerosol sample collection, Sn, Zr were found together with the components of the structural materials, such as Fe, Cr, Zn and Ni.

U-rich particles with a few times 10^{-11} g were detected by EDS on impactor sample No.1 (during the high temperature escalation). Uranium was present mostly in single particles (1-3 μm) with rectangular shape.

Some elements such as Ta, Y, W were found only in the composition of a few particles. Y might be present as minor component of zirconia, while W came probably from the heating wire.

All these findings were proven and quantified by the results of the classification by the chemical composition as follows:

- On the first collector of impactor No. 1 (sample 1B) studied at magnification of 1000x, the most popular class is the one richest in Sn (lower part of Fig. 101). This class is owed by 50 % of the particles (by number) and the mean particle diameter is 1,5 μm. Beside Sn, the following elements were detected: Al, S, Cl, Cr, Mg, Fe, Ni, Ti, Zn, Zr, W and Cu. The net X-ray intensities for the last seven elements are less than 5 %. The standard deviation for these elements are relatively high. The second most popular class contains also significant amount of Sn and Al, Zr, Mg, Cr and Fe. The mean diameter for this class is 3,6 μm and the percentage probability or abundance is 19 %. The third class is owed by 17 % of the aerosol particles with mean diameter of 2 μm. The net intensity of Sn is larger than that of the previous class, but there is smaller amount of Al. Beside these elements, S, Cl, Cr and Zn are worth to mention. There are three classes with abundance of 7; 5 and 2 %, respectively, where the net intensities of S, Fe and Zn are the largest. Sn is always present even in these classes. The largest mean diameter was found for Fe-rich particles at magnification of 1000 x.

- On the second collector of impactor No.1 (sample 1D) the most popular chemical class is the one richest in Sn. The 45 % of the evaluated particles belongs to this class. Beside Sn, the following elements were detected: Al, S, Cl, Cr and Mg. The amounts of the other elements such as Fe, Ti, Ni and Zn are less than 5 %. This Sn-rich class has the second largest mean diameter: 1,69 μm, the largest particles are again enriched in Fe

(with mean diameter of 2 μm). There are three other classes containing also Sn but in smaller quantities than the above mentioned class. One of these classes contains significant amount of Al coming probably from the insulating material. The other components are the same as above. In one of these classes there is Cr beside Sn, Al and Cl. There is one chemical class - richest in Fe, which is owed only by 2 % of the particles. Beside Fe, Sn, Al and S are emitted in more than 5 %.

- At the middle stage of the aerosol sample collection (impactor plate No. 6) the most popular class is owed by 67 % of the particles with mean diameter of 0,82 μm. The main component is the Sn, besides the following elements are present in an amount higher than 5 %: Ti, Cr, Fe, Cl and Ni. Zr is present, but the net intensity of it is only 2,35 %. There is much more Zr in the second most popular chemical class containing also Sn, Ti, Cr, Fe and Ni. All these elements are originating from the cladding and from the structural materials. The third chemical class contains the largest amount of Sn (45 %) owed by 7,4 % of the particles. Beside Sn, Cl, Cr, Ti and Fe are present in more than 5 %. The fourth class contains only 1,5 % of the particles enriched in Cr and Fe. Beside these elements the net intensities of Sn, Ti, Cl are more than 5 %. The net intensity of Zr is only 2,27 %. Again this chemical class has the largest mean diameter: 3,18 μm.

- At the end of the aerosol sample collection (sample collector No. 10 D) the most frequently found element is Sn. Besides the mean value of Zr net intensity is the largest and generally there is more amount of Zr in each class than it was found at the earlier stages of the aerosol sample collection. The most popular class is owed by 41 % of the particles enriched mostly in Sn. Besides there are significant amounts from the following elements: Cr, Fe, Ni and Zn. Zr is present in 4,2 % and there are two elements detected only at this stage: Br and Y. In these sample there are more number of chemical classes than before, but Sn is always present. Besides Zr, Fe, Zn and Cr are the characteristic elements of other classes containing also some amount of S, Cl, Ni, Br and Y. The last two elements are not always present in an amount worth to mention. In the point of view of the main components and also of some minor elements there is a good agreement between the results gained by EDX and by spark source mass.

7.3 ESTIMATION OF THE AEROSOL PARTICLE VOLUME AND MASS

On the basis of the chemical classification by ED spectra of aerosol particles for some selected samples a very rough estimation can be done by using the measured mean particle diameters and particle numbers per each chemical class. If sphere shape is supposed, rough data for the total measured volume of aerosol particles can be calculated. Taking into account that in some chemical classes there are more amount of Sn and/or Zr, Fe etc., the total mass of the measured particles can be estimated by using density of 5 or 4,75. It can be stated that there is a large difference among the studied samples in the total particle volume and mass. Taking into account that the measured 200-300 particles were settled in a part of about 1000 μm^2 and the most densely packed area on the Si wafer is about 1 mm^2, i.e. 1000 x larger, it can be supposed that aerosol amounts between a few μg and 400 μg might be present on the collector plates. The largest amount is for sample 1 B, which is densely packed by particles not only on the Si wafer, but all the area among the four holes. The smallest value is for

sample 10D, i.e. for the end of the sample collection. On the basis of the above estimation the total amount of aerosol in the outlet gas might be about 90 - 100 mg/litre.

7.4 RESULTS OF SPARK SOURCE MASS SPECTROMETRY

The results of the elemental analysis of filters are summarised in Table 5. The most important metal components are as follows: Sn, Fe, Zr, Ni, Cr, Mn, Nb and Mo. All these elements were found in the first sample. We have to remember, that the first impactor collected the aerosols during the escalation process and at the beginning of cooling after air ingress.

Impactor	1	2	3	4	5	6	7	8	9	10
Element	(μg)	(μg)	(μg)	(μg)	(μg)	(μg)	(μg)	(μg)	(μg)	(μg)
Na	2,5	0,70	0,08	1,60	1,0	0,8	3,7	0,8	3,2	2
Mg	13	1,4		2,8	3		4	8	2	4
Al	6,3	0,02	0,1	3,5	3,3		0,02	0,1	13	2,6
P	2,6	0,3	0,12	1,3	0,4	0,6	1,2	1,3		1,3
S	9,3	3,6	0,3	3,4	1,4	1,5	3,4	1,3	3,5	3,4
Cl	25	7	1,1	10	6	11	24	5	26	10
K	1,6	1,7	0,1	0,4	0,5	1,2	11	1,2	0,9	0,4
Ca	2,90	3,30	0,36	3,90	1,2	2,5	7,0	3,9	5,0	10
Ti	14						1,3	0,5	0,1	
Cr	16	0,02	0,2	0,4	0,14		1,4	1,1	13	0,4
Mn	1,8	0,3	0,03	3	0,03	0,10	0,54	0,31	0,39	0,3
Fe	22	4	0,6	5	3,6	3,8	21	14	25	5
Co				0,1		0,03		0,02		0,1
Ni	19	4	0,6	0,7	0,20	0,33	1,2	1,5	1,1	0,7
Cu	6	20	0,2	4,8	2	3	10	6	13	1,9
Zn	4	15		1,7	0,4	0,6	0,6	0,2	0,6	1,2
As	0,15	0,03		0,05				0,10		
Br	0,5	0,25			0,02	0,2	0,5	0,2	0,4	0,05
Rb		0,005	0,003	0,09						
Sr	0,04	0,008	0,002	0,25	0,16	0,01	0,01	0,01		0,005
Y	0.9	0,004	0,003	0,03	0,20	0,06	0,56	0,06	0,05	0,31
Zr	12	1,8	1	1,1	3,8	1,2	24	2,1	1,6	9
Nb	0,2	0,004	0,003		0,61		0,20	0,22		0,33
Mo	22	0,15	0,1							5
Ag	0,2	0,01					0,033	0,056	0,086	
Sn	230	3,7	2,1	1,3	0,09	0,58	0,75	0,33	0,31	5
Cs		0,006	0,01	0,23				0,01		
Ba	0,3	0,032	0,01	0,06		0,02	0,08	0,03	0,09	0,05
Pb		0,6		0,5			19		55	

Table 5 Amount of collected elements on quartz fibre filter,
results from spark source mass spectrometric analyses

The highest amount of element detected on the filter of Sampler 1. is the tin with 230 μg, far above the values of any other component. Its amount is falling back rapidly by the

time, that means by the cooling down of the bundle. During a sampling event 1 litre/minute gas was pumped through the sampler. It is about 1/200 part of the total gas volume escaping from the test system. From this value it can be extrapolated that about 0.7% of the total tin content in the bundle was emitted. Presumably the tin escaped in form of very small particles (smaller than 1 μm) and that is the reason, why they were not precipitated on plates in sampler before the quartz fibre filter. The SEM-EDX investigations have shown, that the tin was in small particles and as rough assessment of 400 μg total precipitation (the half of it is Sn) on the plates can be concluded. Altogether a 2 % escaped part might be supposed.

In Fig. 102 the amounts of some elements (Sn, Zr, Fe, Nb, Cr and Ni) are plotted as function of the sampler numbers. It can be recognised that these elements are present in the largest quantity in Sample 1., but they were detected in all of the samples. The only except was the niobium. It was under the detection limit in Samples 4 and 6.

The numbers of particles measured by the Aerosol Particle Counter 1. has been summarised for different sizes and for those intervals, when the impactors were used. The results can be seen in Fig. 103. It can be concluded that there is an agreement with the morphological studies. Obviously the particle analyser has caught mostly individual particles - similar ones that were shown in SEM images - and aggregates were formed probably during travelling to the impactors.

The amount of small sized particles (0.3-0.5 and 0.5-1) decreased with the sampler number on a similar way as the tin concentration. That is supporting also the assumption, that the tin is enriched in the aerosol particles with small sizes.

The amount of zirconium proved a monotone decrease only at the first some samples, later the amount changed irregularly. Presumably this element is appeared in larger particles, those numbers have larger statistical fluctuations. The relative large amount of Zr in the last sampler can not be connected to any of the APC results, but it is correlating with the EDX results. It was found by SEM and EDX analysis that Zr was enriched in larger particles at the end of the aerosol collection by impactors. These particles came probably from the cladding, while at the escalation period mostly fine sized zirconia building up larger plate-like structures was detected.

An increase of particle and element concentrations was observed at the sampling period from 6 to 8. It reflects a strong post excursion emission, probably originated from thermomechanical stresses in the oxide type layers. Similar effect was observed at other high temperature aerosol experiments.

On the quartz fibre filters the U content was below the detection limit of SSMS (1 ng). On the Ni impaction plate 7 ng/cm^2 uranium was detected by SSMS. On the basis of these findings the total uranium release could be assessed as a few tenth of microgram.

In Table 5 some other elements can be seen as well. Many of them are components of ceramic materials, metal components of bundle or impurities from cleaning agents. They have no substantial meaning from the point of view of the explanation of processes in the high temperature bundle. The high sensitivity of the method resulted values even at very low concentrations.

8. EXPERIMENTAL DATABASE

The experimental data were collected for code validation purposes into a database, which cover 31417 s time period with 1 s frequency. The frequency of particle counter recording was different and for this reason the database has the appropriate values in the recorded points only. The parameters are listed in Table 6 and plotted in Fig. 9-59 for the period of 25000-31000 s.

The database is presented in a large ASCII type file. The first column of the matrix contains the time. The "0" experimental time was set to real time 10:42:41, 7th May 1998. Each variable listed in Table 6 is given in a separate column in the file. The order of variables is the same as listed in the table. The commissioning test database has a similar structure, but the number of recorded variables was less (Table 7).

Name	Unit	Definition
TIME	s	Time
UH50	°C	Unheated rod temperature at 50mm
UH150	°C	Unheated rod temperature at 150mm
UH300	°C	Unheated rod temperature at 300mm
UH450	°C	Unheated rod temperature at 450mm
UH535	°C	Unheated rod temperature at 535mm
UH570	°C	Unheated rod temperature at 570mm
SP535	°C	Spacer temperature at 535mm
H50	°C	Heated rod temperature at 50mm
H150	°C	Heated rod temperature at 150mm
H300	°C	Heated rod temperature at 300mm
H535	°C	Heated rod temperature at 535mm
SH50	°C	Shroud temperature at 50mm
SH150	°C	Shroud temperature at 150mm
SH300	°C	Shroud temperature at 300mm
SH450	°C	Shroud temperature at 450mm
SH535	°C	Shroud temperature at 535mm
HS50	°C	Steel heat shield temperature at 50mm
HS150	°C	Steel heat shield temperature at 150mm
HS300	°C	Steel heat shield temperature at 300mm
HS450	°C	Steel heat shield temperature at 450mm
HS535	°C	Steel heat shield temperature at 535mm
OS50	°C	Outside shield temperature at 50mm
OS150	°C	Outside shield temperature at 150mm
OS300	°C	Outside shield temperature at 300mm
OS450	°C	Outside shield temperature at 450mm
OS535	°C	Outside shield temperature at 535mm
TLOCH	°C	Lower Chamber temperature

TUPCH	°C	Upper Chamber temperature
TMELT	°C	Thermocouple with opened end at 0mm
PYR450	°C	Pyrometer temperature at 450mm
PYR535	°C	Pyrometer temperature at 535mm
TIN1	°C	Gas inlet temperature at the superheater outlet
TIN2	°C	Gas inlet temperature in the inlet junction
TCOUT	°C	Gas outlet temperature in the outlet junction
TINC	°C	Gas temperature at the cooler inlet
TOUTC	°C	Gas temperature at the cooler outlet
PSYS	bar	System pressure
PINS	bar	Rod internal pressure
ARGON	g/s	Argon flowrate
AIR	g/s	Air flowrate
POWER	W	Electric power
API1	particle/l	Concentration of 0,3-0,5 μm aerosols, internal counter
API2	particle/l	Concentration of 0,5-1,0 μm aerosols, internal counter
API3	particle/l	Concentration of 1-3 μm aerosols, internal counter
API4	particle/l	Concentration of 3-5 μm aerosols, internal counter
API5	particle/l	Concentration of 5-10 μm aerosols, internal counter
API6	particle/l	Concentration of >10 μm aerosols, internal counter
APE1	particle/l	Concentration of 0,3-0,5 μm aerosols, external counter
APE2	particle/l	Concentration of 0,5-1,0 μm aerosols, external counter
APE3	particle/l	Concentration of 1-3 μm aerosols, external counter
APE4	particle/l	Concentration of 3-5 μm aerosols, external counter
APE5	particle/l	Concentration of 5-10 μm aerosols, external counter
APE6	particle/l	Concentration of >10 μm aerosols, external counter

Table 6 Parameters in the CODEX-AIT-1 database

Name	Unit	Definition
TIME	s	Time
UH50	°C	Unheated rod temperature at 50mm
UH150	°C	Unheated rod temperature at 150mm
UH300	°C	Unheated rod temperature at 300mm
UH450	°C	Unheated rod temperature at 450mm
UH535	°C	Unheated rod temperature at 535mm
UH570	°C	Unheated rod temperature at 570mm
SP535	°C	Spacer temperature at 535mm
H50	°C	Heated rod temperature at 50mm
H150	°C	Heated rod temperature at 150mm
H300	°C	Heated rod temperature at 300mm
H535	°C	Heated rod temperature at 535mm
SH50	°C	Shroud temperature at 50mm

SH150	°C	Shroud temperature at 150mm
SH300	°C	Shroud temperature at 300mm
SH450	°C	Shroud temperature at 450mm
SH535	°C	Shroud temperature at 535mm
HS50	°C	Steel heat shield temperature at 50mm
HS150	°C	Steel heat shield temperature at 150mm
HS300	°C	Steel heat shield temperature at 300mm
HS450	°C	Steel heat shield temperature at 450mm
HS535	°C	Steel heat shield temperature at 535mm
OS50	°C	Outside shield temperature at 50mm
OS150	°C	Outside shield temperature at 150mm
OS300	°C	Outside shield temperature at 300mm
OS450	°C	Outside shield temperature at 450mm
OS535	°C	Outside shield temperature at 535mm
TLOCH	°C	Lower Chamber temperature
TUPCH	°C	Upper Chamber temperature
TMELT	°C	Thermocouple with opened end at 0mm
PYR450	°C	Pyrometer temperature at 450mm
PYR535	°C	Pyrometer temperature at 535mm
TIN1	°C	Gas inlet temperature at the superheater outlet
TIN2	°C	Gas inlet temperature in the inlet junction
TCOUT	°C	Gas outlet temperature in the outlet junction
TINC	°C	Gas temperature at the cooler inlet
TOUTC	°C	Gas temperature at the cooler outlet
PSYS	bar	System pressure
PINS	bar	Rod internal pressure
ARGON	g/s	Argon flowrate
POWER	W	Electric power

Table 7 Parameters in the CODEX-AIT-1 commissioning test database

9. SUMMARY AND CONCLUSIONS

The CODEX-AIT-1 experiment represents the first integral fuel rod bundle degredation test under air oxidation conditions [9]. The experiment was carried out with electrically heated 9-rod PWR type bundles. Temperature, flowrate, pressure measurements were recorded during the tests. Pyrometers and high temperature thermocouples were used for temperature measurements. Aerosol release was measured using on-line particle counters and cascade impactors. The bundle cross sections and aerosol impactor samples were investigated in the post-test examination process.

The test indicated the acceleration of oxidation phenomena and core degradation processes during the late phase of the vessel melt through accident, when the air can have access to the residual fuel bundles in the reactor core. The degradation process was accompanied with zirconium-nitride formation and release of U-rich aerosols.

ACKNOWLEDGMENTS

The CODEX-AIT-1 test was performed in the OPSA (Oxidation Phenomena in Severe Accidents) project of the Fourth Framework Programme with the financial support of the European Commission (contract number FI4S-CT96-0031).

REFERENCES

[1] D.A. Powers, L.N. Kmetyk, R.C. Schmidt, A review of the technical issues of air ingression during severe reactor accidents, Sandia National Laboratories operated by Sandia Corporation, NUREG/CR-6218 SAND94- 0731 (1994)

[2] Sheperd I, B. Adroguer B, Buchmann M, Gleisberg O, Haste T, Hofmann P, Hózer Z, Hummel R, Kaltofen R, Knorr J, Kourti N, Leonardi M, Oriolo F, Schneider R, Maróti L, Matus L, Schanz G, Windberg P. Oxidation Phenomena in Severe Accidents, Proceedings of FISA-99, Luxemburg 29 November - 1 December 1999, pp. 193-201

[3] L. Maróti, “Chemical Interaction between VVER Core Components under Accidental Conditions”, Nucl. Eng. and Design vol. 172, 1997, pp. 73-81

[4] Z. Hózer, L. Maróti, B. Tóth, P. Windberg,”VVER-440 Core Degradation Experiment” Proceedings of NURETH-8, Vol. 2, Kyoto, 1997, pp. 605-611.

[5] Hózer Z, Maróti L, Nagy I, Windberg P: CODEX-2 Experiment: Integral VVER-440 Core Degradation Test, KFKI-2000-02/G

[6] Z. Hózer , L. Maróti ,P. Windberg, “Quenching of High Temperature VVER Bundle”, Proceedings of NURETH-9 on CD, San Francisco, 1999, ISBN 0-89448-650-0

[7] Hózer Z, Maróti L, Nagy I, Windberg P: CODEX-3/1 and CODEX 3/2 Experiments: Quenching of High Temperature VVER Bundles, KFKI-2000-03/G

[8] Pintér Csordás A, Matus L, Czitrovszky A, Jani P, Maróti L, Hózer Z, Windberg P, Hummel R: Investigation of aerosols released at high temperature from nuclear core models, J. Nucl. Materials, vol 282, Iss 2-3, pp. 205-215

[9] Trambauer K, Haste T J, Adroguer B, Hózer Z, Magallon D, Zurita A: In-Vessel Core Degradation Code Validation Matrix, Update 1996-1999, NEA/CSNI/R(2000)21

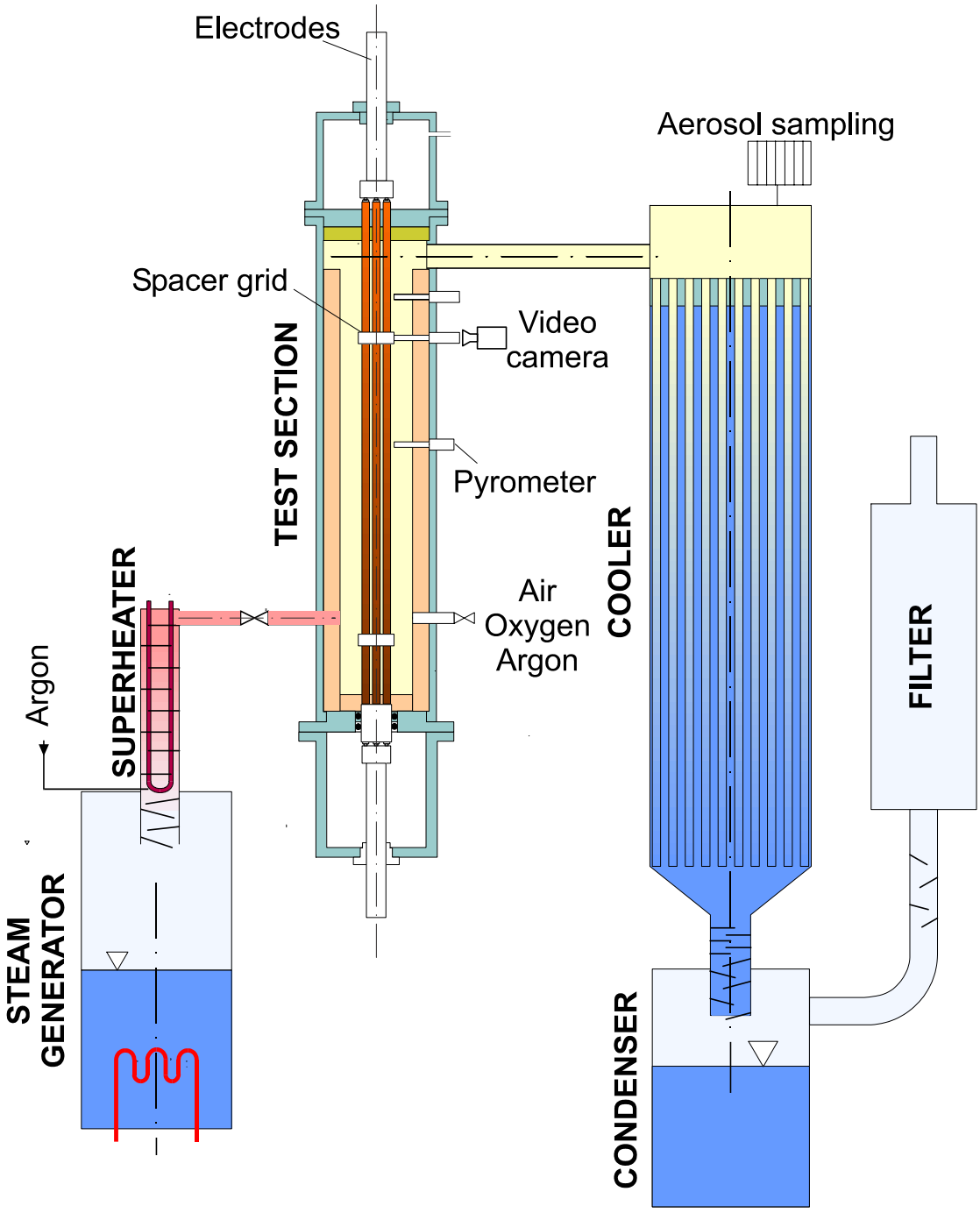

Fig. 1 Scheme of the CODEX-AIT-1 facility

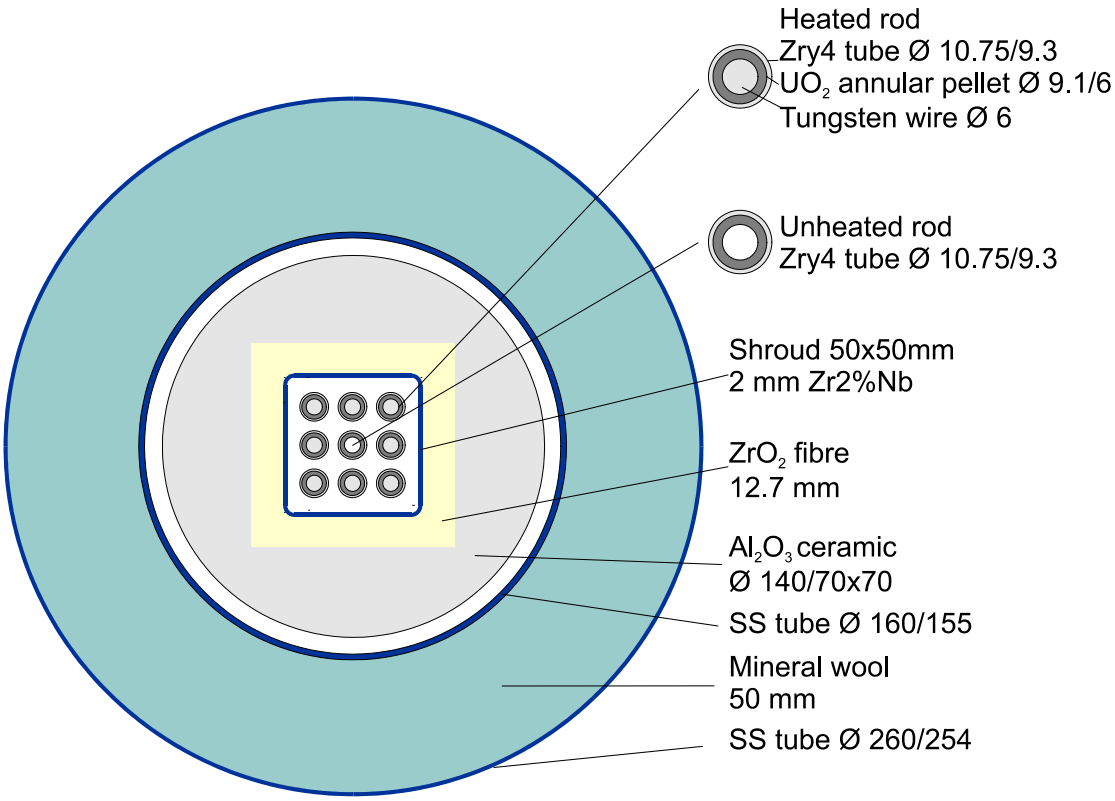

Fig. 2 Horizontal cross section of the CODEX-AIT-1 9 rod PWR bundle

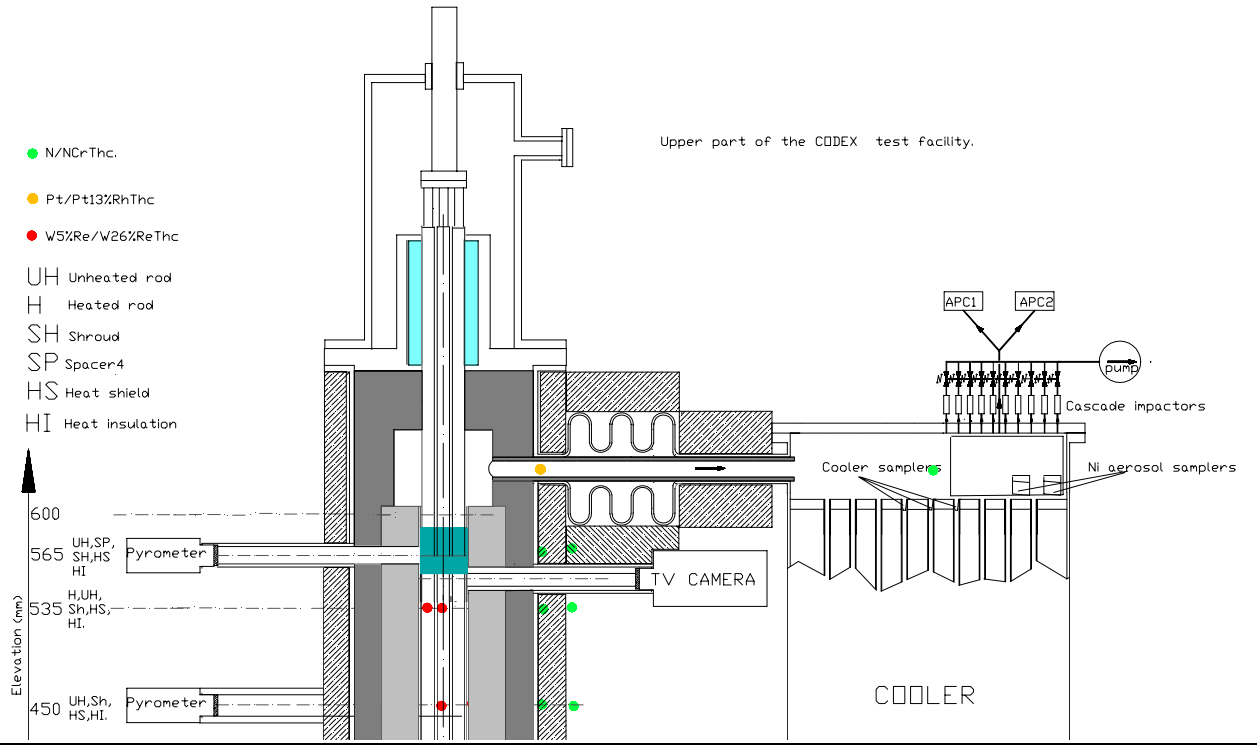

Fig. 3 Aerosol sampling in the CODEX-AIT-1 test

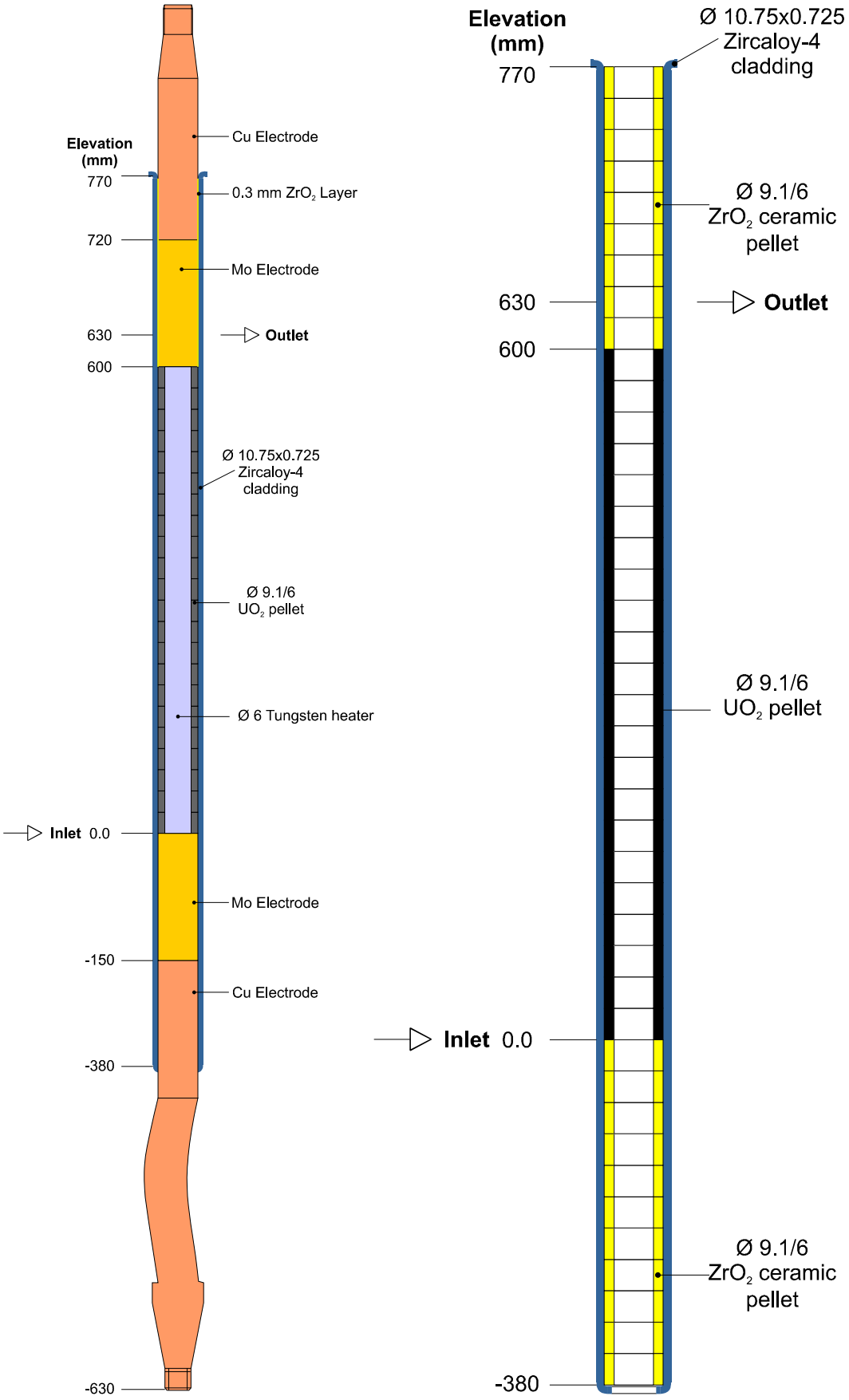

Fig. 4 Vertical cross section of heated and unheated rods

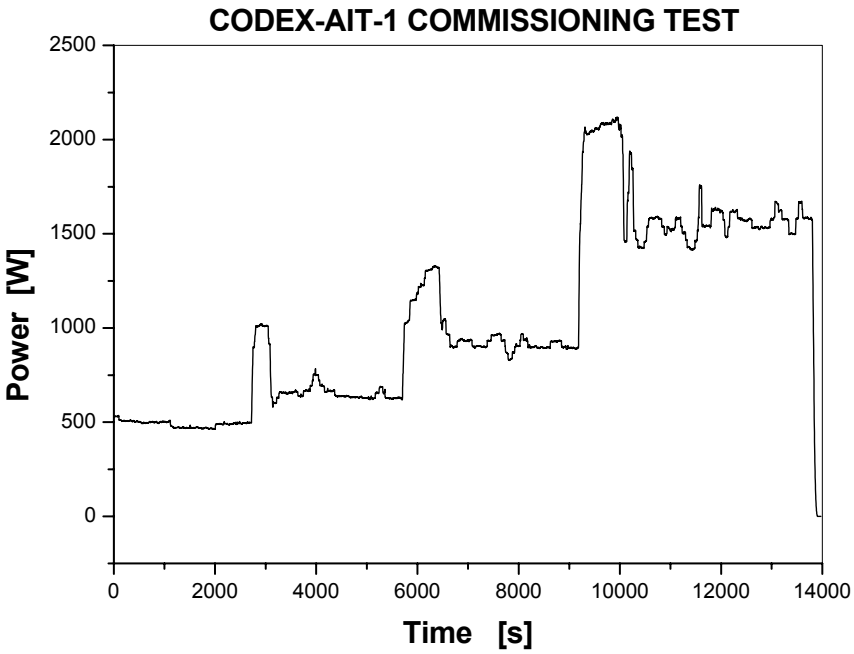

Fig. 5 Electrical power in the CODEX-AIT-1 commissioning test

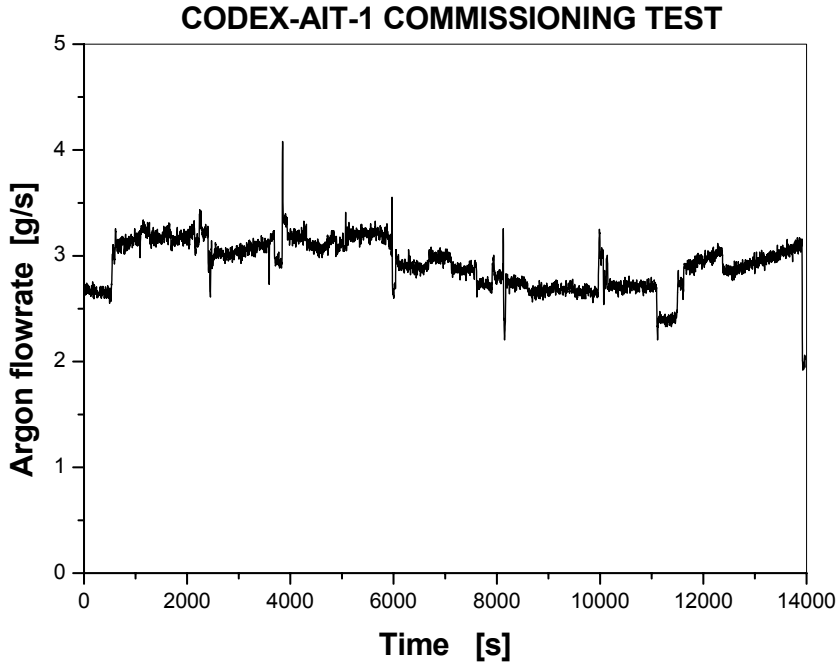

Fig. 6 Argon flowrate in the CODEX-AIT-1 commissioning test

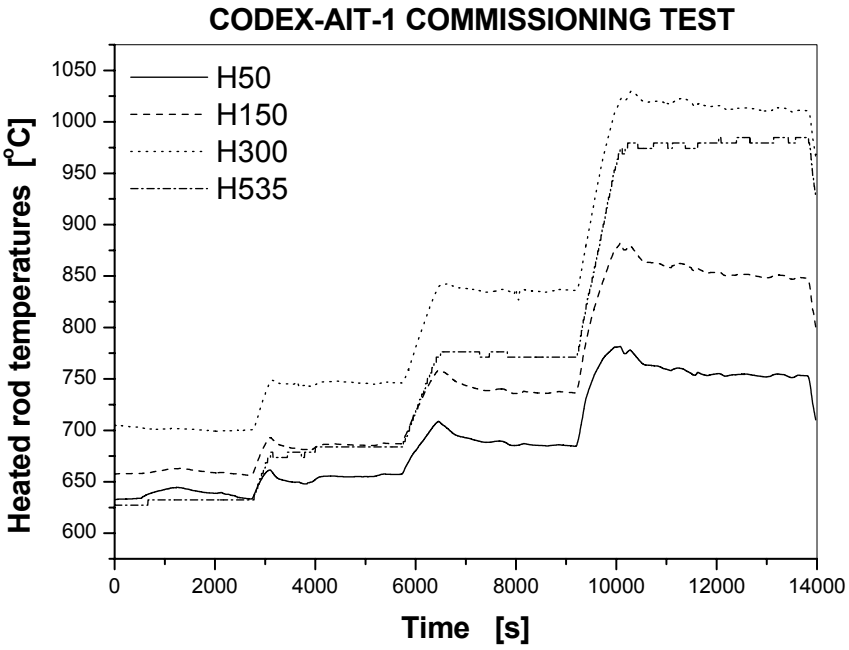

Fig. 7 Heated rod temperatures in the CODEX-AIT-1 commissioning test

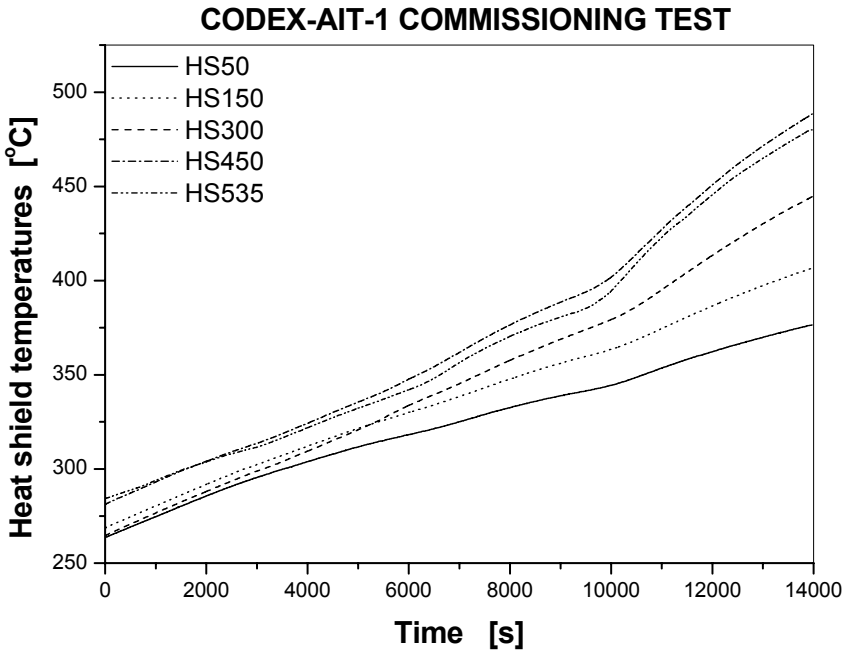

Fig. 8 Steel temperatures in the heat shield in the commissioning test

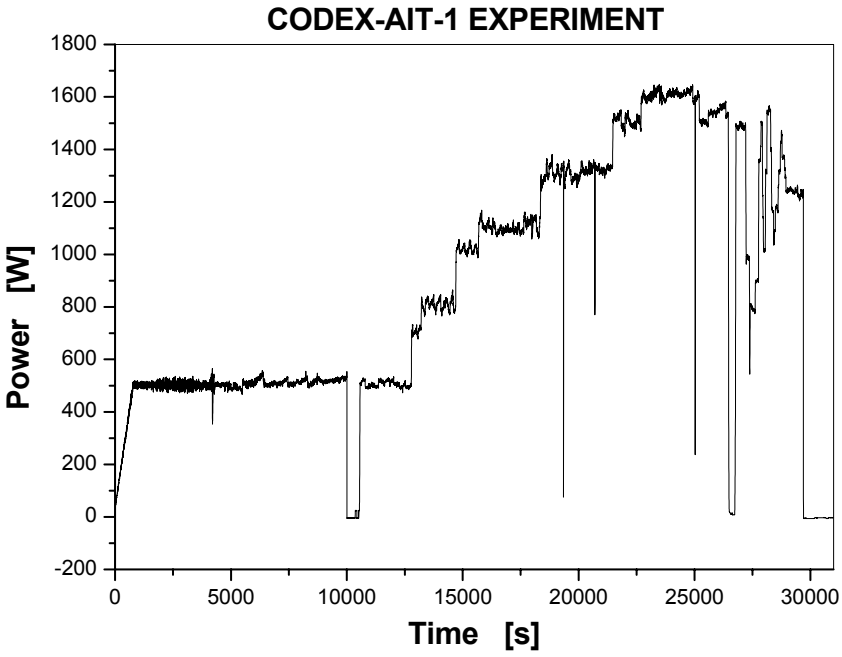

Fig. 9 Electrical power during the total recorded period

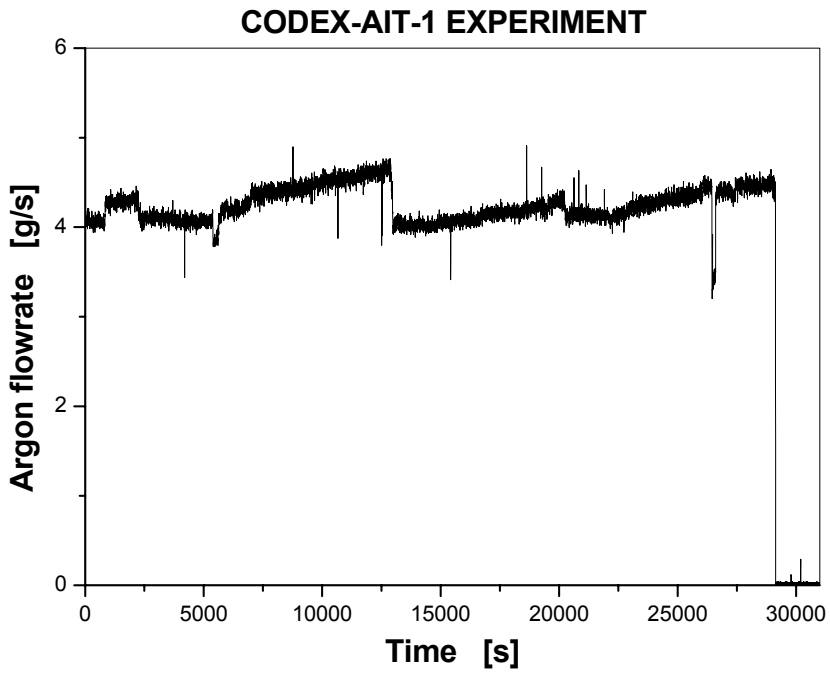

Fig. 10 Argon flowrate during the total recorded period

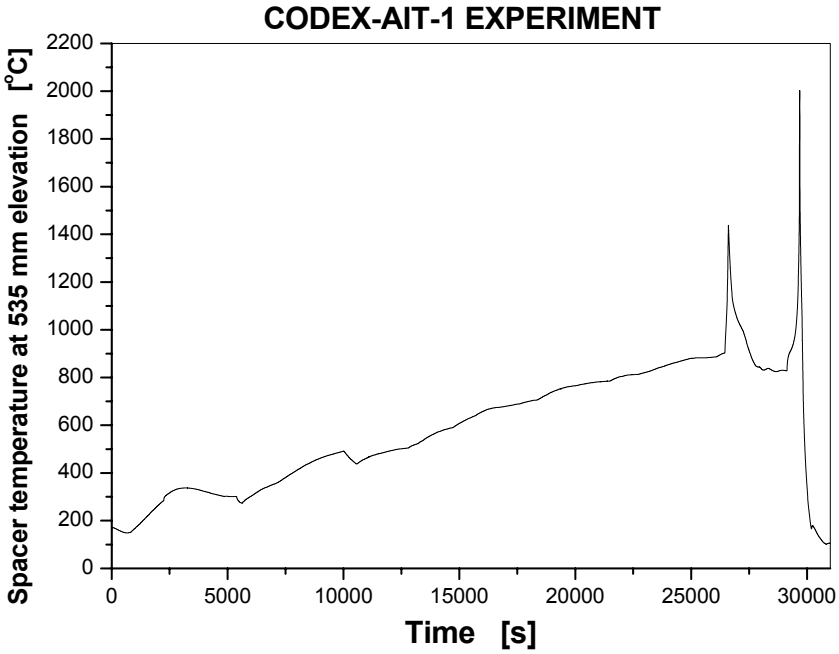

Fig. 11 Spacer temperature during the total recorded period

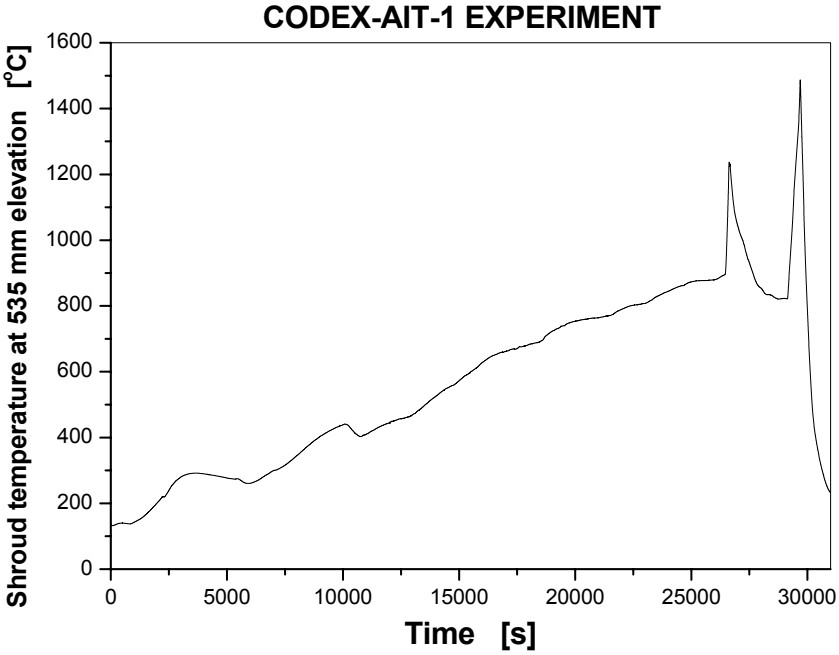

Fig. 12 Shroud temperature during the total recorded period

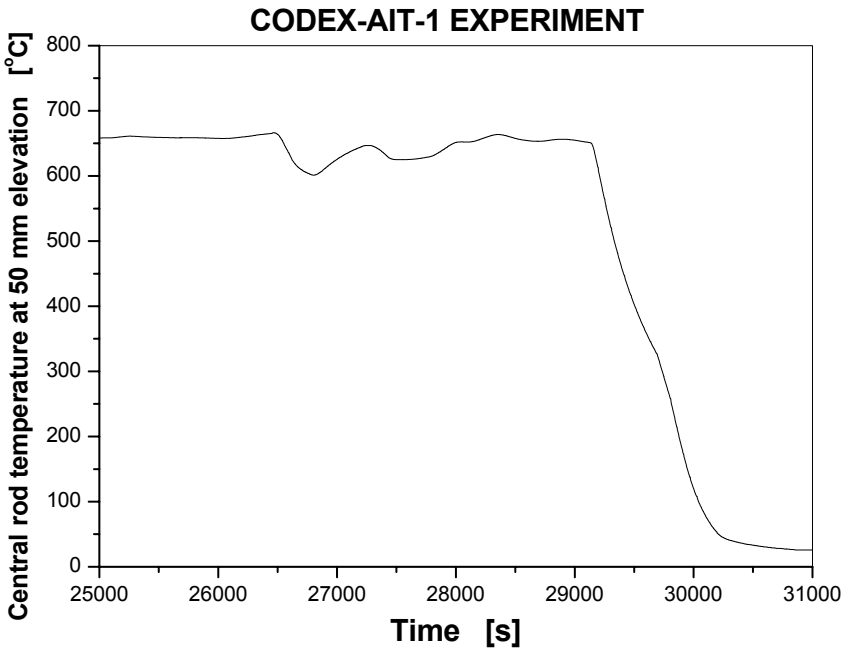

Fig. 13 UH50: Unheated rod temperature at 50 mm

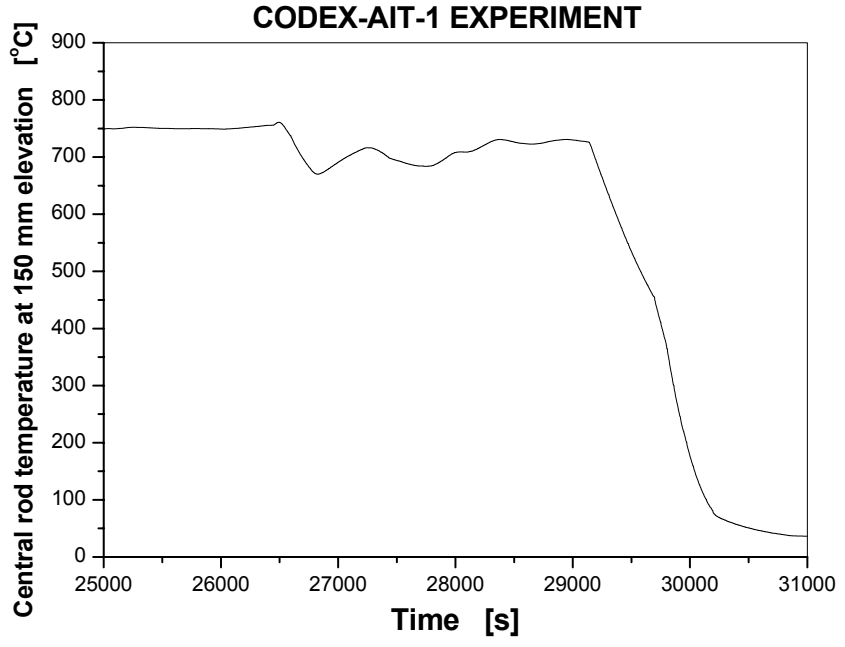

Fig. 14 UH150: Unheated rod temperature at 150 mm

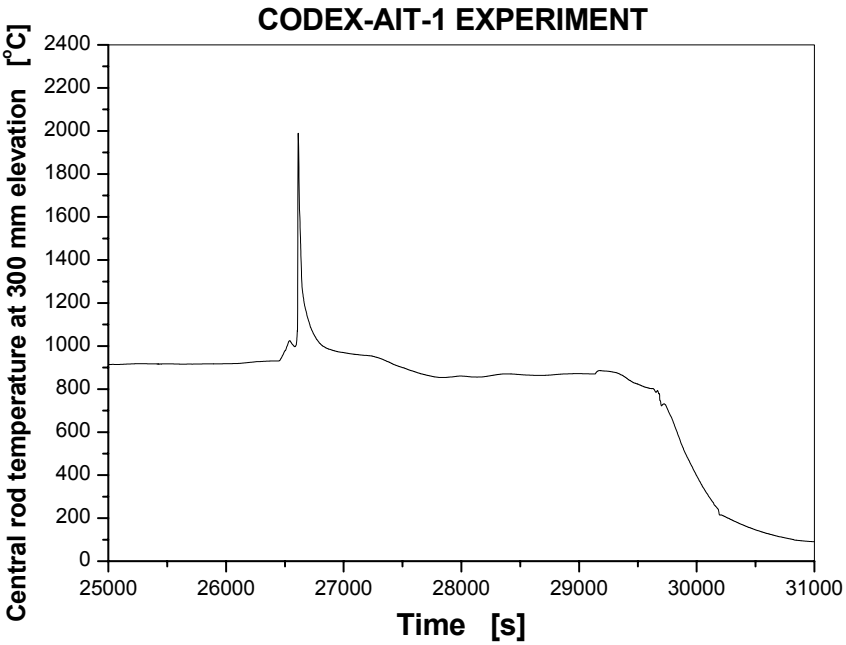

Fig. 15 UH300: Unheated rod temperature at 300 mm

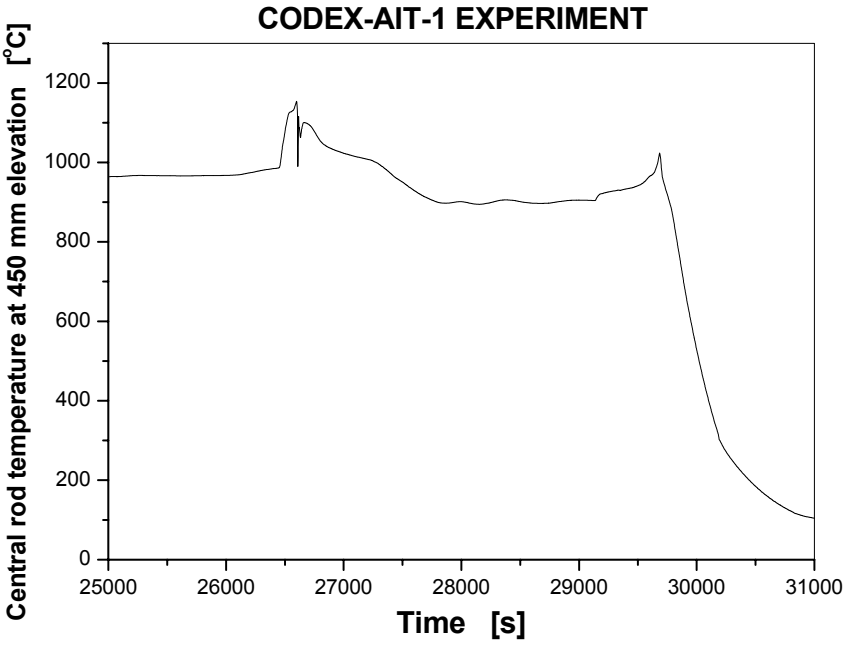

Fig. 16 UH450: Unheated rod temperature at 450 mm

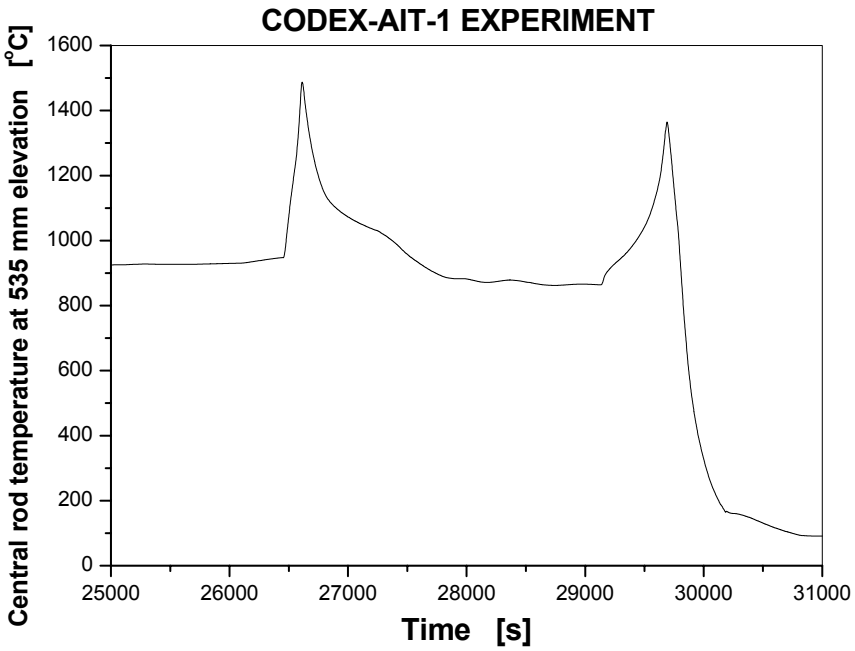

Fig. 17 UH535: Unheated rod temperature at 535 mm

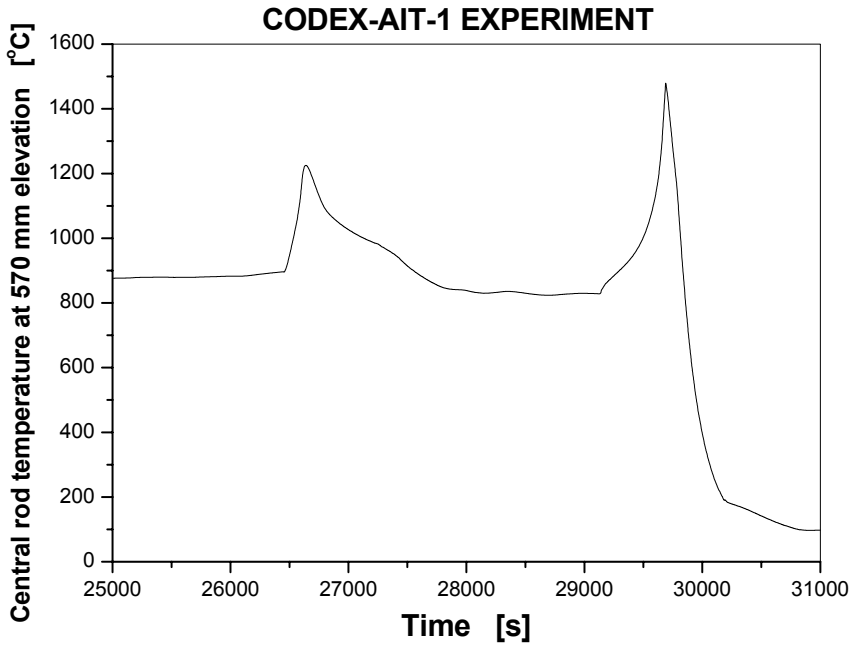

Fig. 18 UH570: Unheated rod temperature at 570 mm

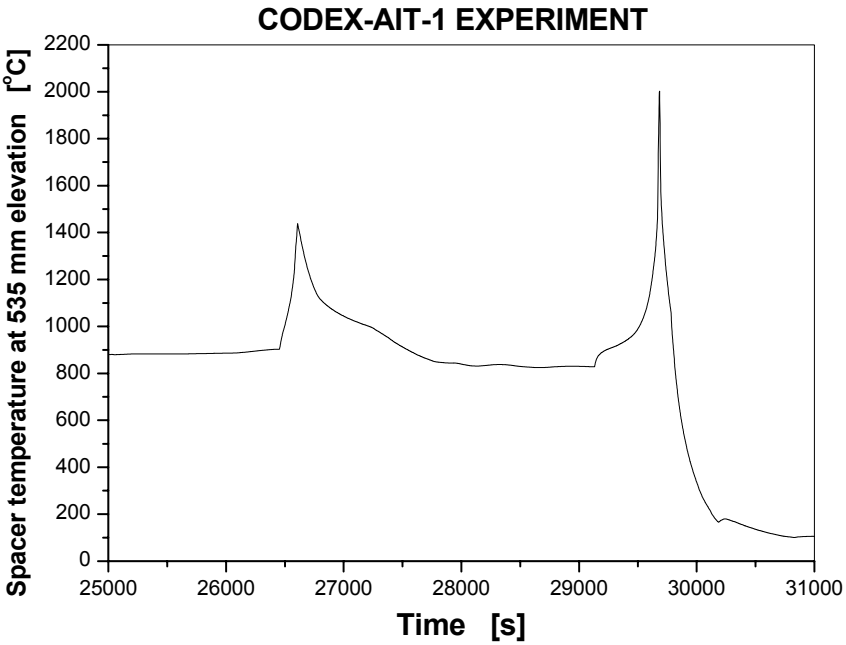

Fig. 19 SP535: Spacer temperature at 535 mm

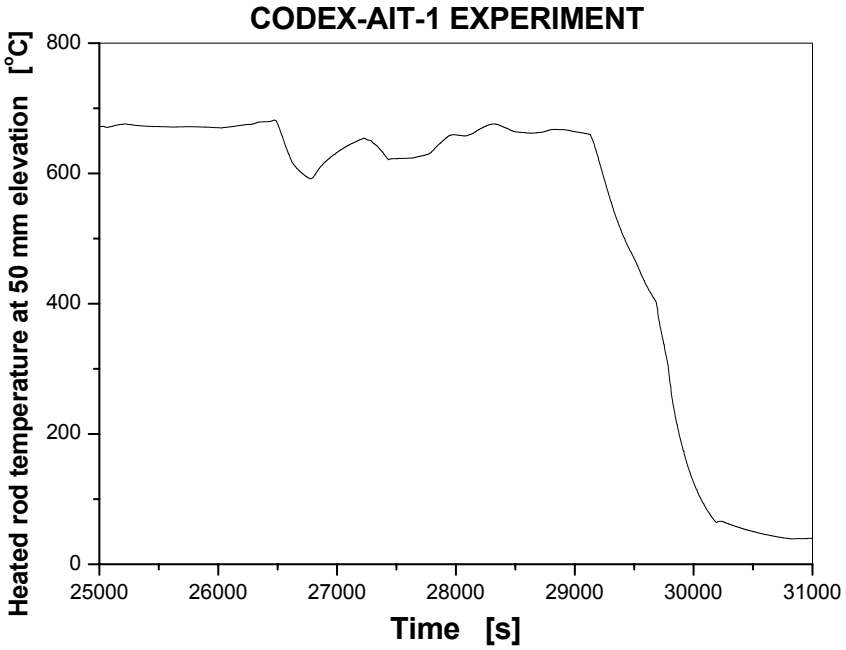

Fig. 20 H50: Heated rod temperature at 50 mm

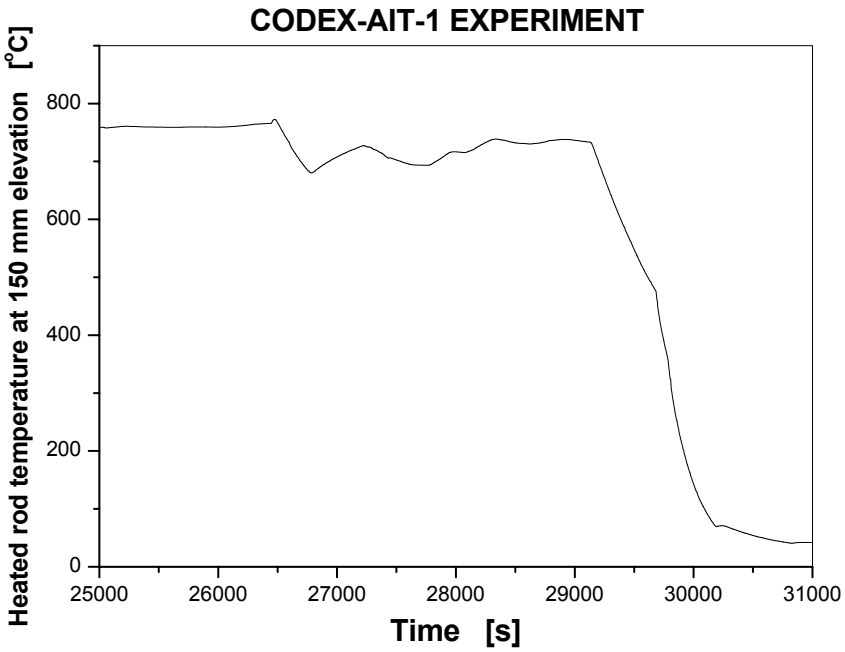

Fig. 21 H150: Heated rod temperature at 150 mm

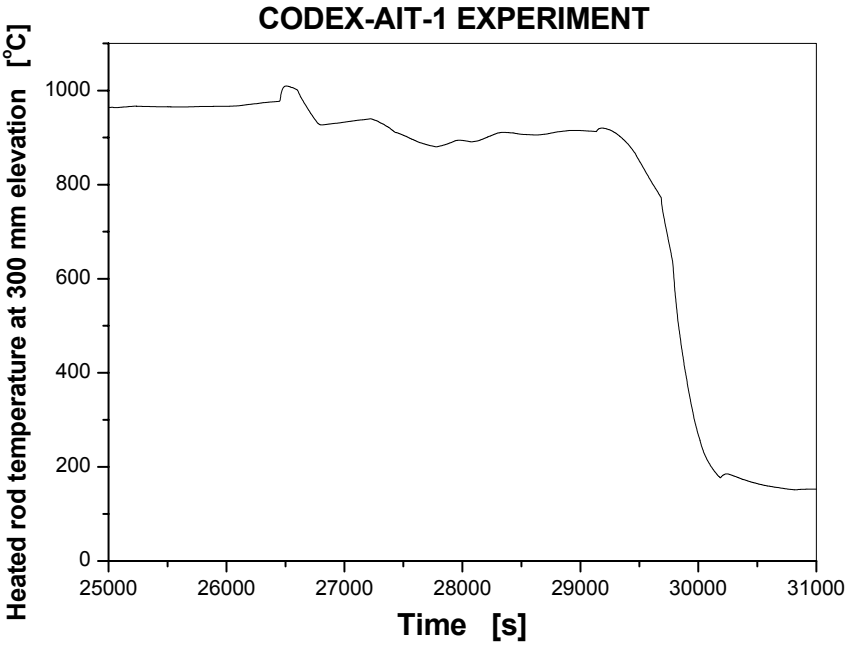

Fig. 22 H300: Heated rod temperature at 300 mm

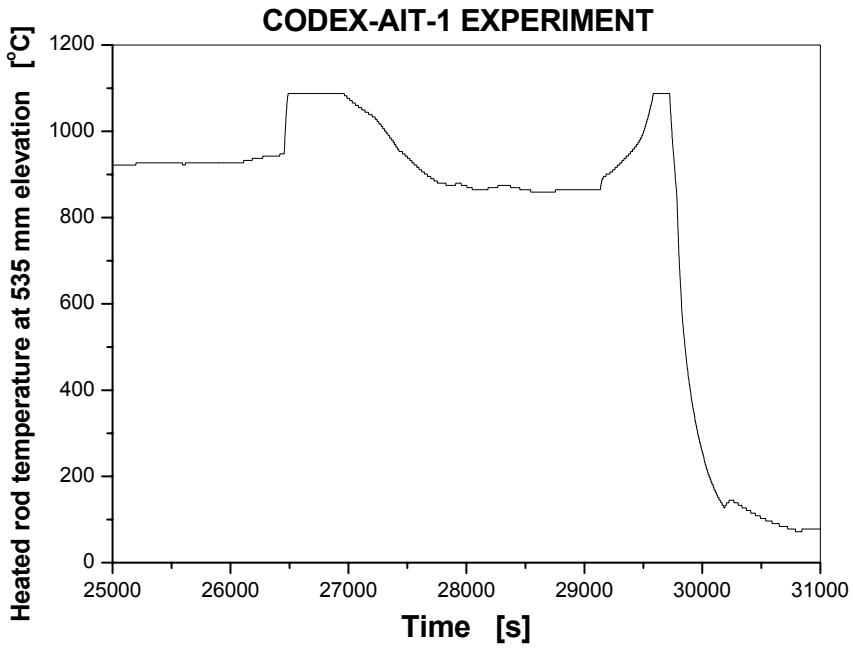

Fig. 23 H535: Heated rod temperature at 535 mm

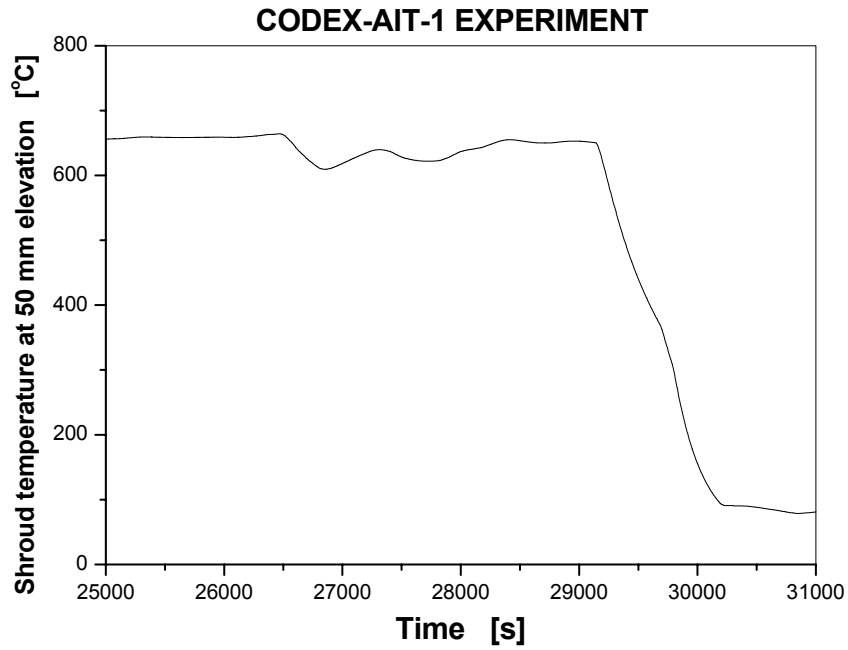

Fig. 24 SH50: Shroud temperature at 50 mm

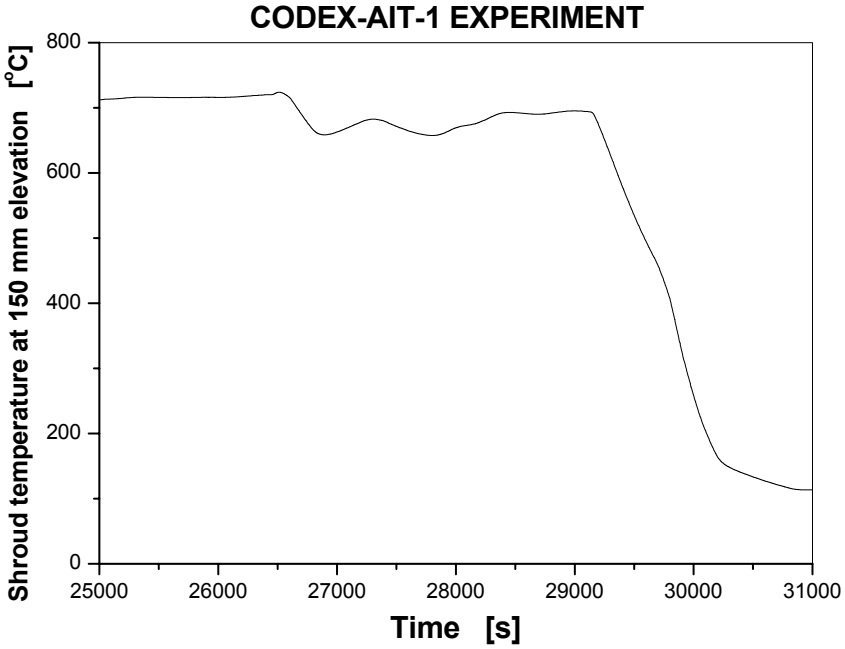

Fig. 25 SH150: Shroud temperature at 150 mm

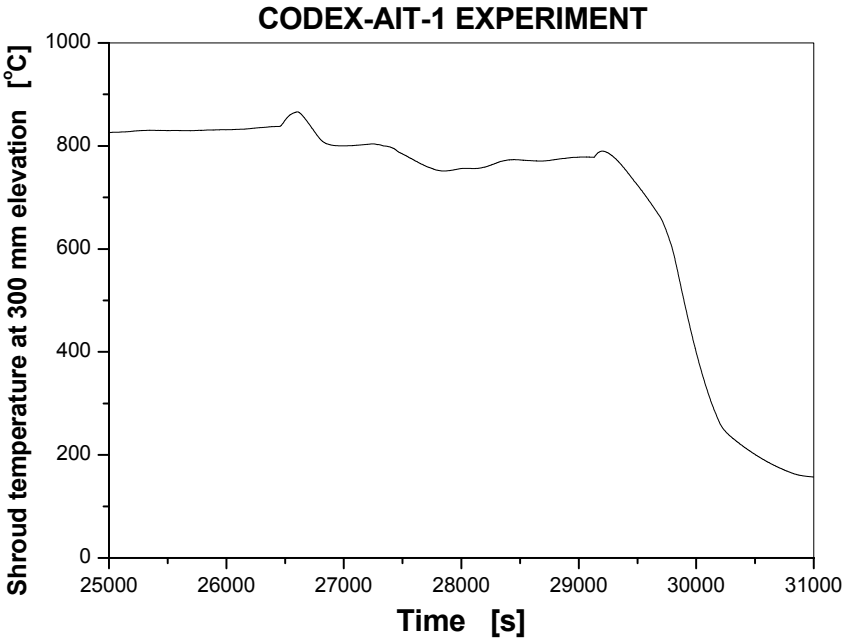

Fig. 26 SH300: Shroud temperature at 300 mm

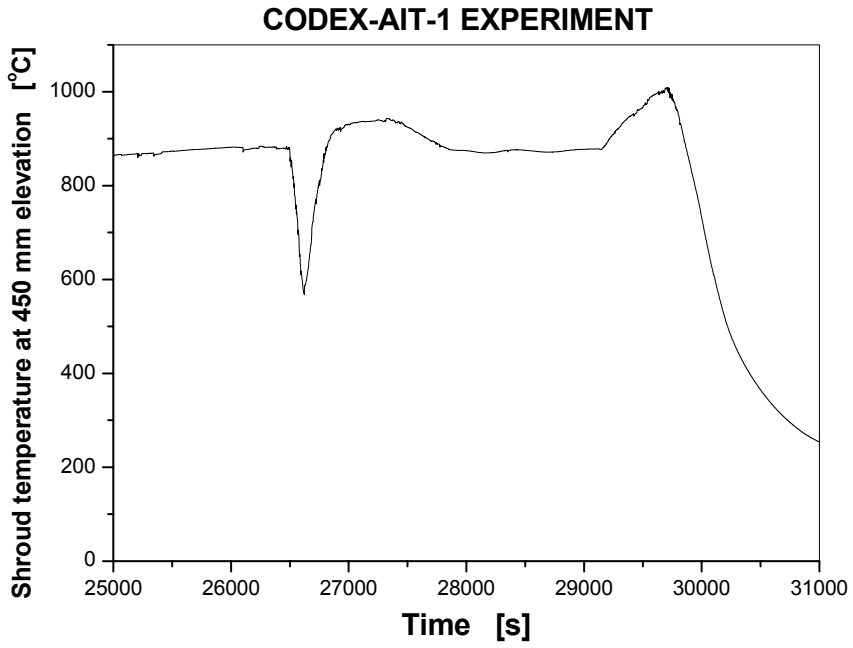

Fig. 27 SH450: Shroud temperature at 450 mm

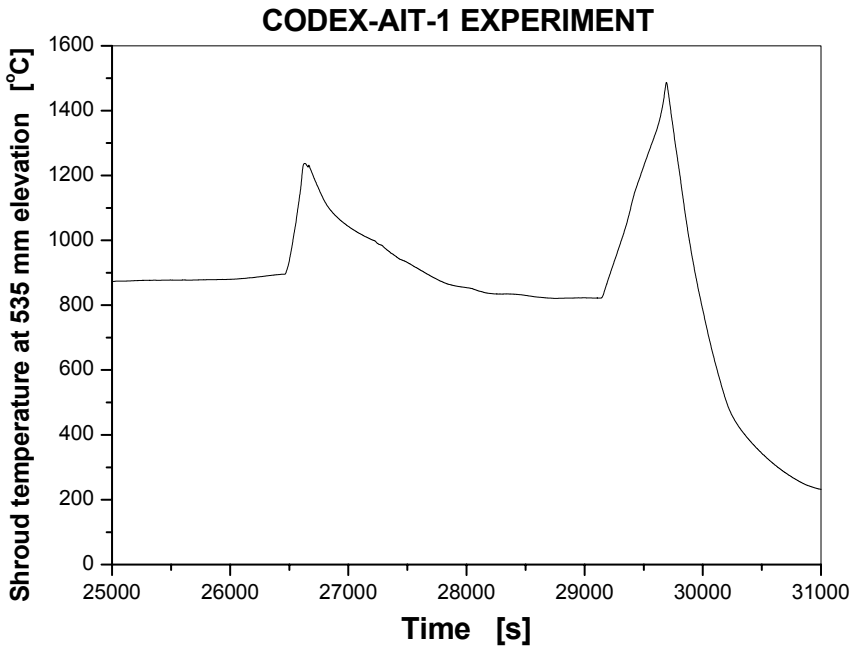

Fig. 28 SH535: Shroud temperature at 535 mm

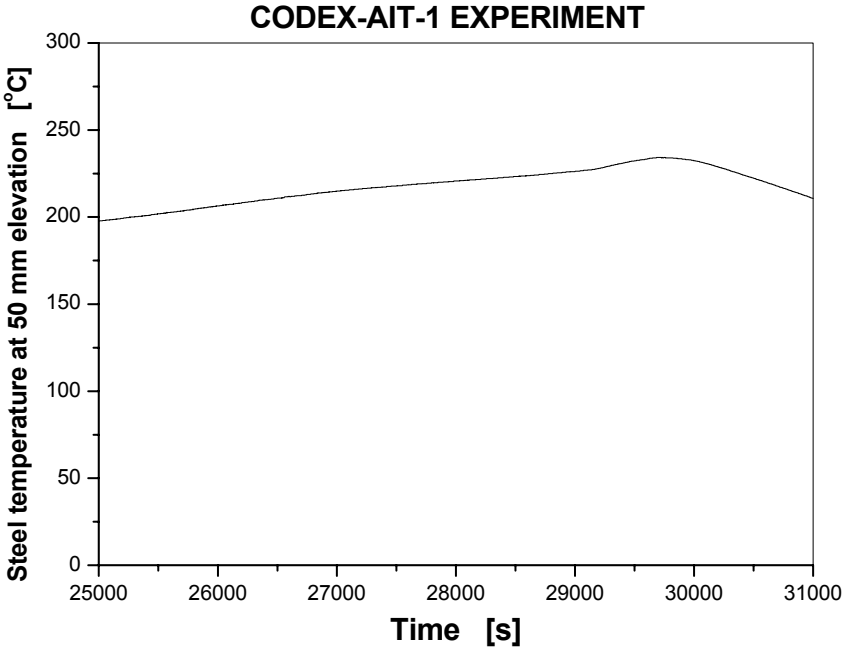

Fig. 29 HS50: Steel heat shield temperature at 50 mm

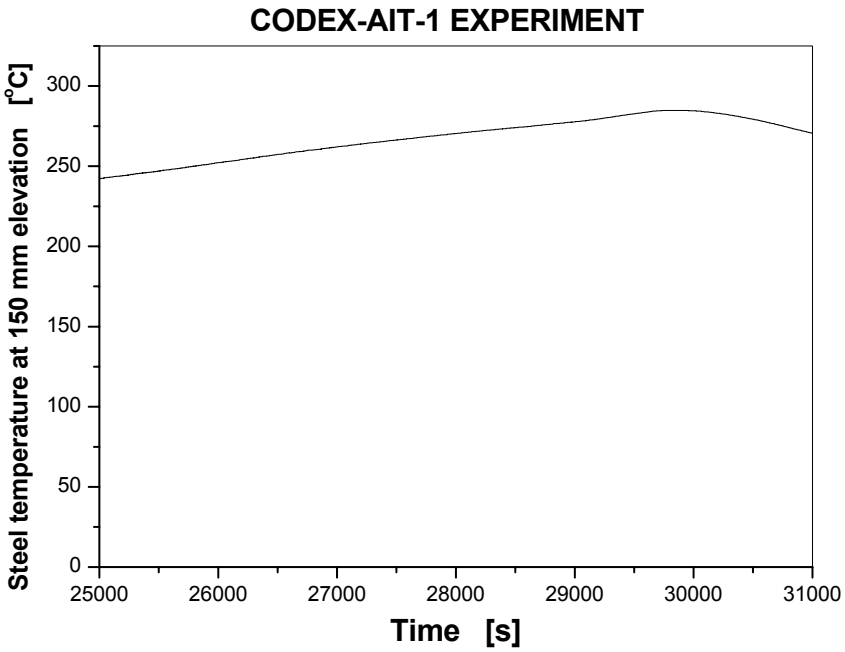

Fig. 30 HS150: Steel heat shield temperature at 150 mm

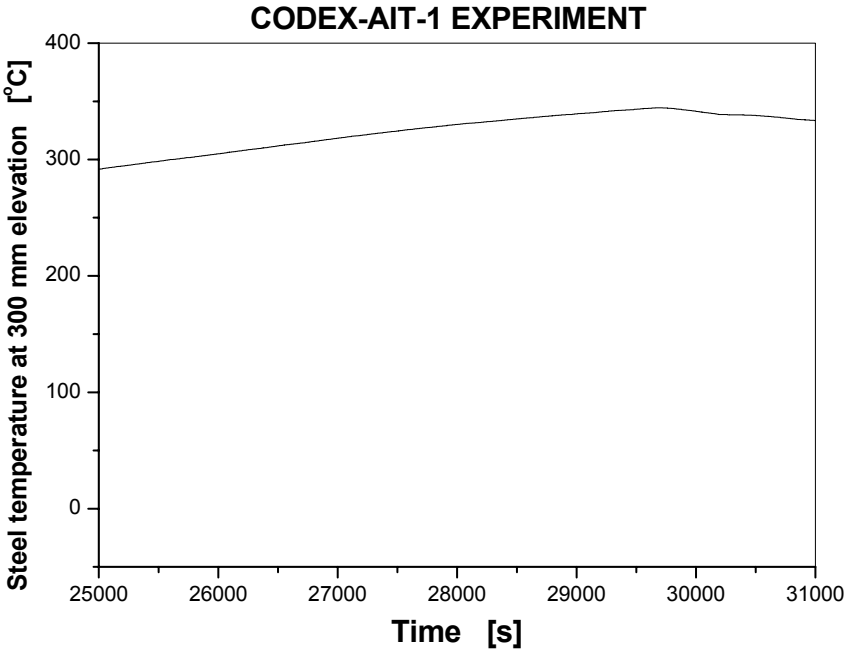

Fig. 31 HS300: Steel heat shield temperature at 300 mm

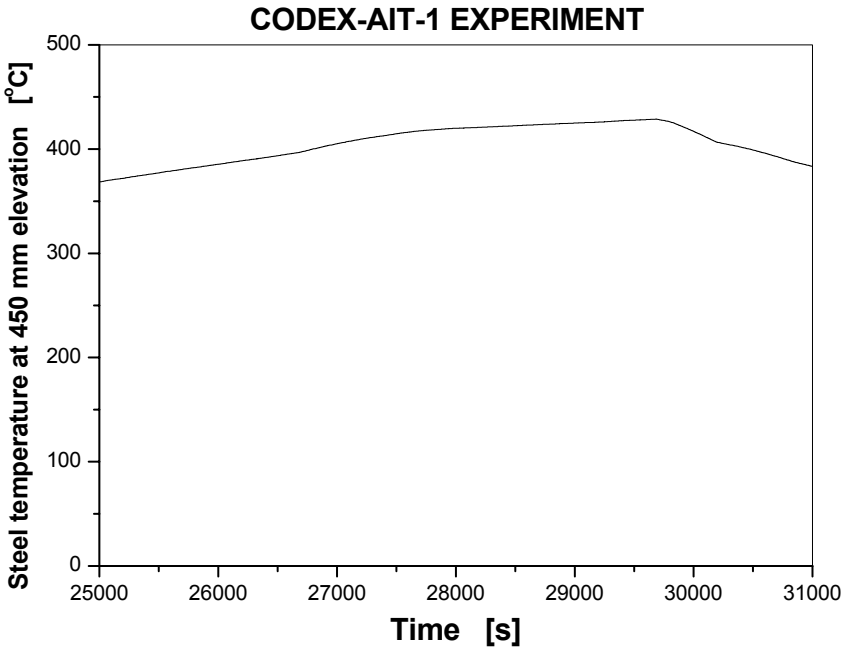

Fig. 32 HS450: Steel heat shield temperature at 450 mm

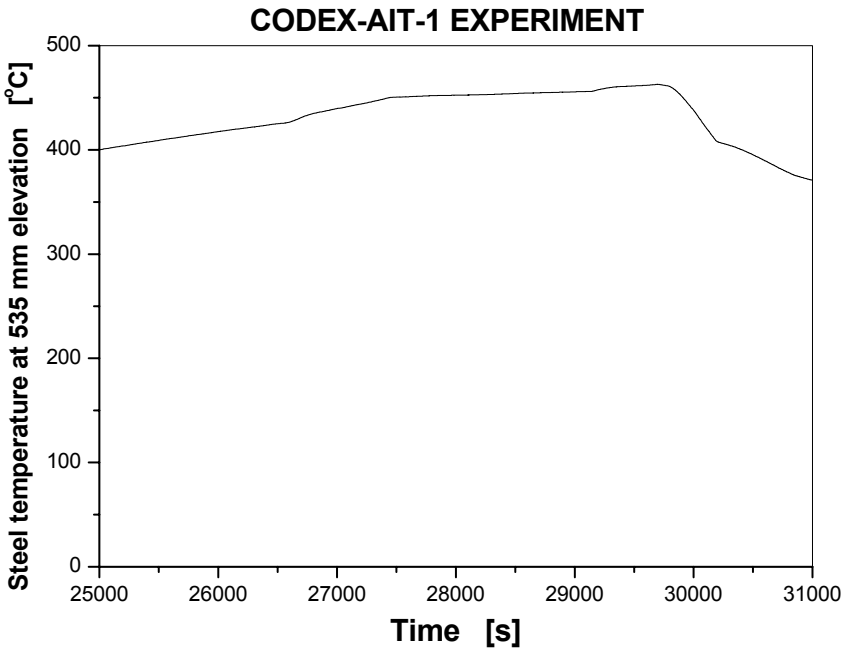

Fig. 33 HS535: Steel heat shield temperature at 535 mm

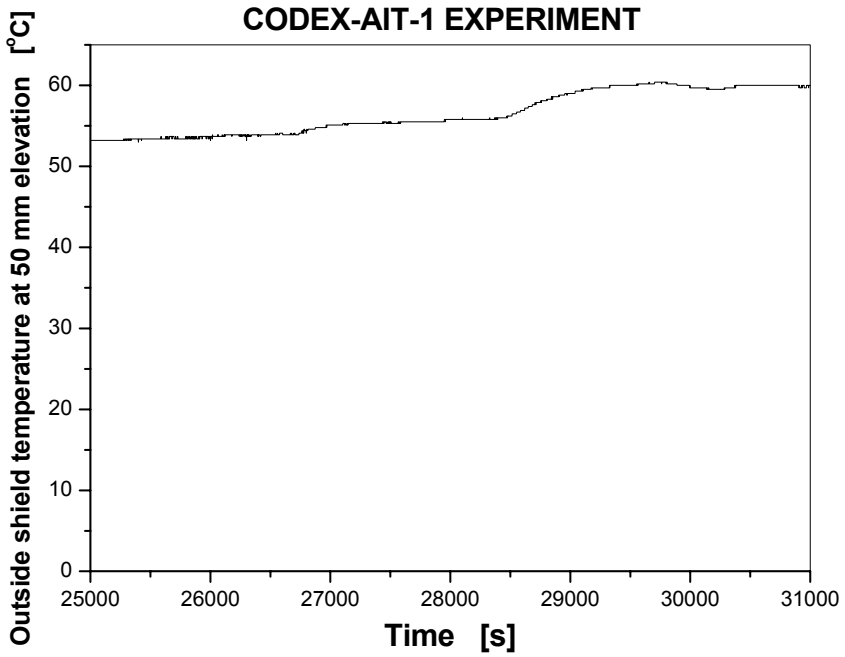

Fig. 34 OS50: Outside shield temperature at 50 mm

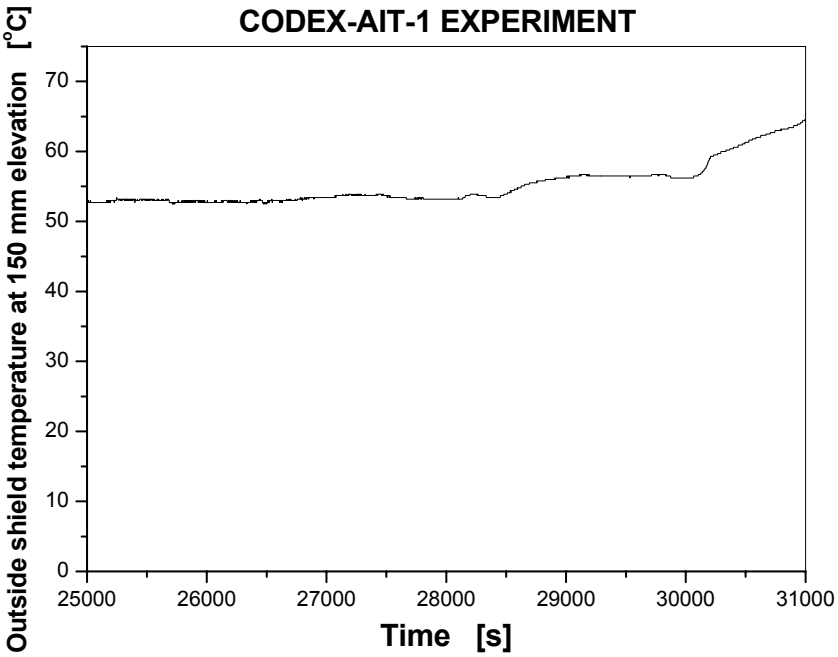

Fig. 35 OS150: Outside shield temperature at 150 mm

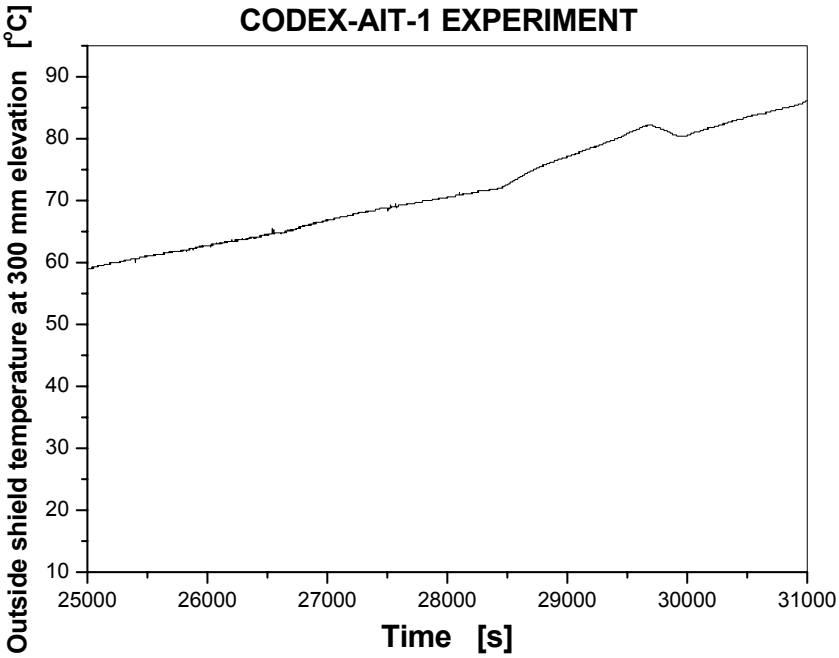

Fig. 36 OS300: Outside shield temperature at 300 mm

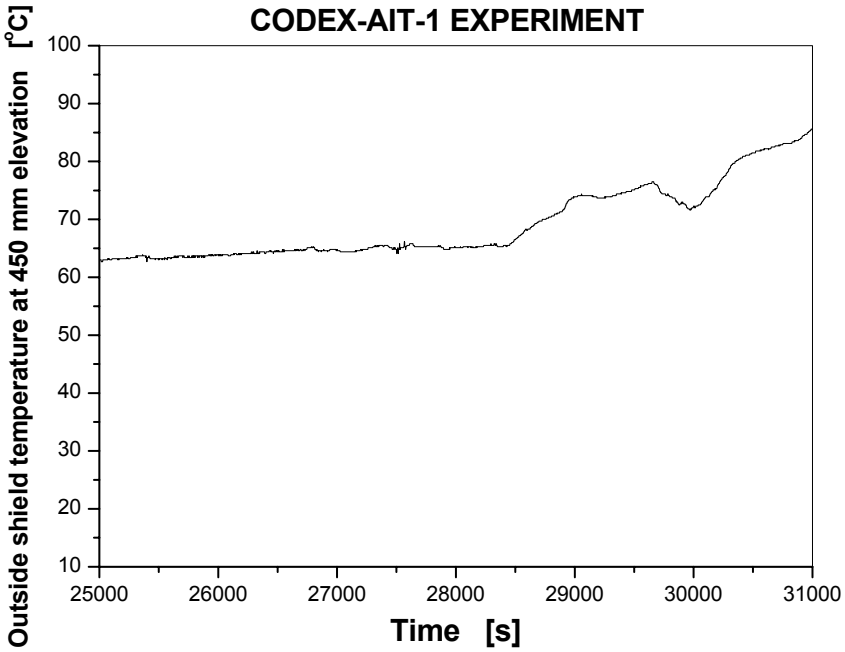

Fig. 37 OS450: Outside shield temperature at 450 mm

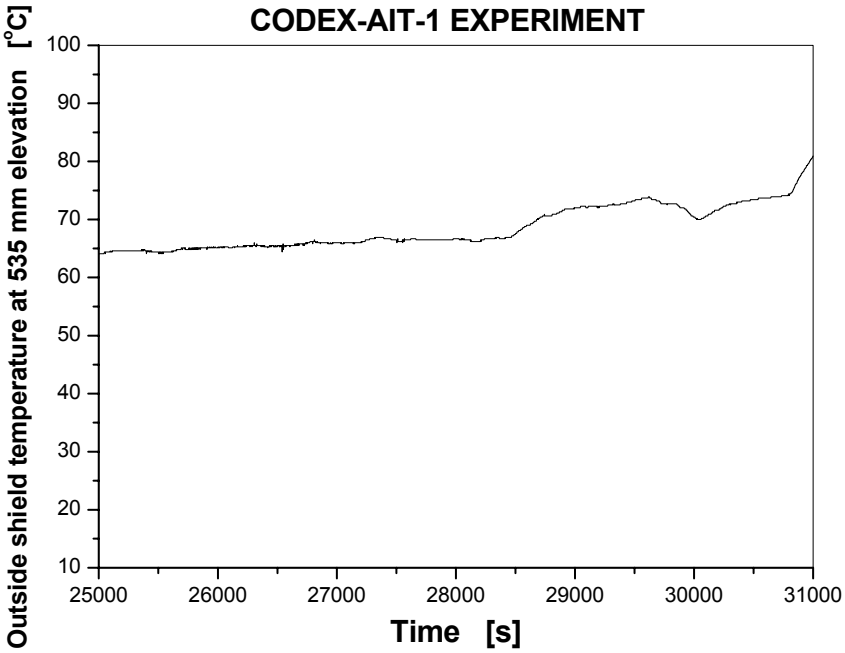

Fig. 38 OS535: Outside shield temperature at 535 mm

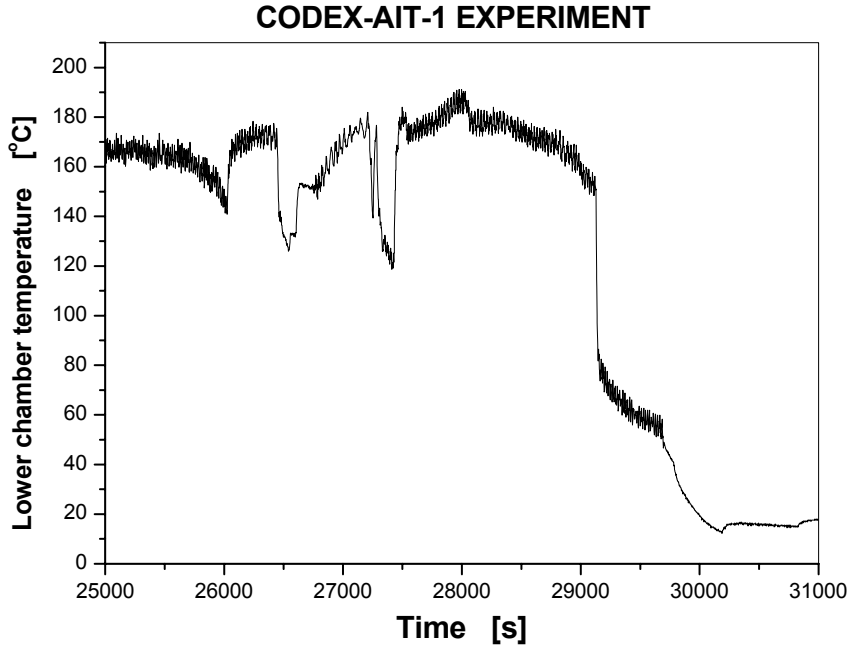

Fig. 39 TLOCH: Lower chamber temperature

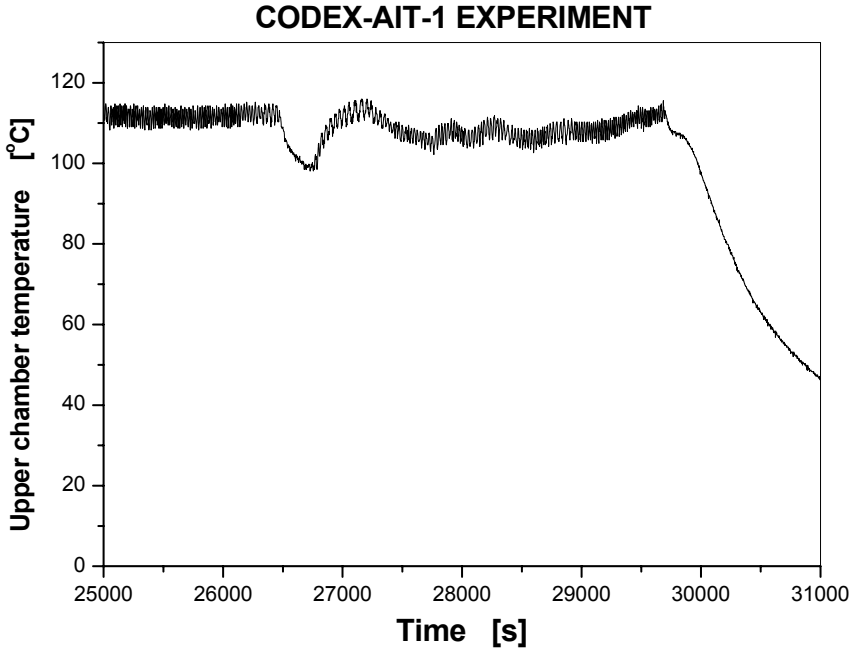

Fig. 40 TUPCH: Upper chamber temperature

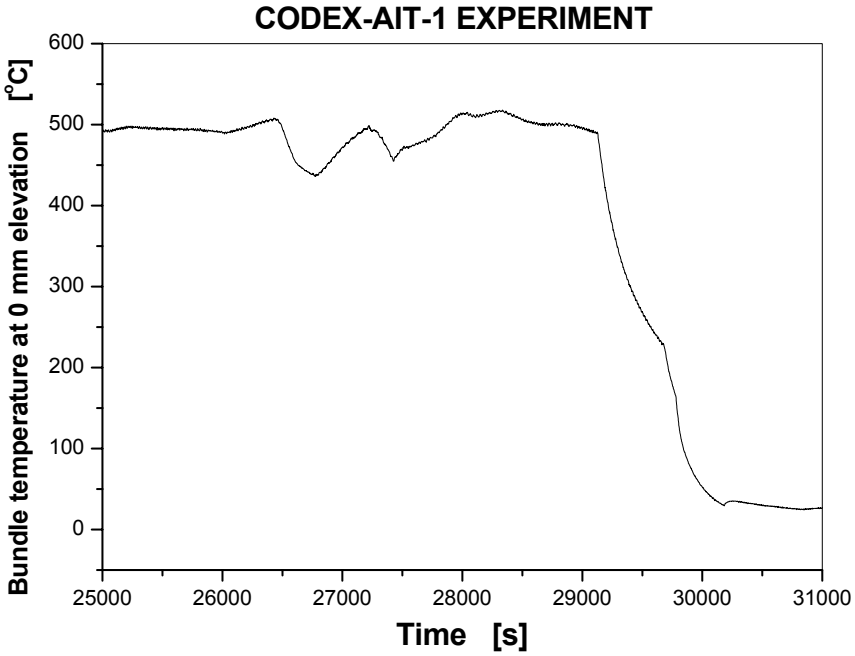

Fig. 41 TMELT: Bundle temperature at 0 mm

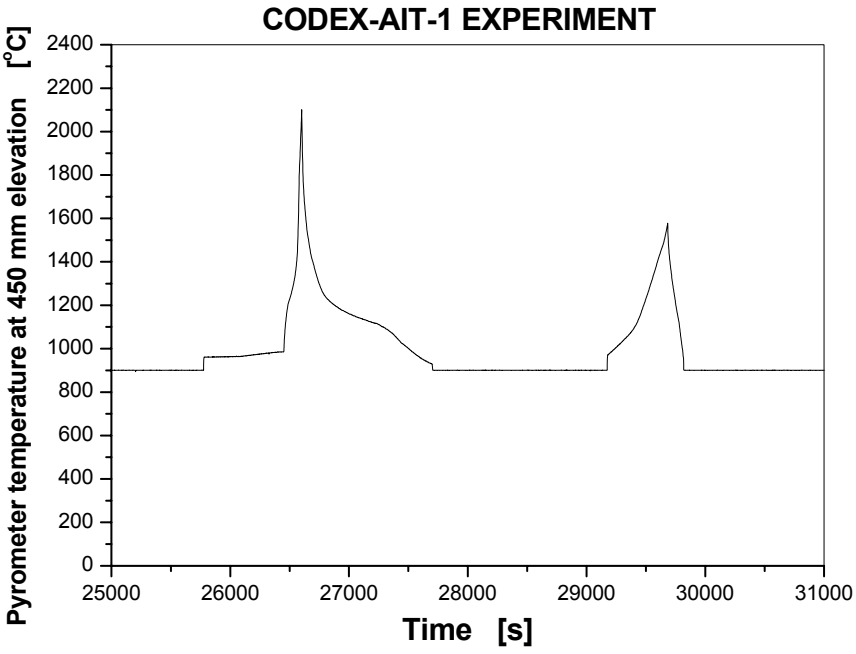

Fig. 42 PYR450: Pyrometer temperature at 450 mm

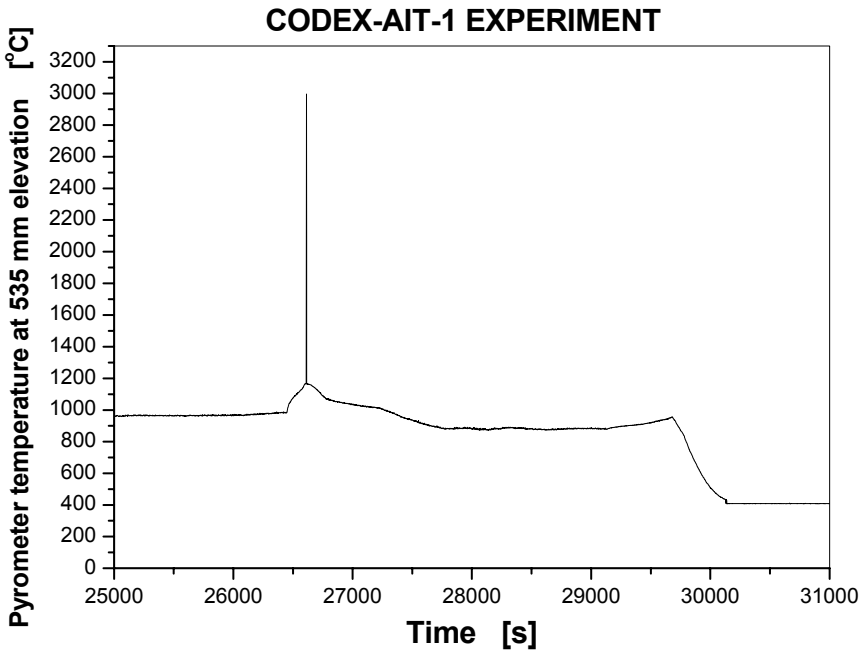

Fig. 43 PYR535: Pyrometer temperature at 535 mm

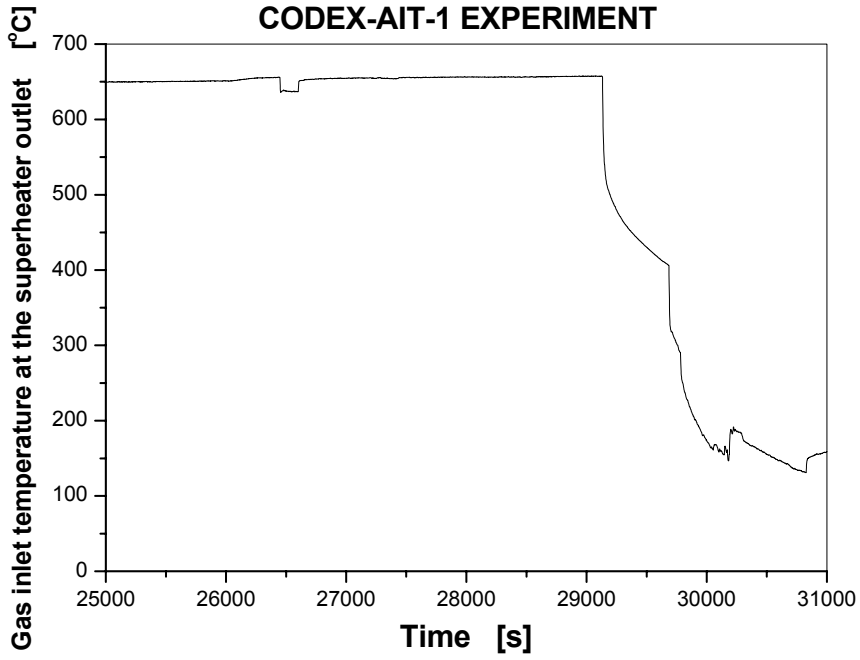

Fig. 44 TIN1: Gas temperature at the superheater outlet

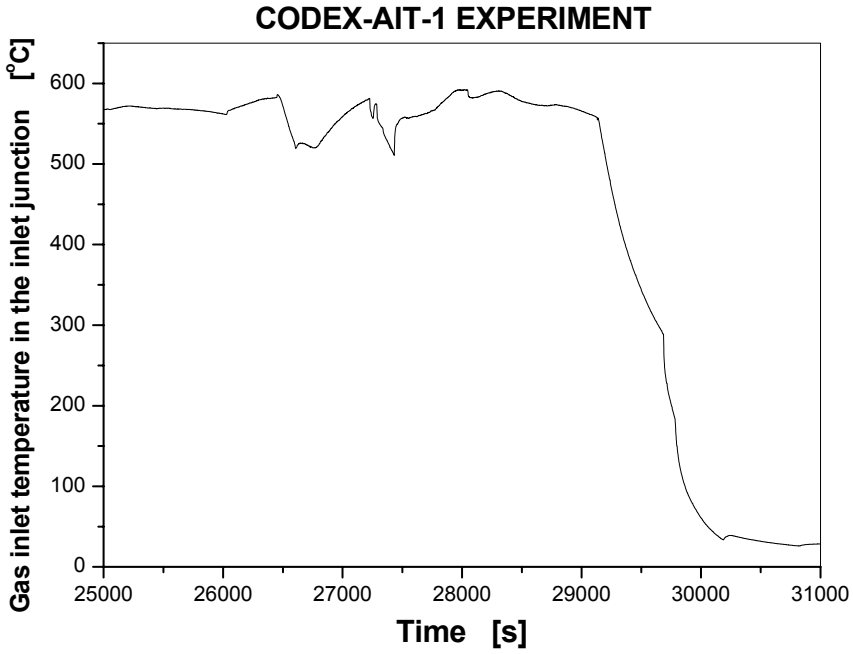

Fig. 45 TIN2: Gas temperature in the inlet junction

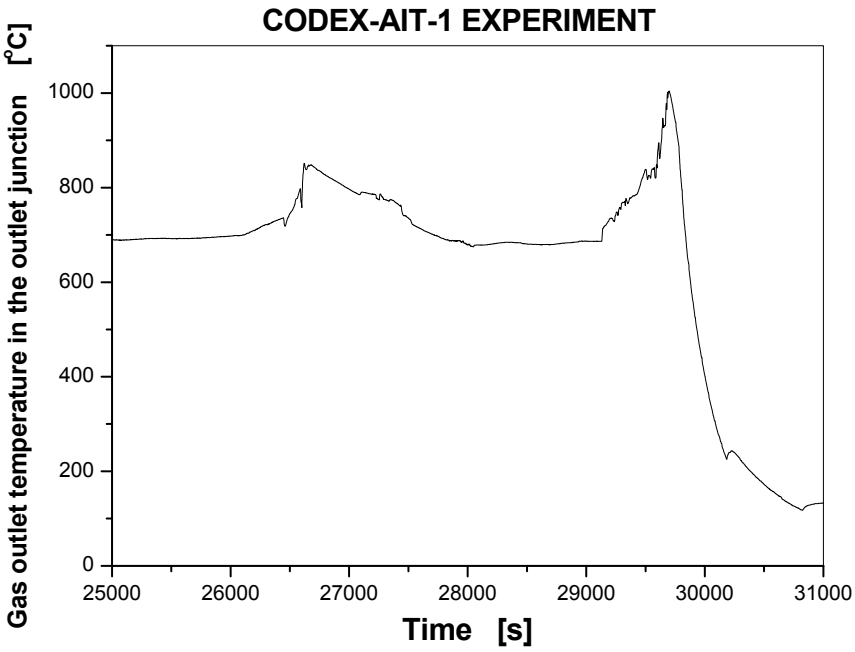

Fig. 46 TCOUT: Gas temperature in the outlet junction

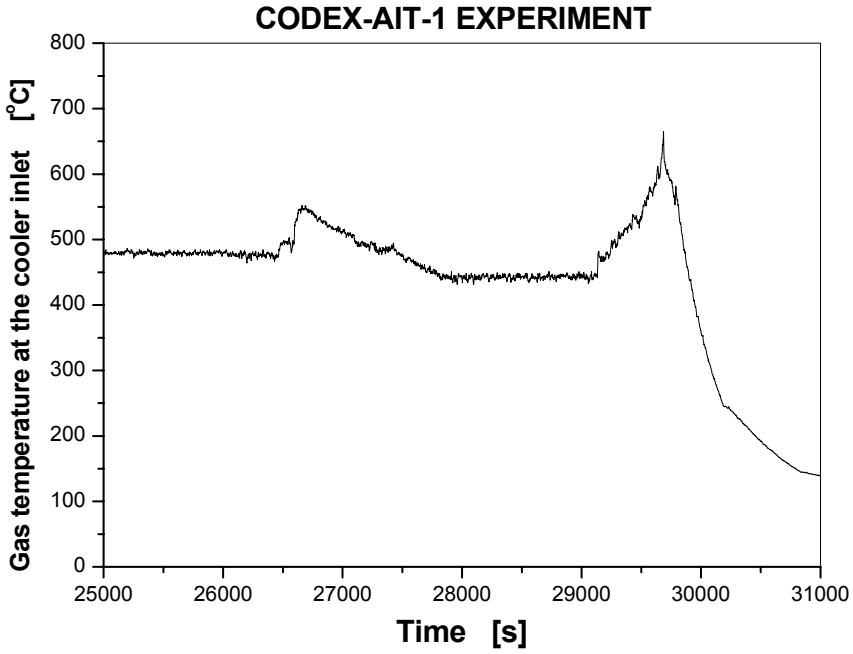

Fig. 47 TCOOL: Gas temperature at the cooler inlet

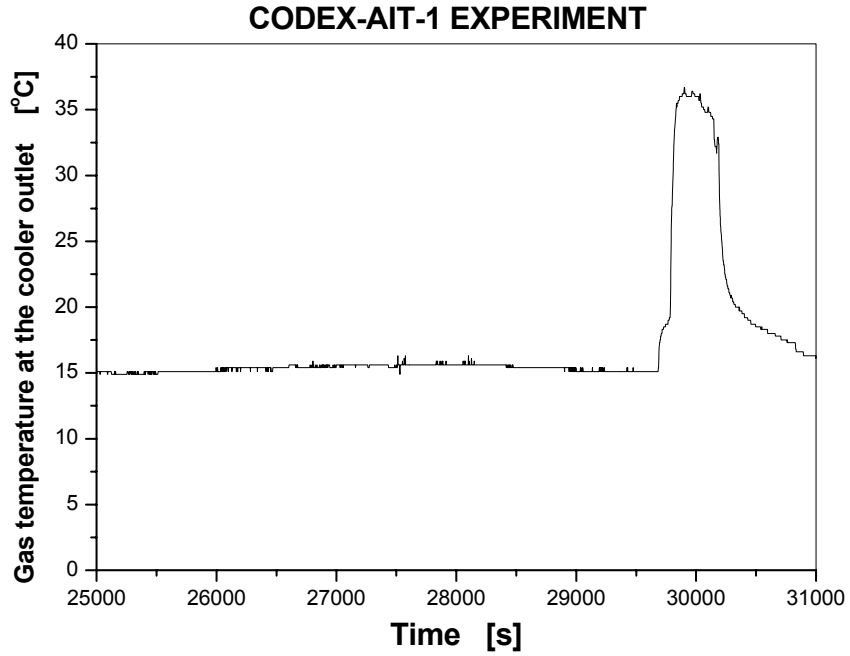

Fig. 48 TOUTC: Gas temperature at the cooler outlet

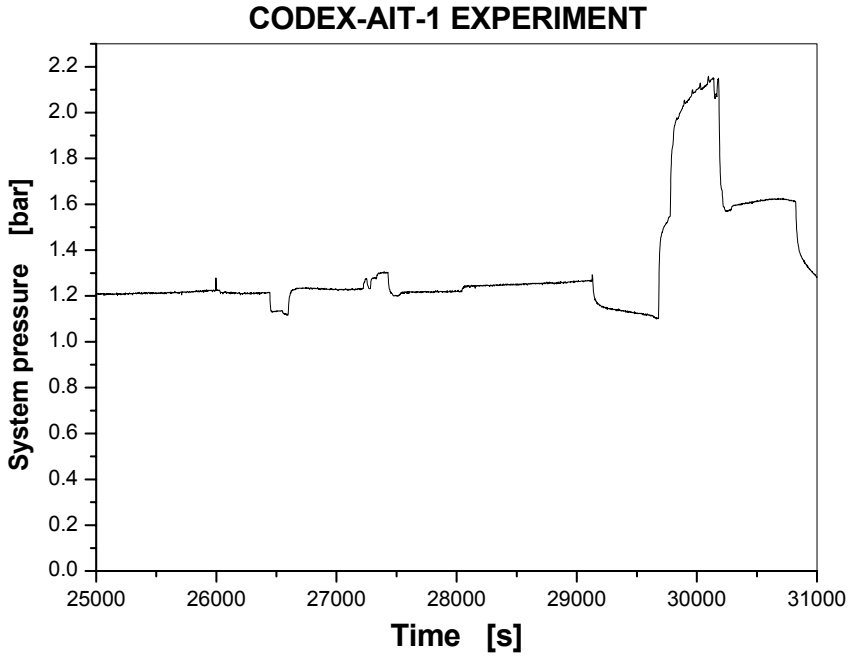

Fig. 49 PSYS: System pressure

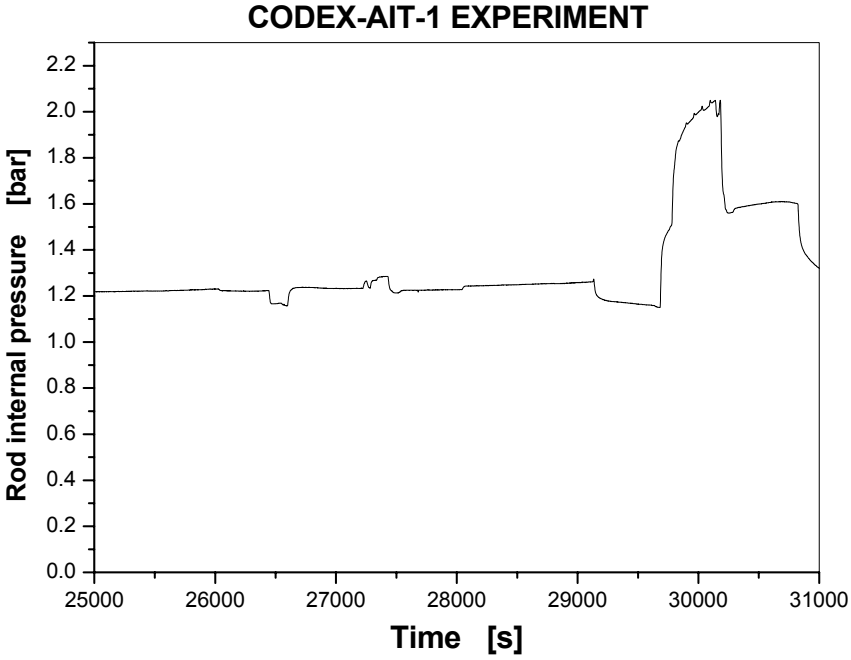

Fig. 50 PINS: Rod internal pressure

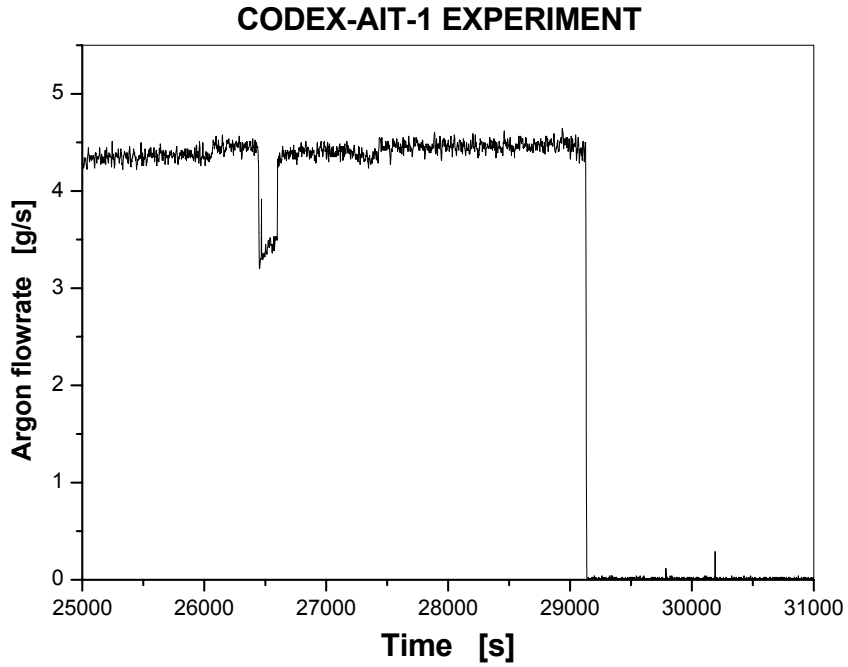

Fig. 51 ARGON: Argon flowrate

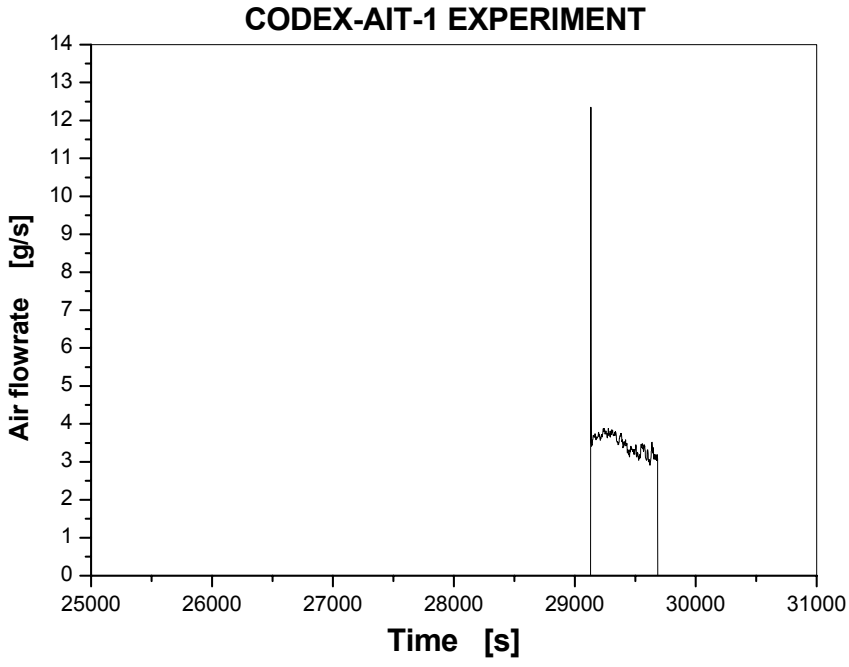

Fig. 52 AIR: Air flowrate

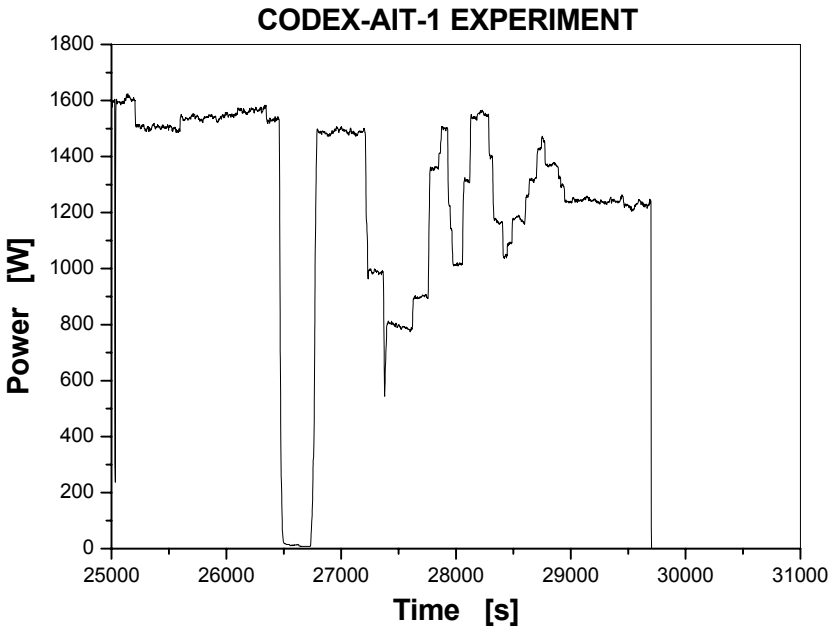

Fig. 53 POWER: Electric power

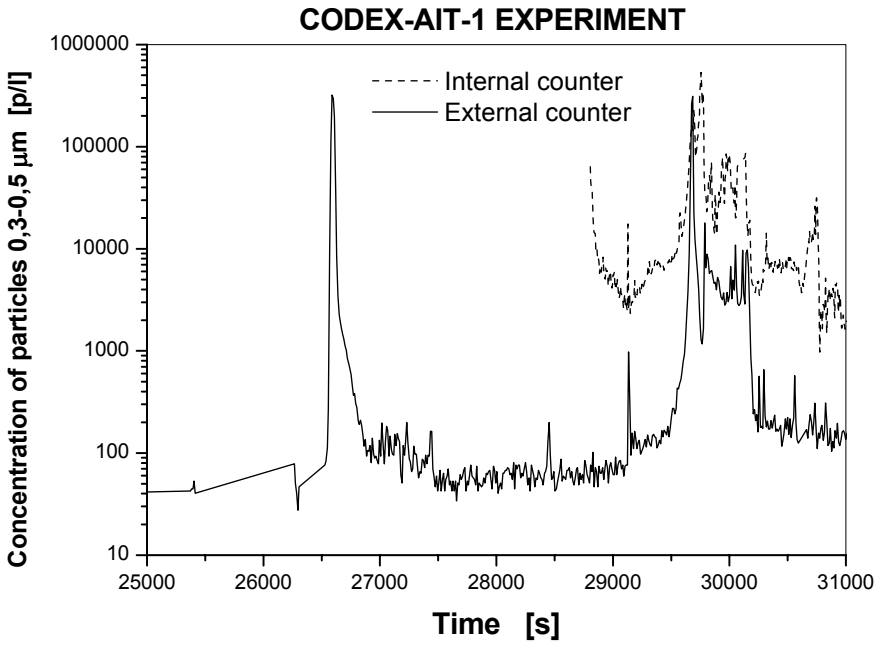

Fig. 54 API1 and APE1: Concentration of 0,3-0,5 µm aerosols

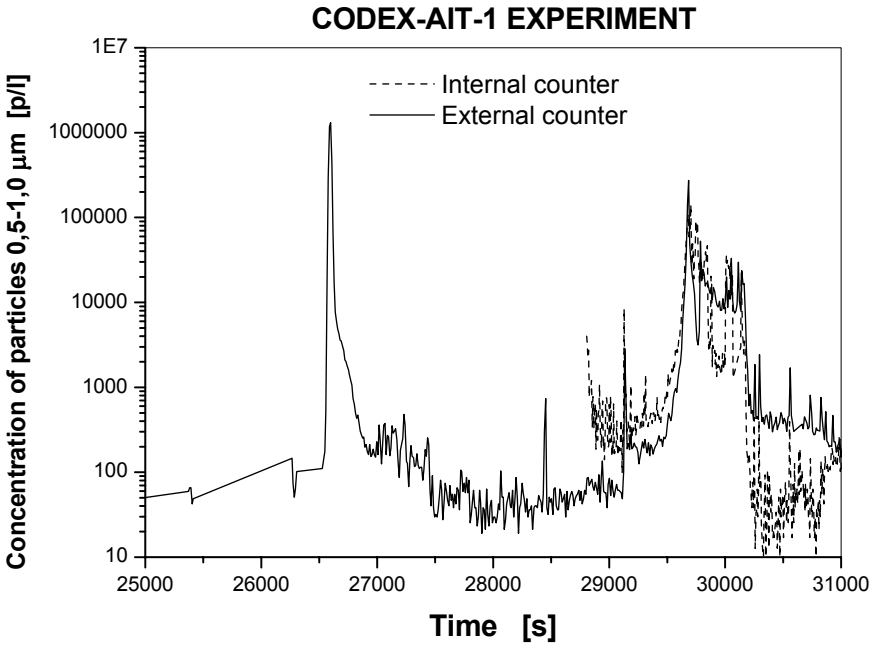

Fig. 55 API2 and APE2: Concentration of 0,5-1,0 µm aerosols

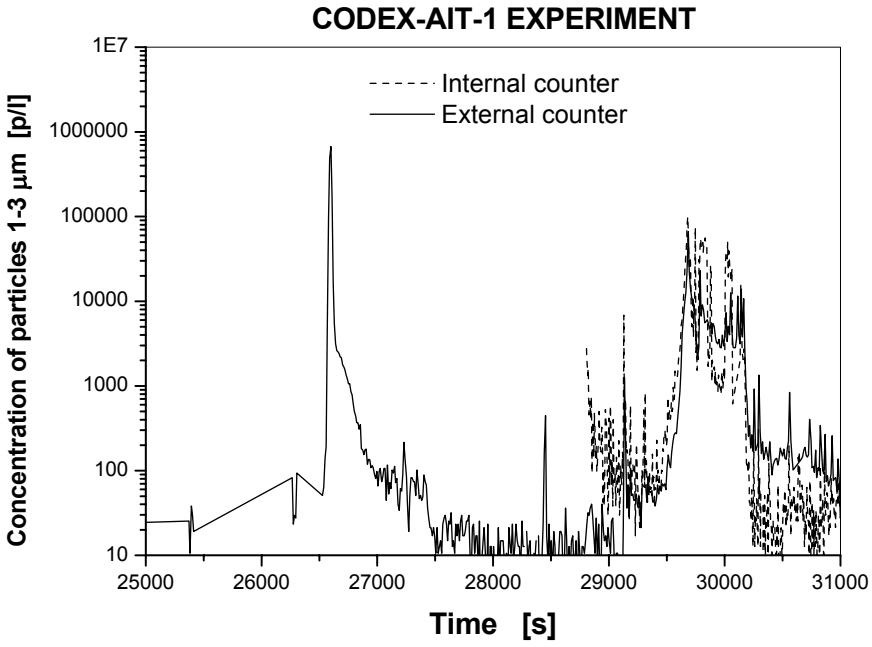

Fig. 56 API3 and APE3: Concentration of 1-3 µm aerosols

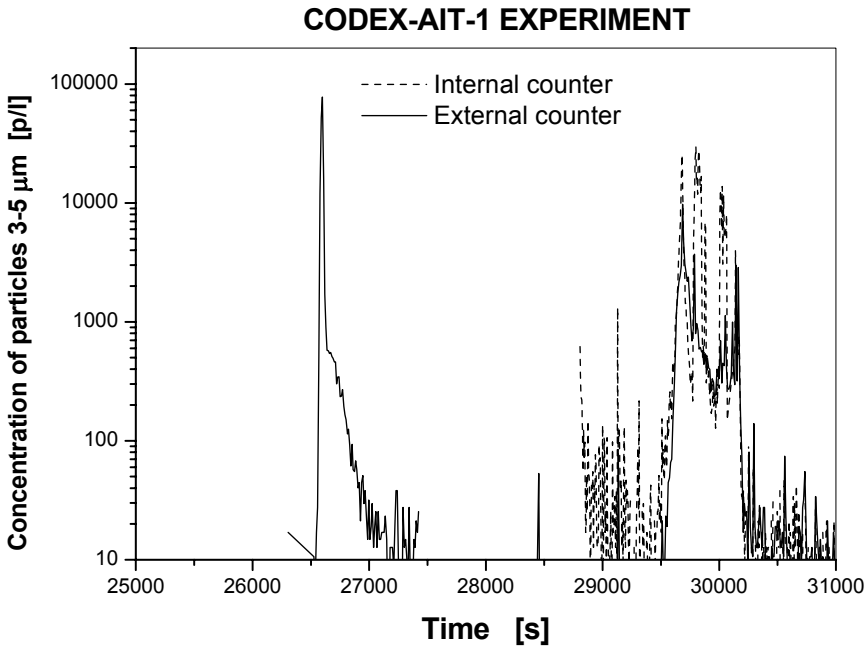

Fig. 57 API4 and APE4: Concentration of 3-5 μm aerosols

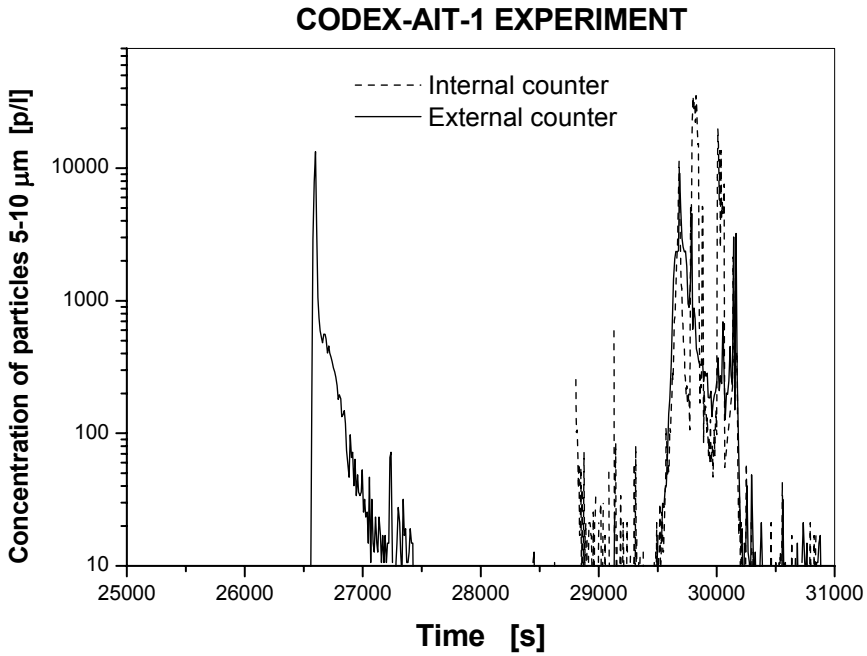

Fig. 58 API5 and APE5: Concentration of 5-10 μm aerosols

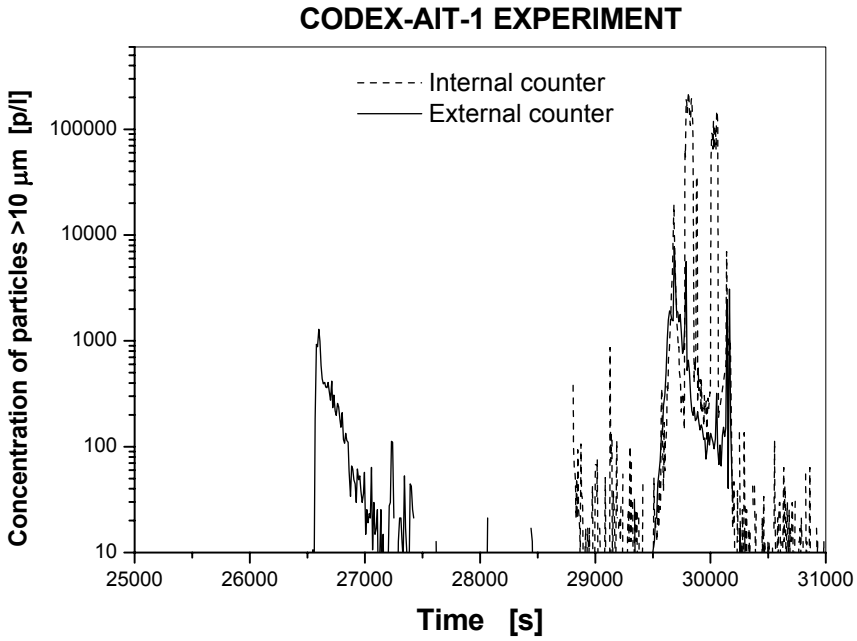

Fig. 59 API6 and APE6: Concentration of >10 μm aerosols

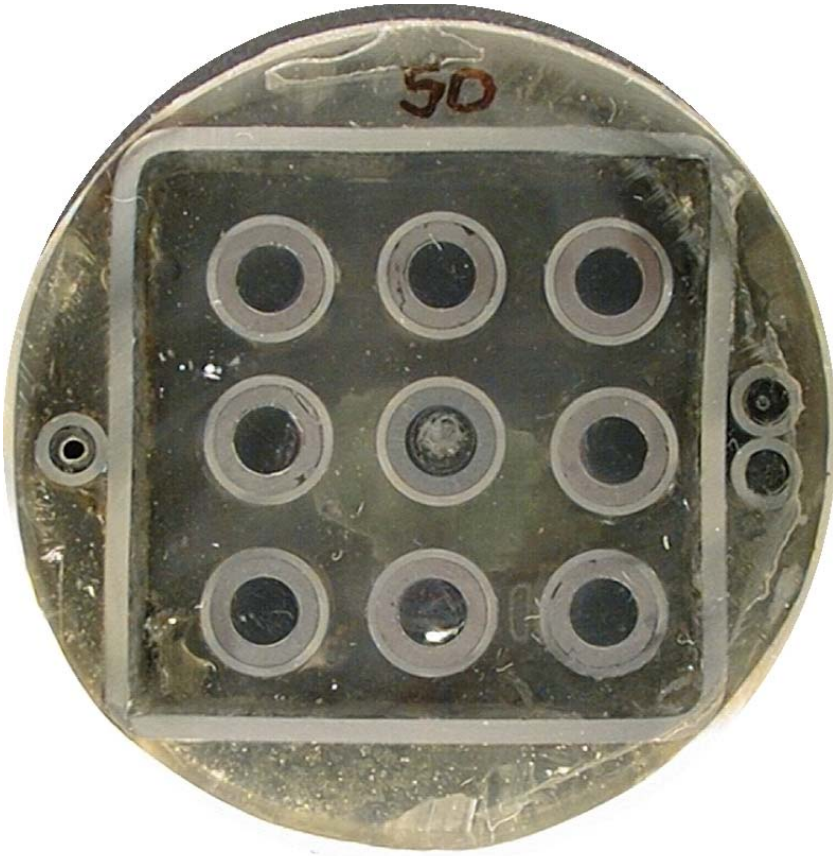

Fig. 60 Cross section of CODEX-AIT-1 bundle at 50 mm elevation

Fig. 61 Cross section of CODEX-AIT-1 bundle at 150 mm elevation

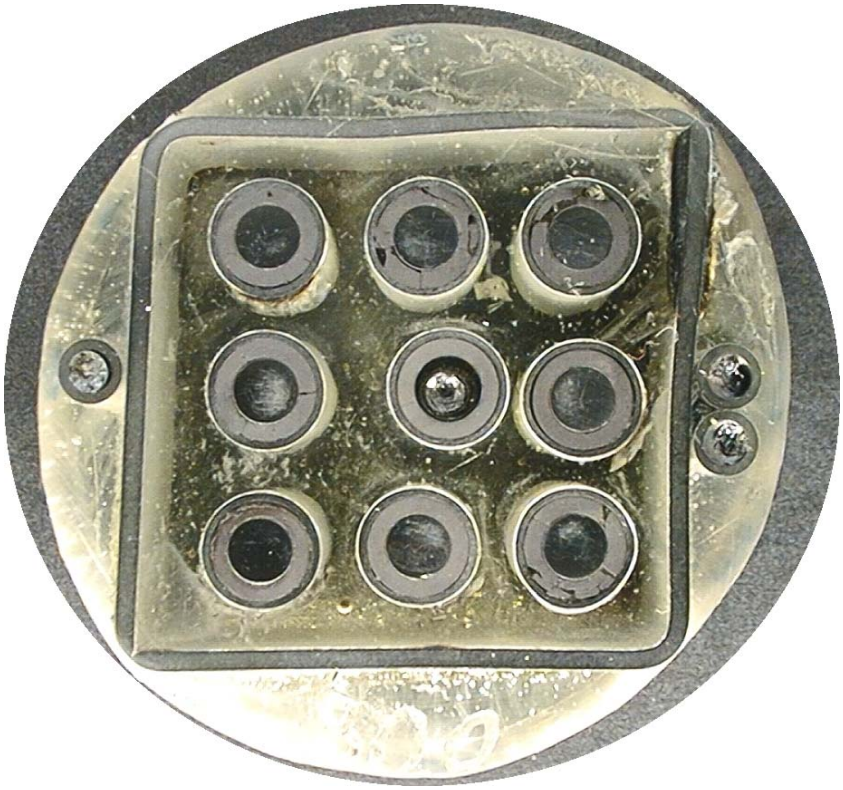

Fig. 62 Cross section of CODEX-AIT-1 bundle at 300 mm elevation

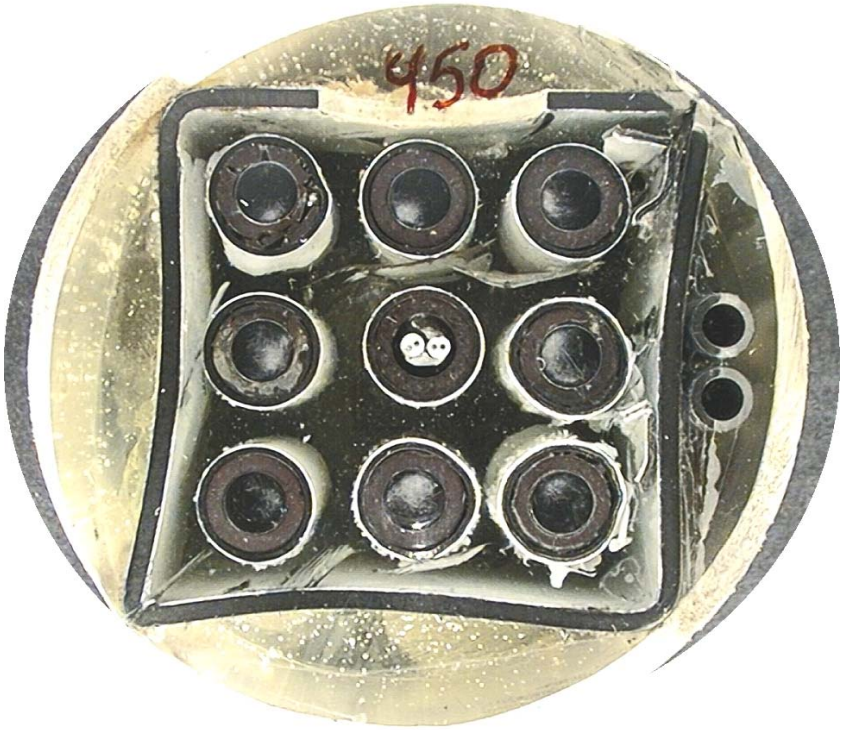

Fig. 63 Cross section of CODEX-AIT-1 bundle at 450 mm elevation

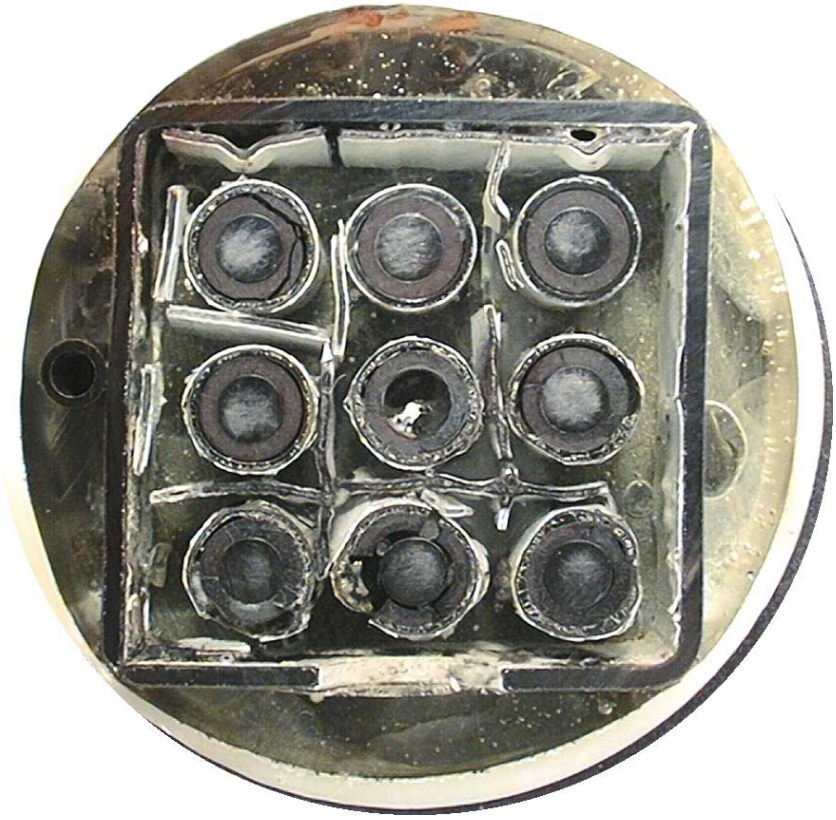

Fig. 64 Cross section of CODEX-AIT-1 bundle at 535 mm elevation

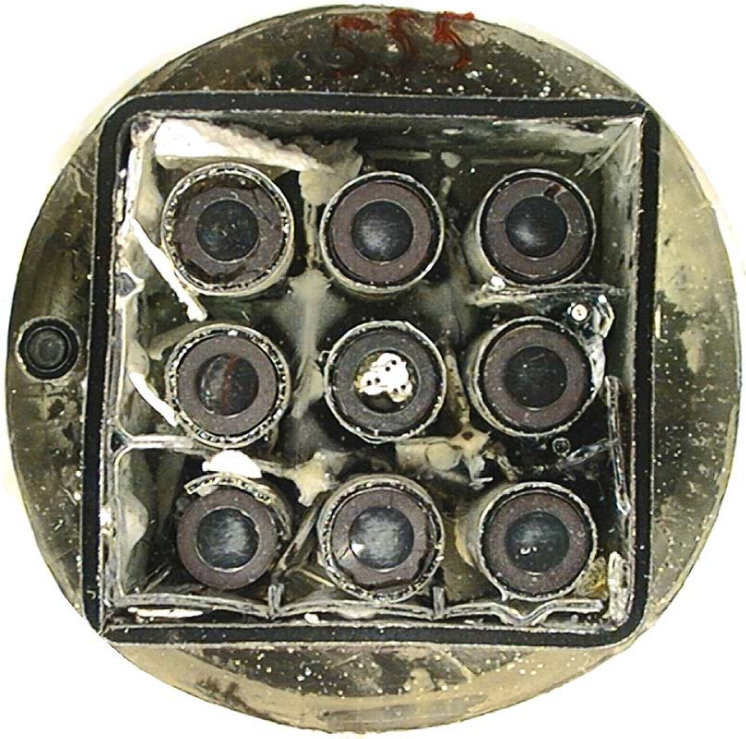

Fig. 65 Cross section of CODEX-AIT-1 bundle at 555 mm elevation

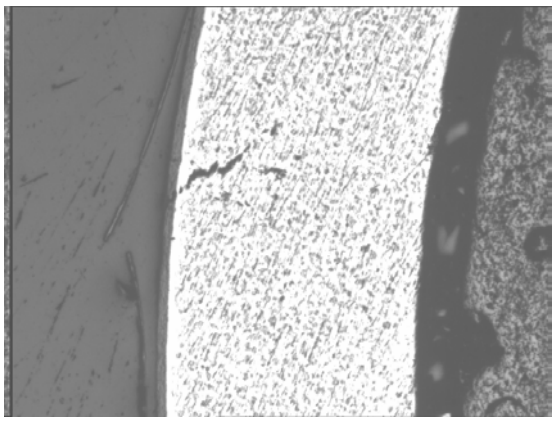

Fig. 66 View of cladding at 150 mm elevation

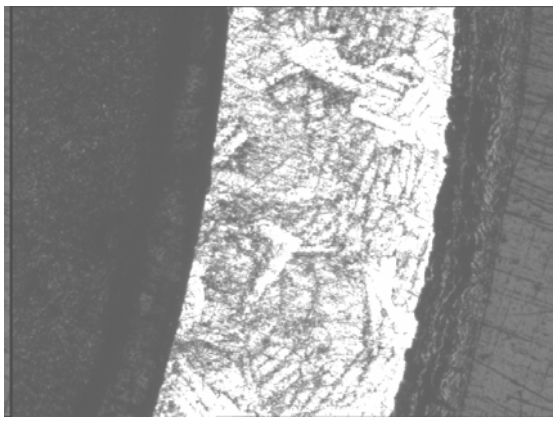

Fig. 67 View of cladding at 300 mm elevation

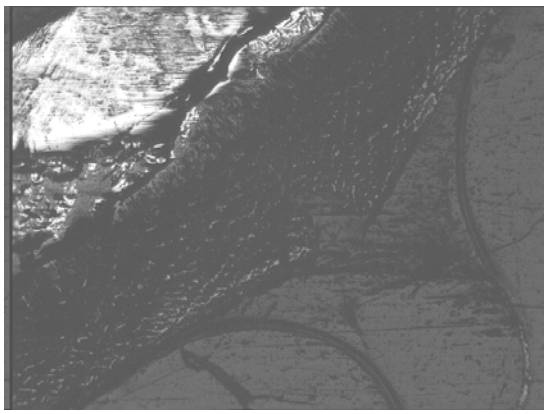

a,

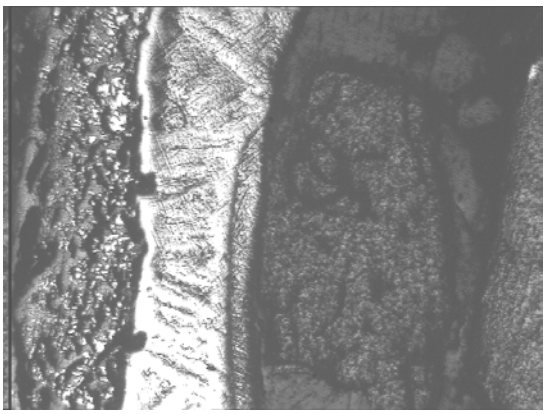

b,

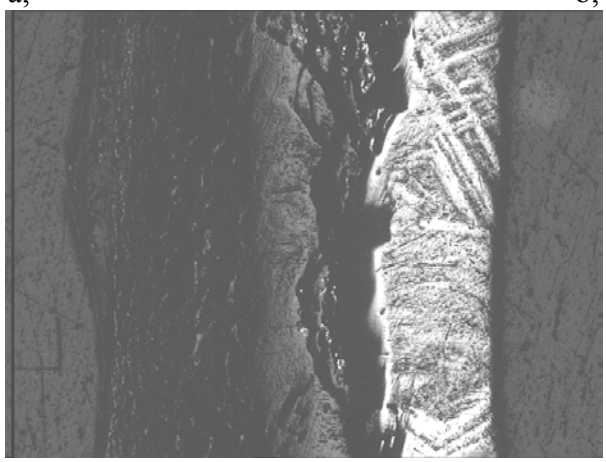

c,

Fig. 68 Cladding details of rod No.1 at 450 mm elevation

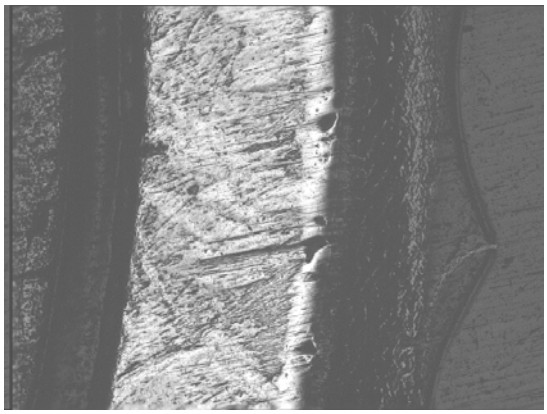

Fig. 69 Cladding of rod No.2 at 450 mm elevation

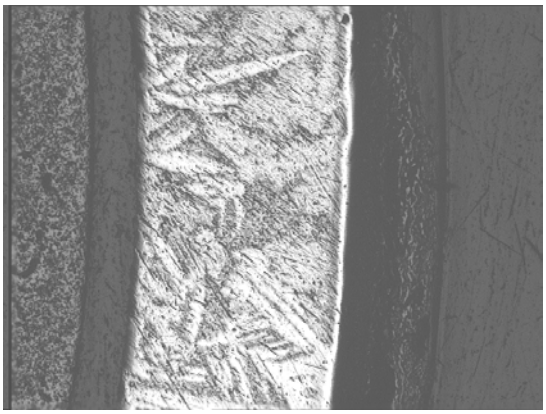

Fig. 70 Cladding of rod No.6 at 450 mm elevation

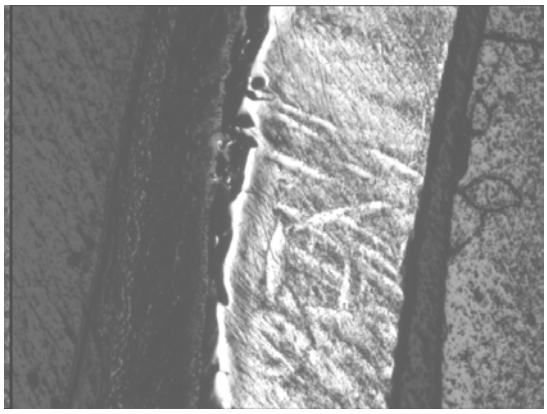

Fig. 71 Cladding of rod No.8 at 450 mm elevation

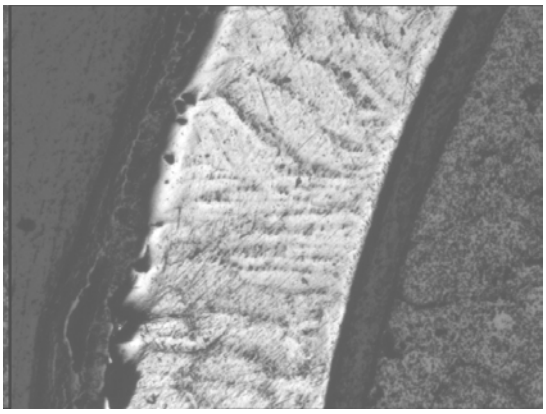

Fig. 72 Cladding of rod No.9 at 450 mm elevation

Fig. 73 Shroud and spacer at 450 mm elevation

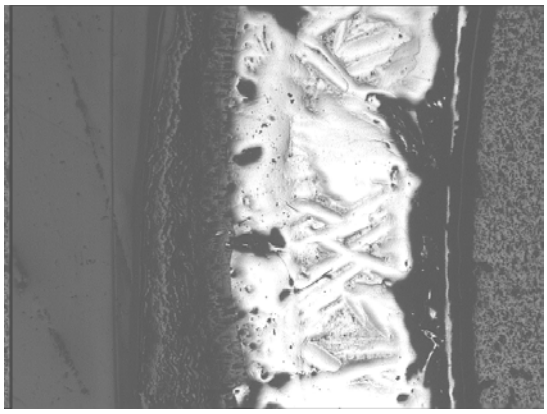

a,

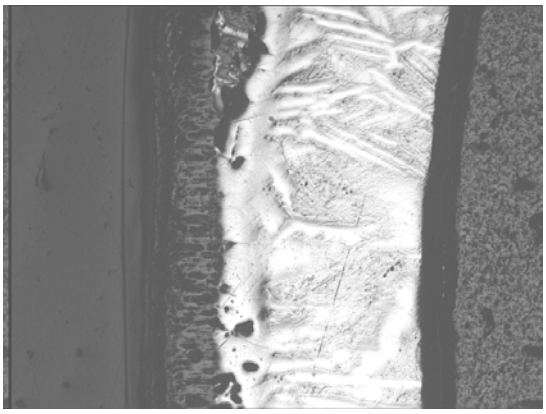

b,

Fig. 74 Cladding of rod No.2 at 535 mm elevation

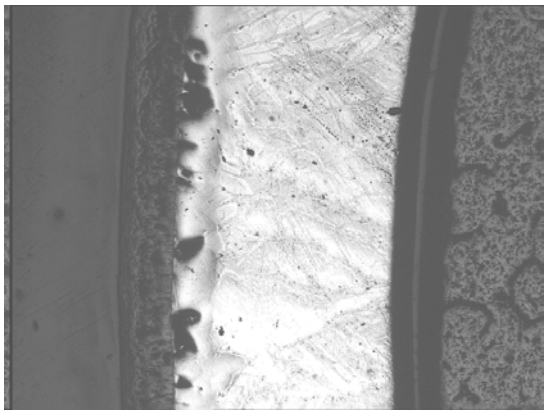

Fig. 75 Cladding of rod No.3 at 535 mm elevation

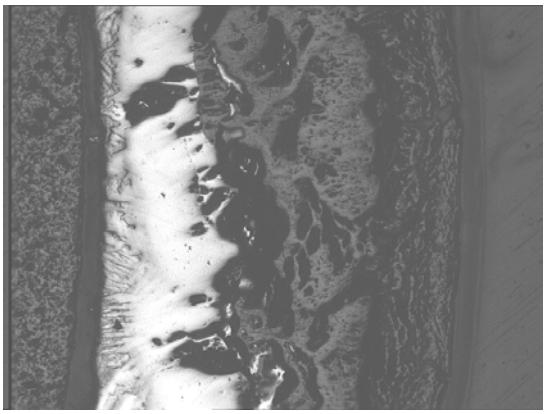

Fig. 76 Cladding of rod No.1 at 535 mm elevation

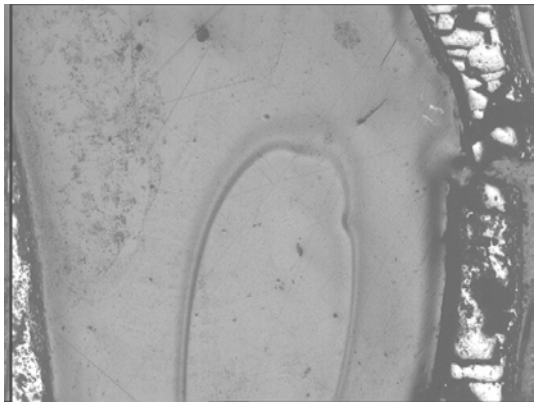

a.

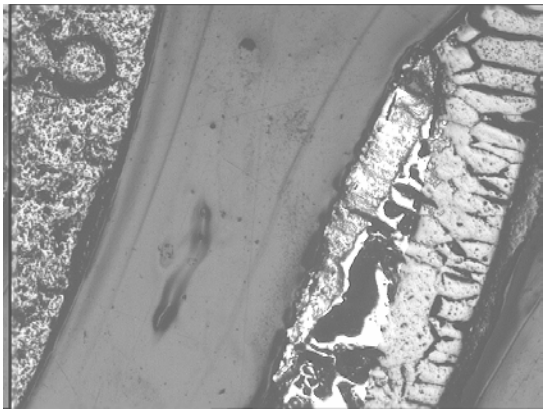

b.

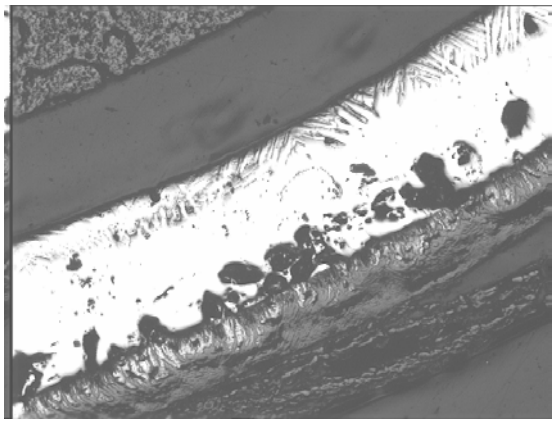

c.

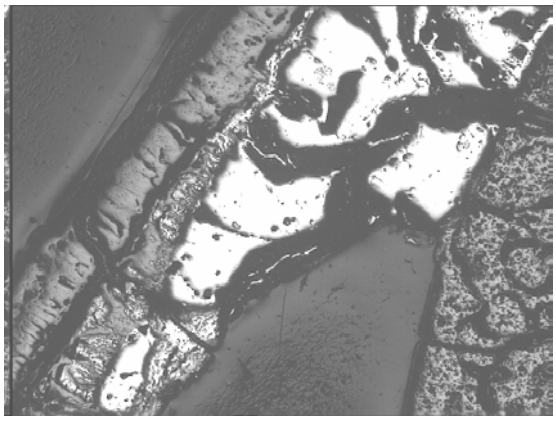

d.

Fig. 77 Cladding of rod No.4 at 535 mm elevation

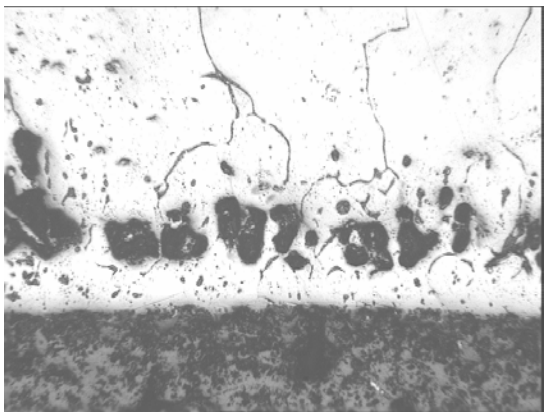

a,

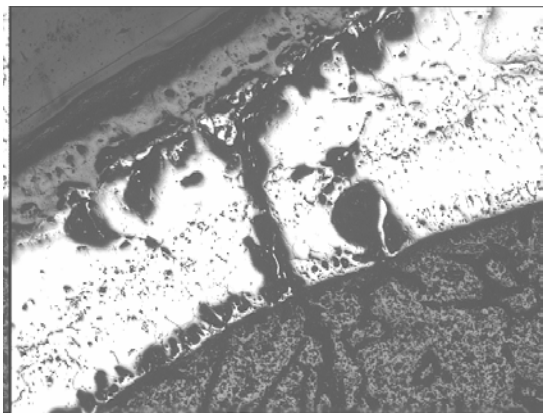

b,

Fig. 78 PCI intreactions in rod No.4 at 535 mm elevation

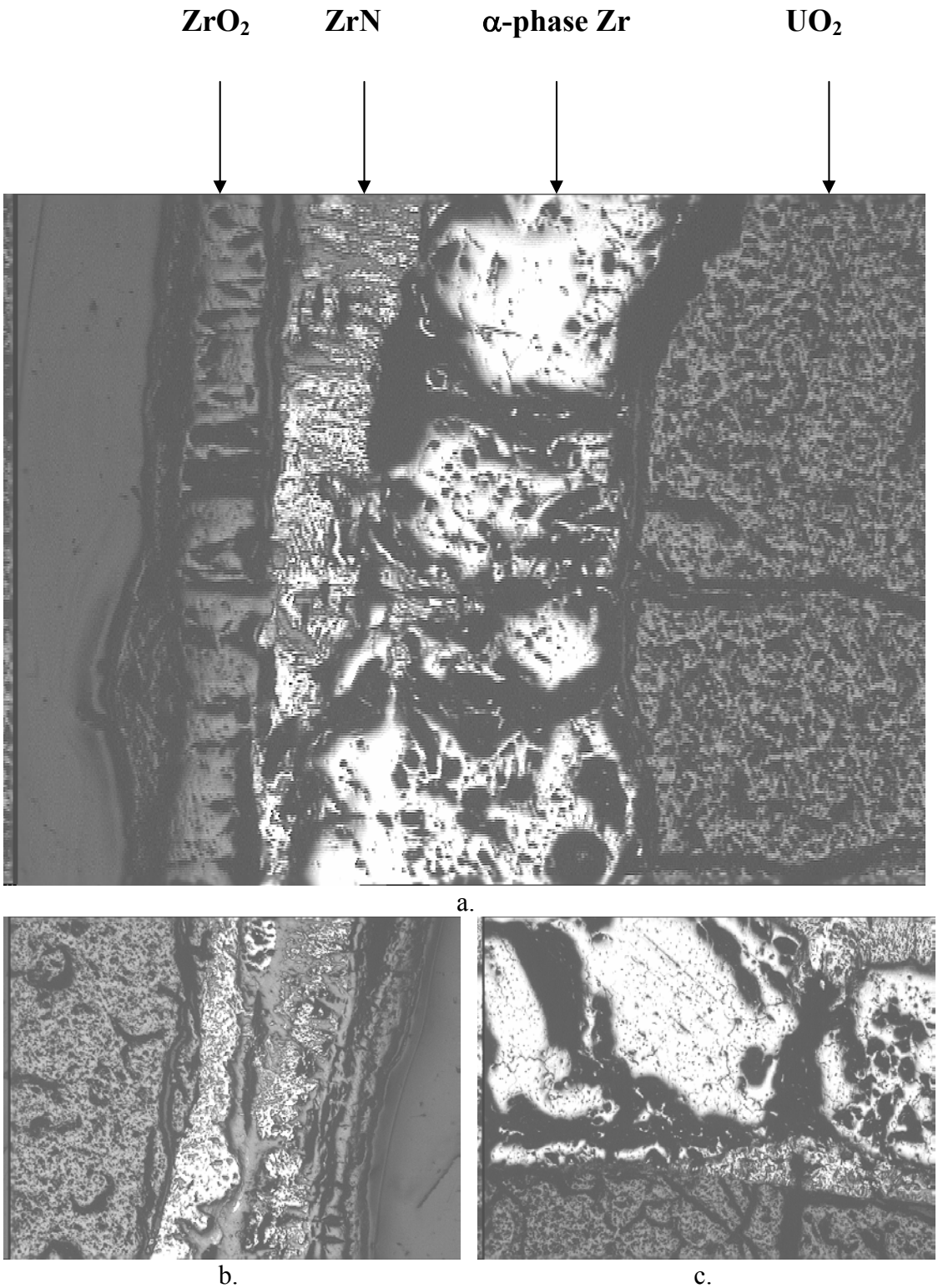

Fig. 79 Cladding and pellet on rod No.4 at 535 mm elevation

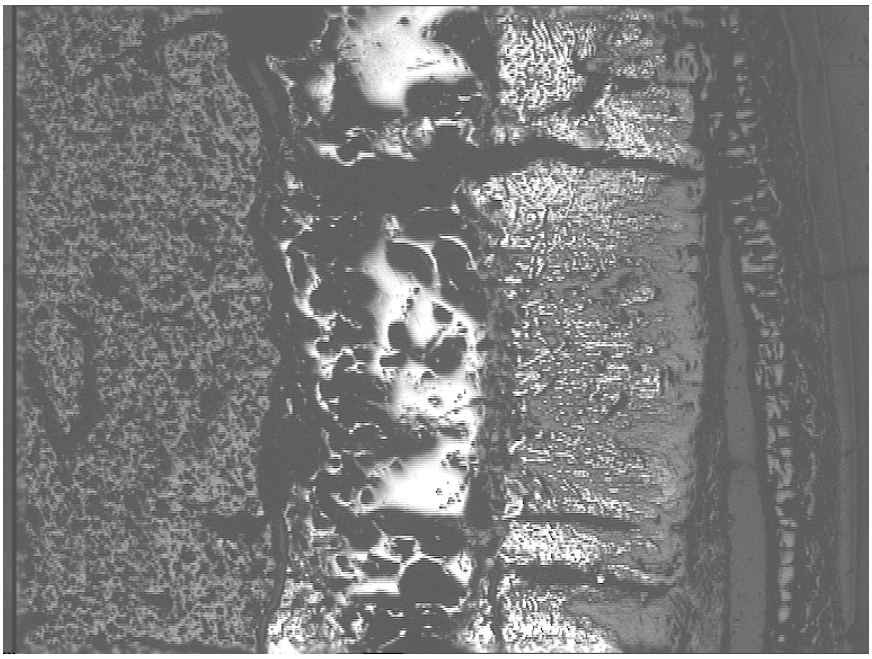

a,

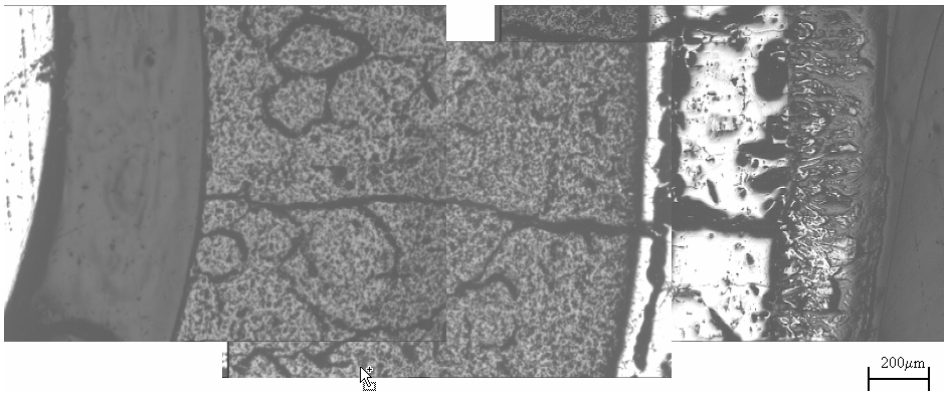

b,

Fig. 80 Cladding and pellet on rod No.6 at 535 mm elevation

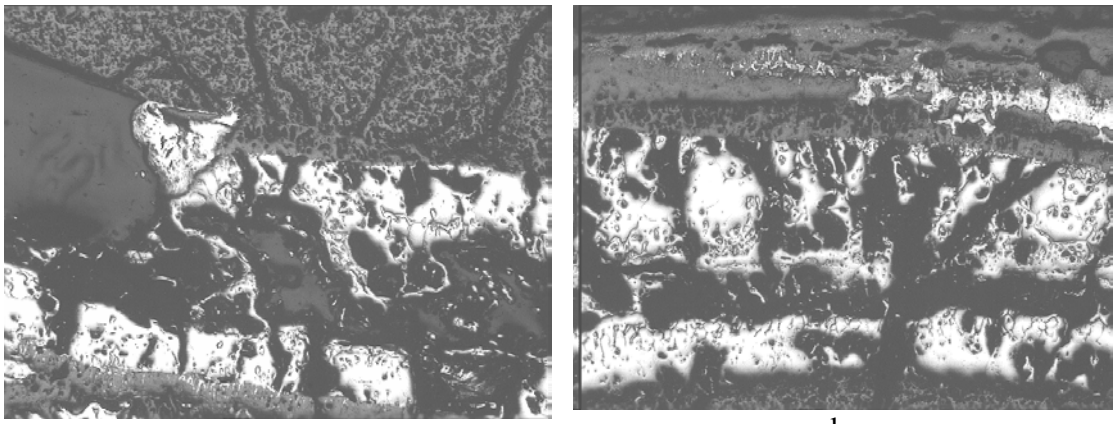

a, b,

Fig. 81 Cladding and pellet on rod No.7 at 535 mm elevation

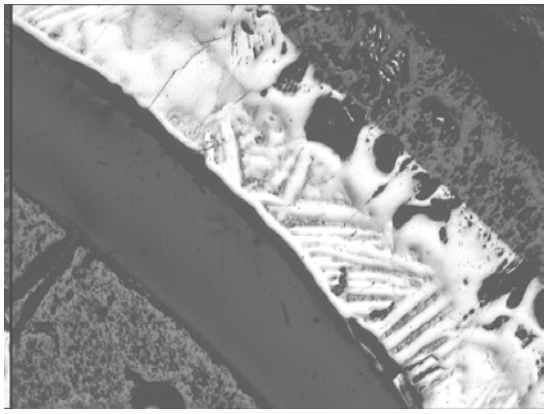

Fig. 82 Cladding of rod No.8 at 535 mm elevation

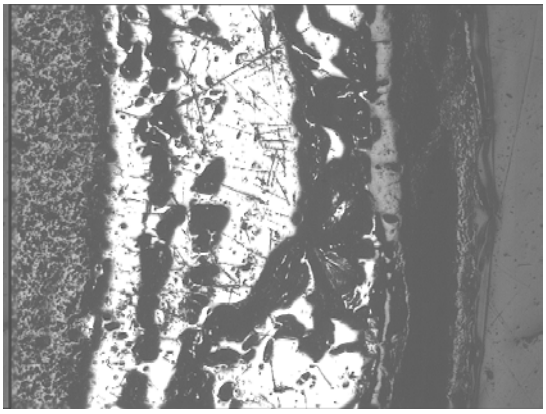

Fig. 83 Cladding of rod No.9 at 535 mm elevation

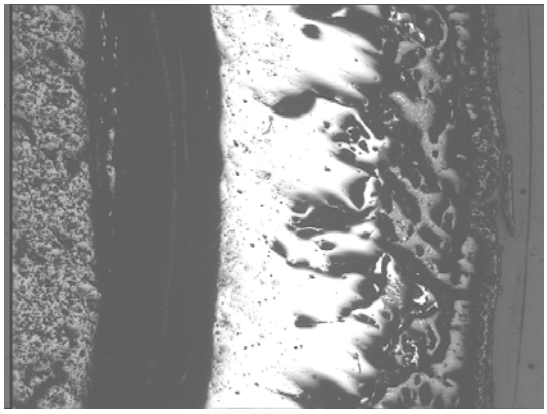

a,

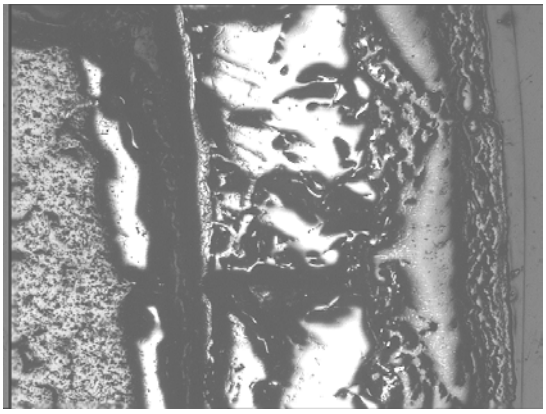

b,

Fig. 84 Cladding of rod No.1 at 555 mm elevation

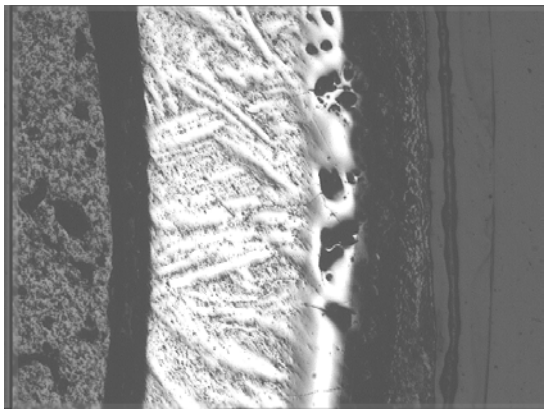

Fig. 85 Cladding of rod No.2 at 555 mm elevation

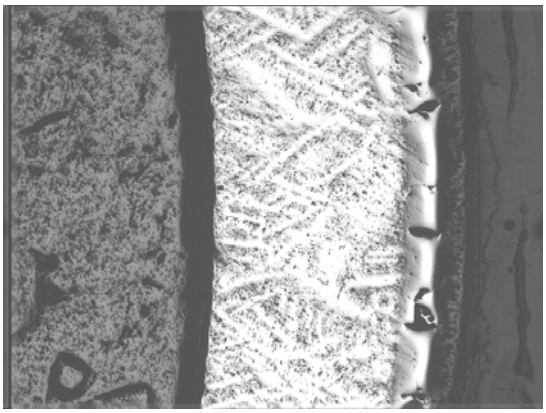

Fig. 86 Cladding of rod No.3 at 555 mm elevation

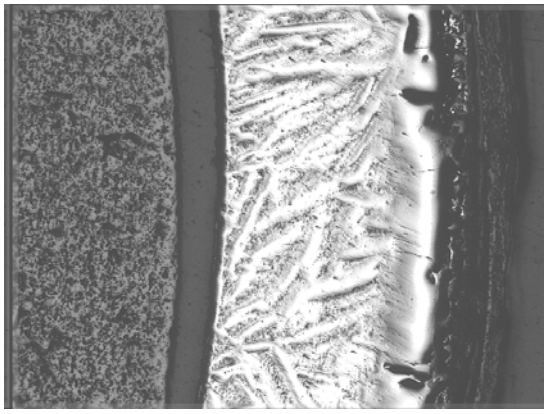

Fig. 87 Cladding of rod No.4 at 555 mm elevation

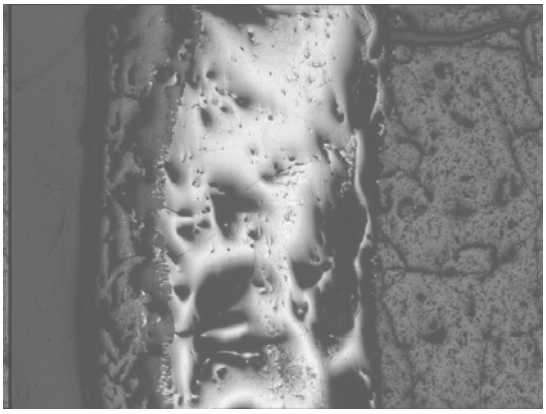

Fig. 88 Cladding of rod No.6 at 555 mm elevation

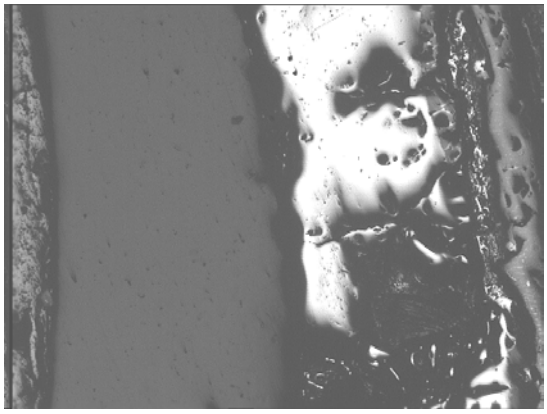

Fig. 89 Peeled off cladding of rod No.7 at 555 mm elevation

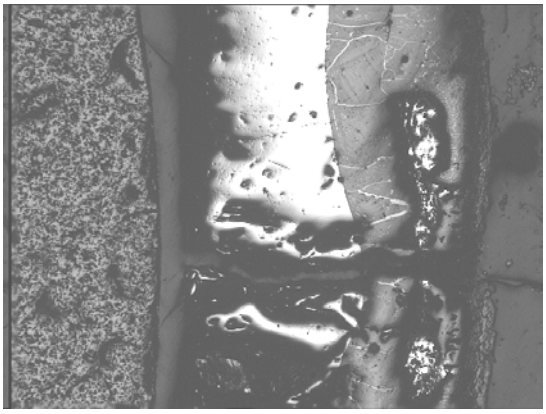

Fig. 90 Cladding of rod No.8 at 555 mm elevation

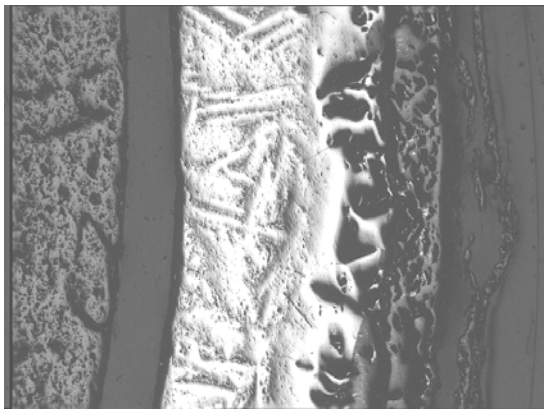

a,

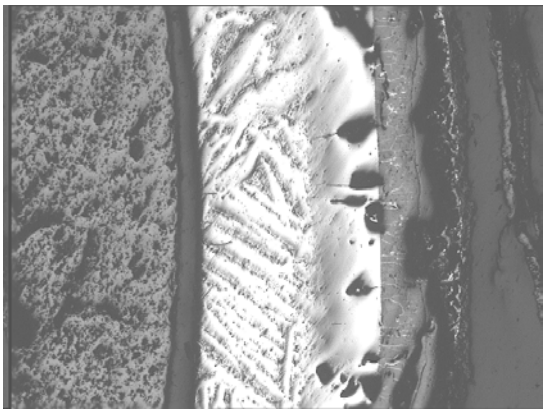

b,

Fig. 91 Cladding of rod No.9 (central) at 555 mm elevation

Elevation	Rod number								
[mm]	1	2	3	4	5	6	7	8	9
50	670.8	673.2	676.2	674.6	670.2	674.8	676.8	675.6	688.2
150	653.3	661.0	658.0	646.0	662.4	650.6	652.8	655.8	656.4
300	620.6	611.2	603.2	562.2	429.2	554.8	614.2	621.5	545
450	558.6	516.1	514.2	499.6	391.8	516.6	560.7	531.6	517.3
535	500.9	492.7	490.9	477.3				498.5	483.2
555								175	

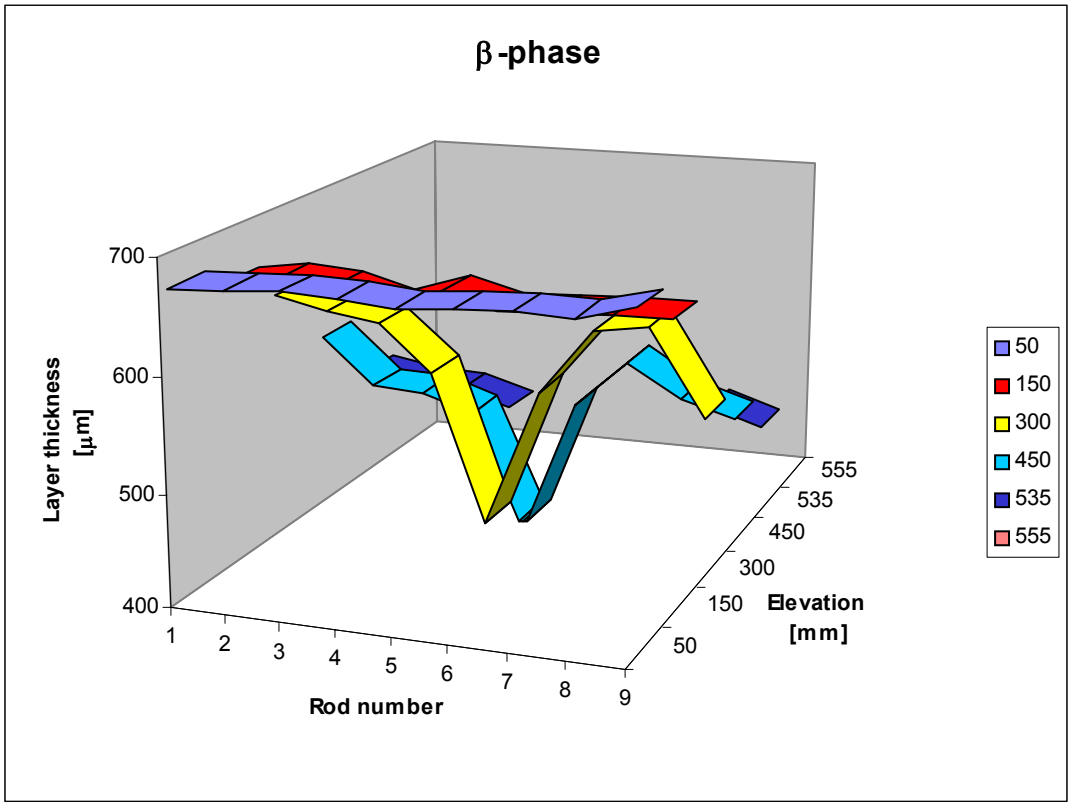

Fig. 92 β-phase axial distribution on the fuel rods

Elevation	Rod number								
[mm]	1	2	3	4	5	6	7	8	9
50	16.2	14.4	12.8	11	11	11.2	11.8	13.4	8.2
150	21	25.4	24.2	14.2	15	15.4	17	17.2	16.2
300	26.8	22.6	23	22	29.8	20.4	12	14.7	12.6
450	35.2	35.1	75.4	42.0	54.8	39.7	28.9	51.1	40.5
535	270.5	95.9	86.0	275.0	543.5	353.4	357.9	205.1	400.8
555	372.6	136.5	98.0	150.2	169.5	362.6	406.6	368.9	209.3

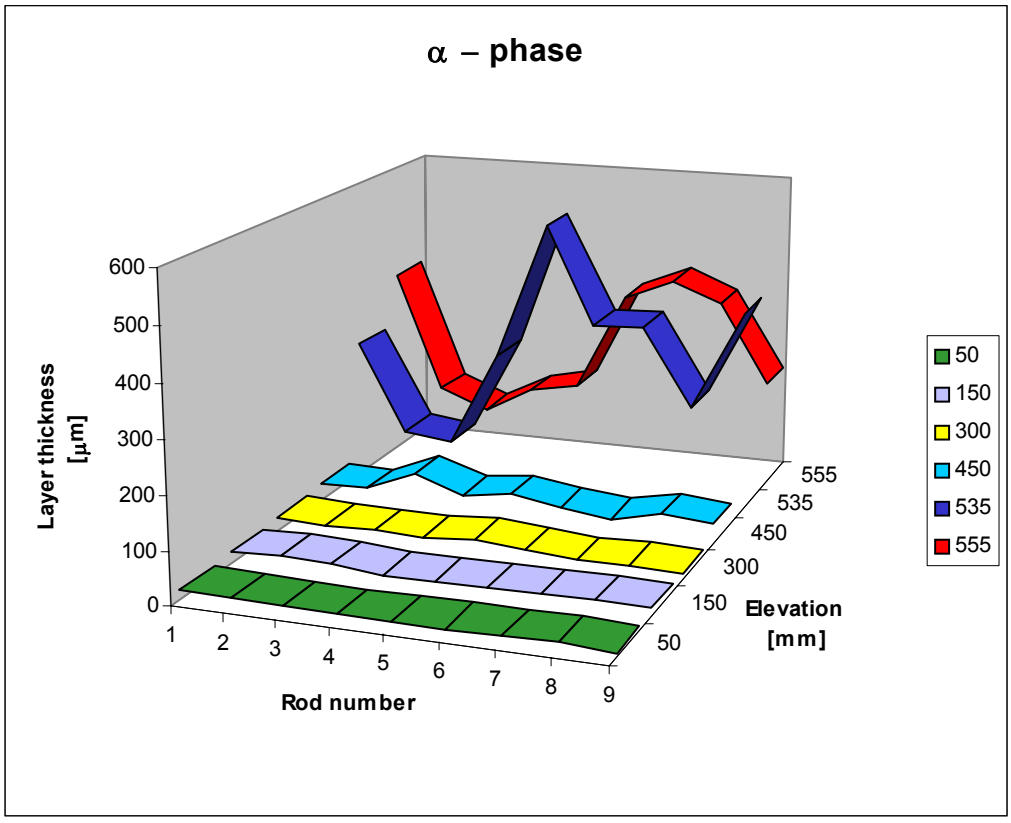

Fig. 93 α phase axial distribution on the fuel rods

Elevation	Rod number								
[mm]	1	2	3	4	5	6	7	8	9
50	13	12.4	11	14.4	18.8	14	11.4	11	3.6
150	25.7	13.6	17.8	39.8	22.6	34.0	30.2	27.0	27.4
300	52.6	66.2	73.8	115.8	241	124.8	73.8	63.8	142.4
450	106.2	148.7	110.4	158.4	253.4	143.7	110.4	117.3	142.2
535	515.4	215.7	106.3	180.3	201.6	105.0	223.9	240.7	191.9
555	293.4	210.6	86.8	96.8	218.5	195.3	301.5	278.3	235.7

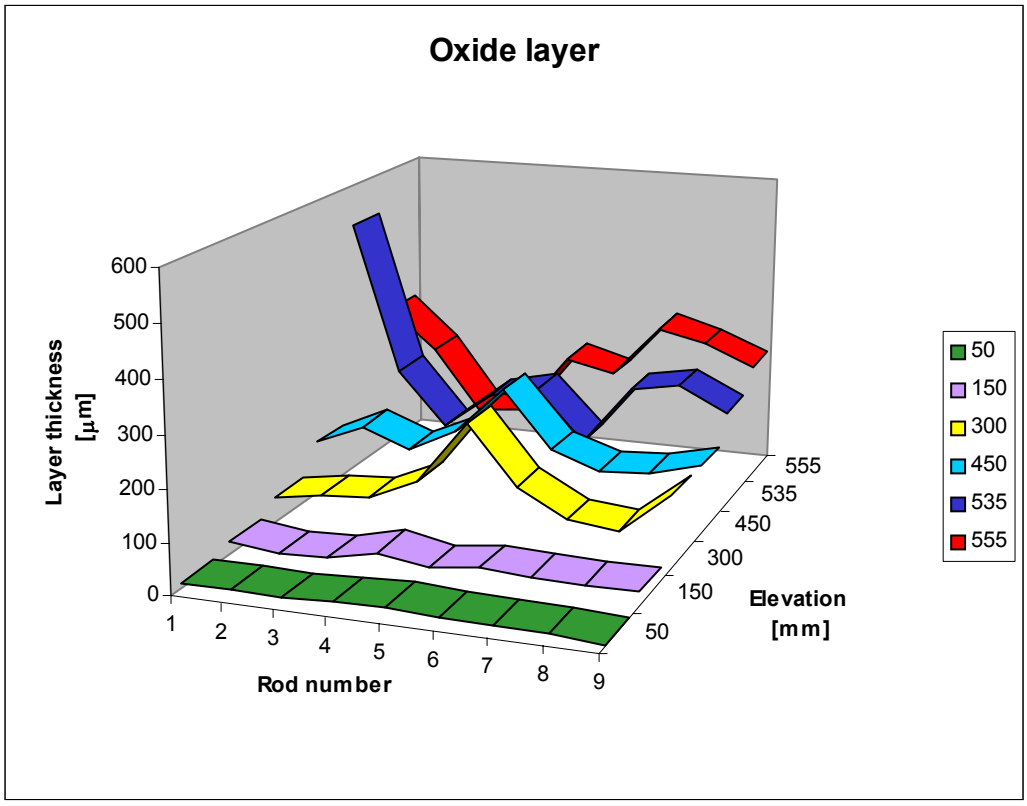

Fig. 94 Oxide layer axial distribution on the fuel rods

Elevation	Rod number								
[mm]	1	2	3	4	5	6	7	8	9
50									
150									
300									
450				167.5	291.6	100.3			89.8
535		174.3	71.4	90.0	147.8	235.2	190.0	222.4	
555							48.5		

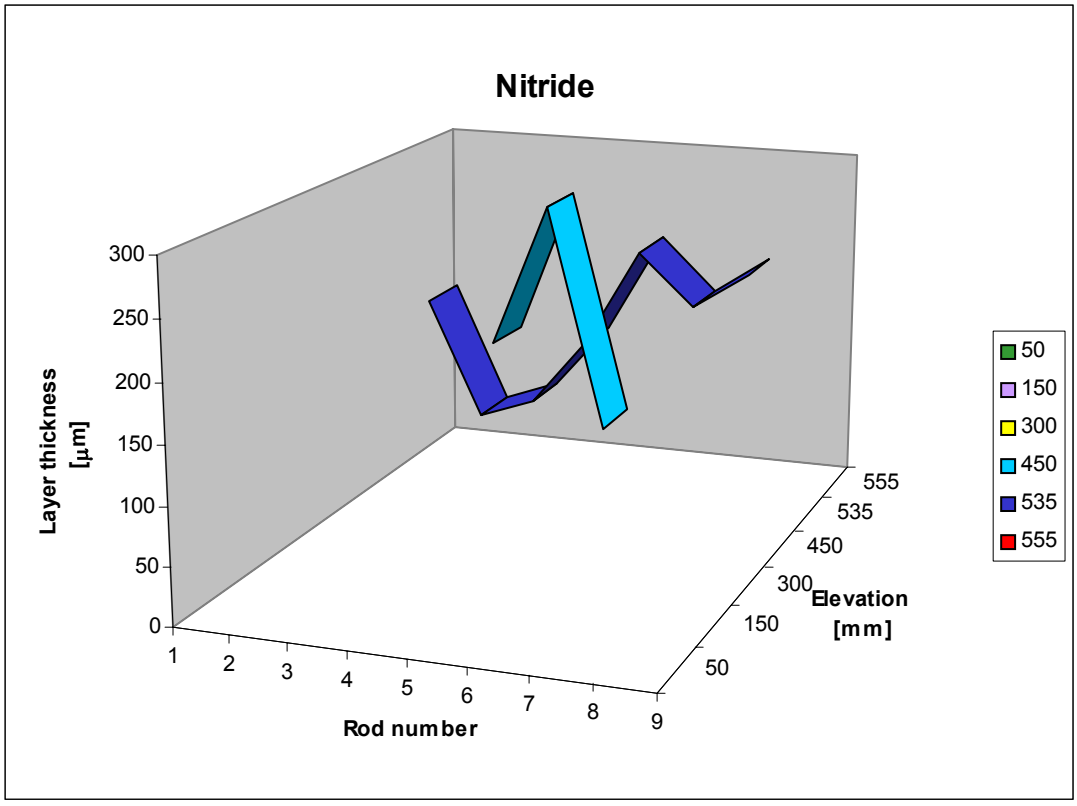

Fig. 95 Nitride layer axial distribution on the fuel rods

	Elevation[mm]	Rod number								
		1	2	3	4	5	6	7	8	9
α-phase	50									
	150									
	300									
	450									
	535				83.3	83.6	66.2	131.2		106.3
	555						100	20		
α-phase	50									
	150									
	300									
	450									
	535					51.6	53.5	122.8		69.3
	555						19	15		

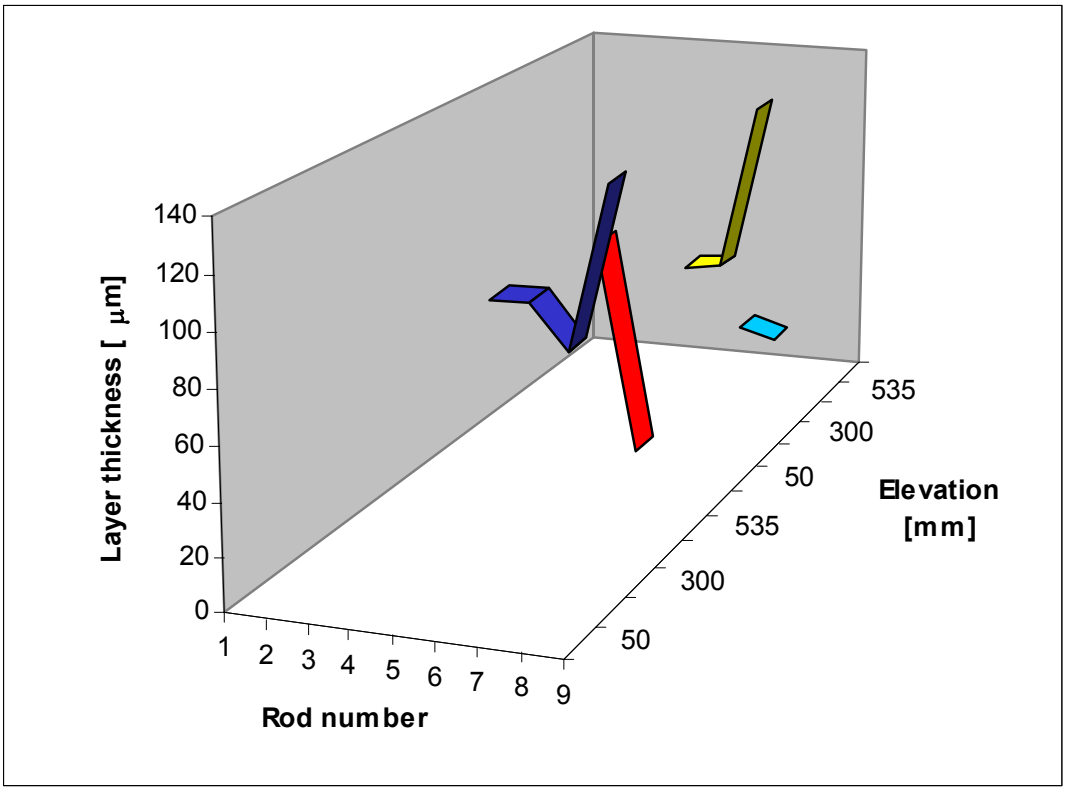

Fig. 96 Pellet-cladding interaction layer thickness
axial distribution on the fuel rods (α-phase at UO_2 side and α-phase at β layer side)

Elevation	oxide		α-phase		nitride	
[mm]	oxide outside	oxide inside	α-phase outside	α-phase inside		
50	10.8		6.8	6.4		
150	17.6	22.6	8.6	13.4		
300	11	64.4	43.2	11.2		
450	82.4	144.0	42.4	40.9		
535	50.4	96.9	124.3	116.7	120.4	118.9
555	100.2	115.2	115.8	130.2		

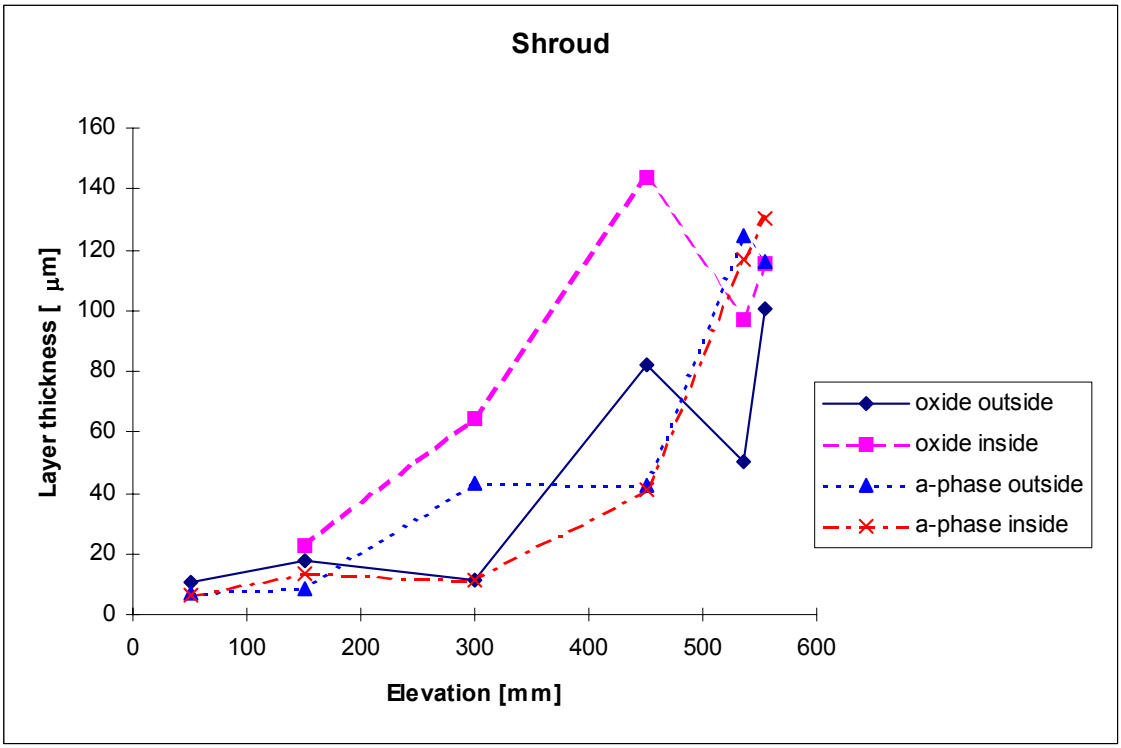

Fig. 97 Oxide, α-phase and nitride layer thickness on the shroud

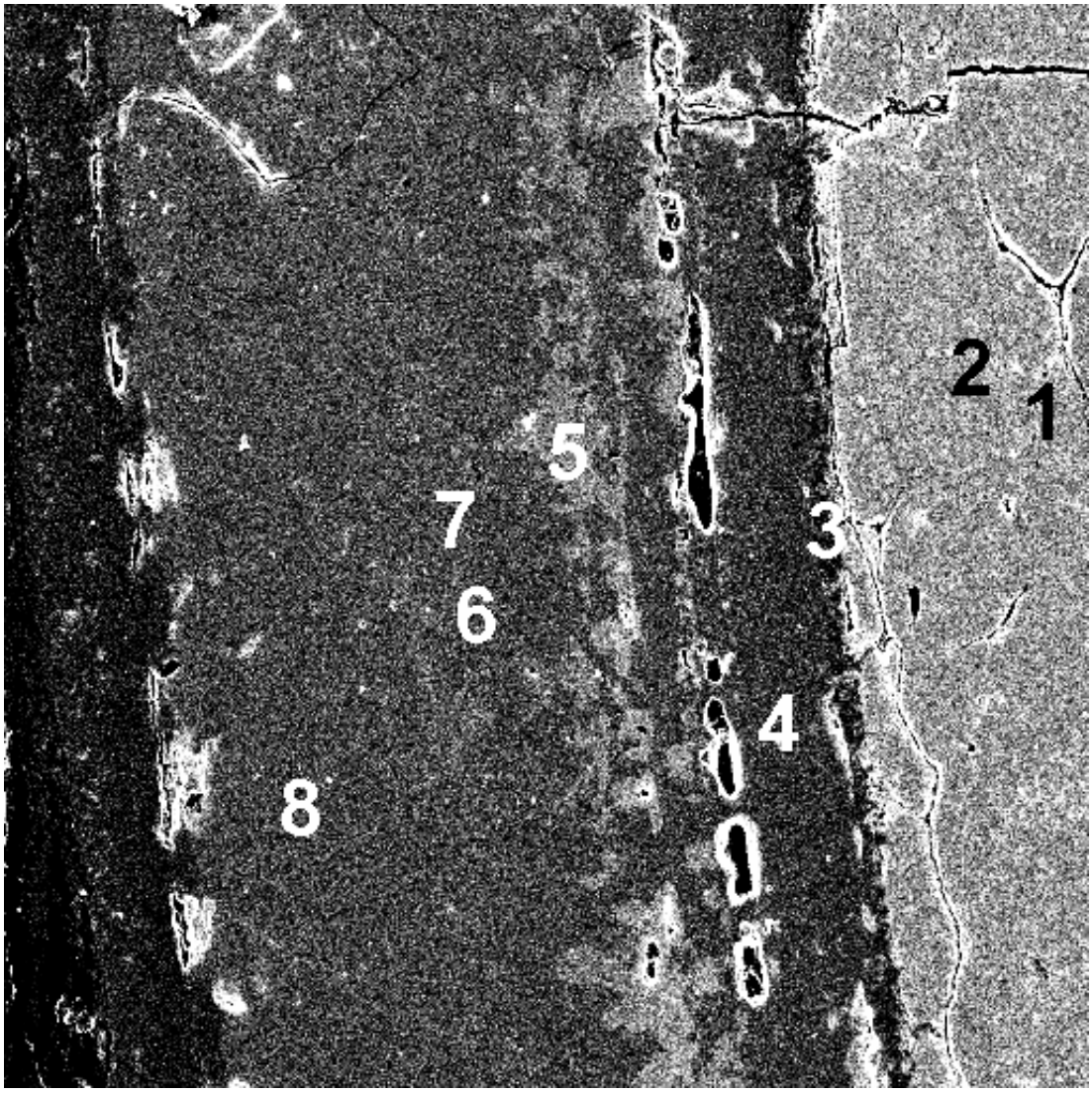

Fig. 98 Interaction of UO_2 with Zircaloy cladding
The above positions refers to EDS investigation (Table 1) :

- Positions No. 1 and 2. are in the UO_2 pellet
- Positions No. 3-5 are in the interaction layers
- Positions No.6 and 7 are in U-rich phases
- Position No. 8 is in the cladding

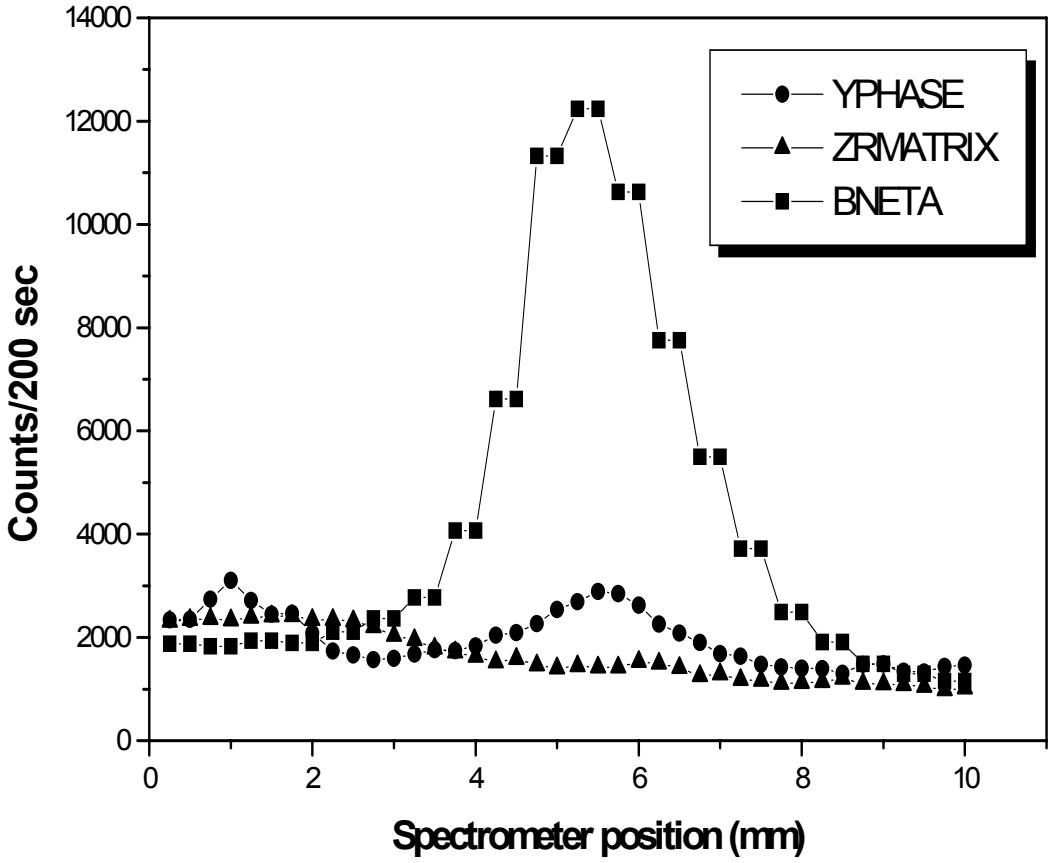

Fig. 99 Nitrogen K alfa X-ray line profiles
measured for the zirconium nitride,
compared with that of the Zr matrix and of the BN standard

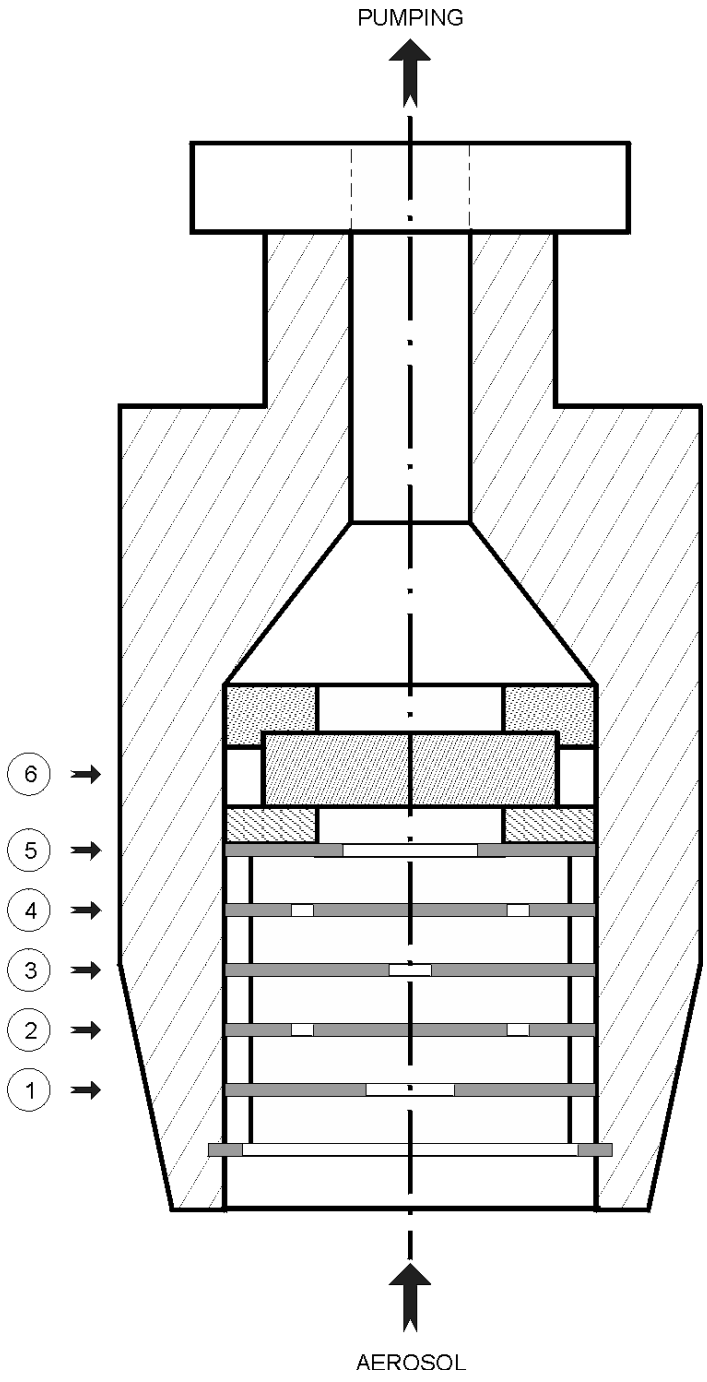

Fig. 100 Scheme of impactor sampler
1. 1st nozzle
2. 1st collector (sample B)
3. 2nd nozzle
4. 2nd collector (sample D)
5. stream limiter
6. quartz fibre filter

CODEX - AIT - 1.

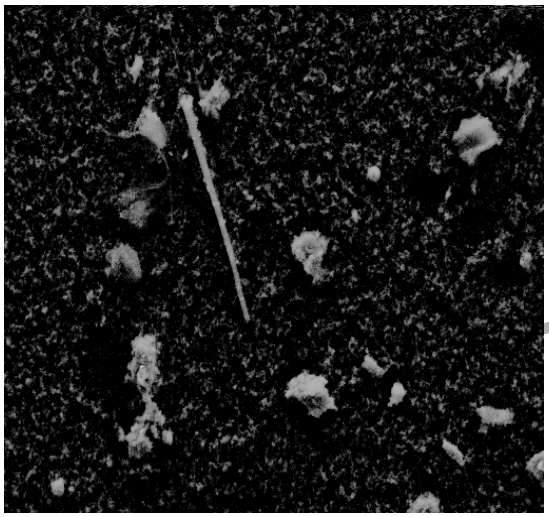

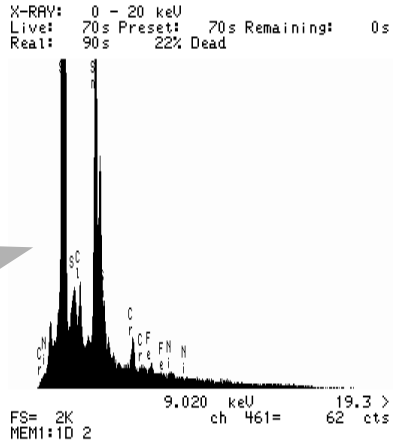

10 μm

SEI image

Small particles: Sn - rich

a few: U-rich

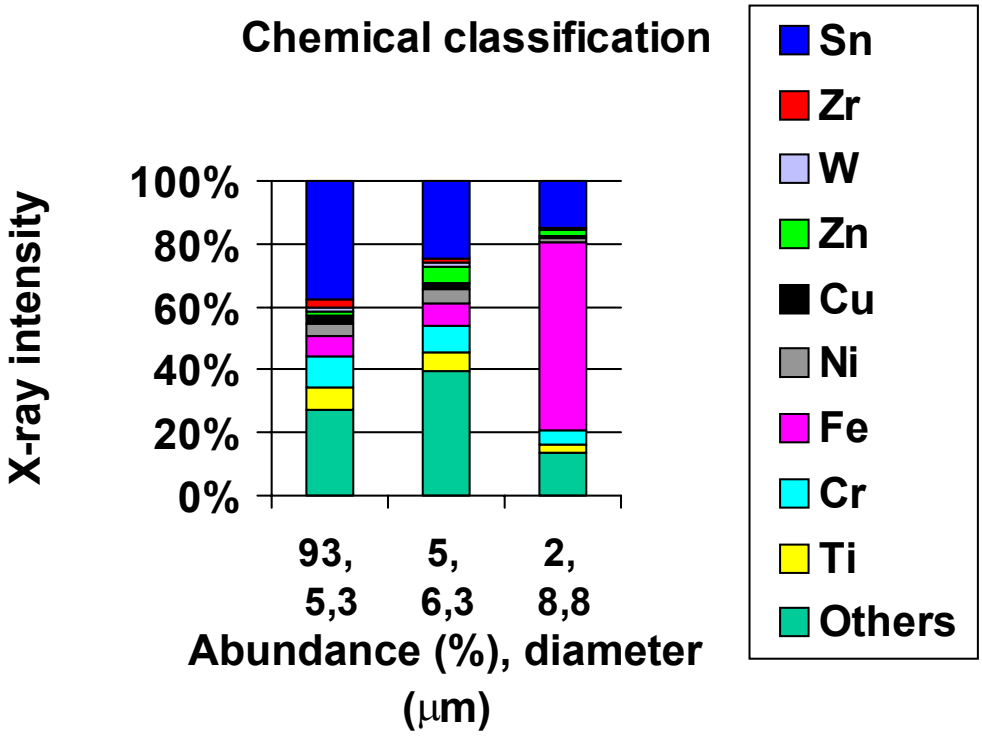

Fig. 101 SEM image, ED spectra
and chemical classification of sample No. 1B

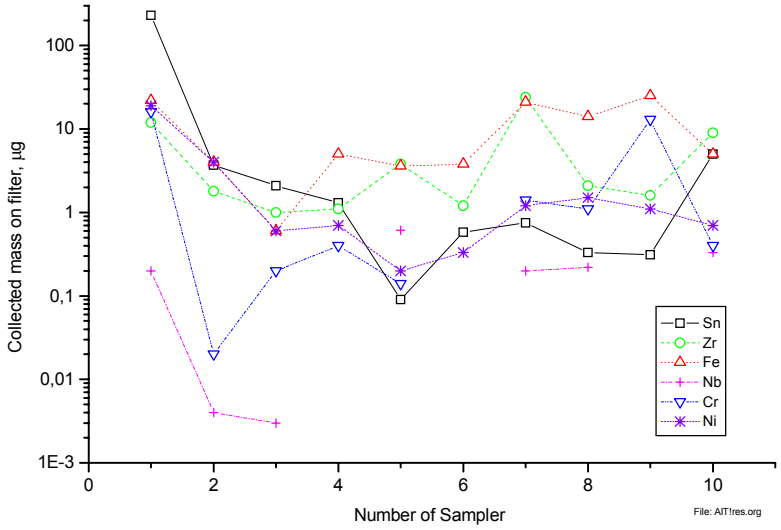

Fig. 102 Amount of some collected elements
on sampling filters after 1 litre gas flow in the CODEX-AIT-1 test

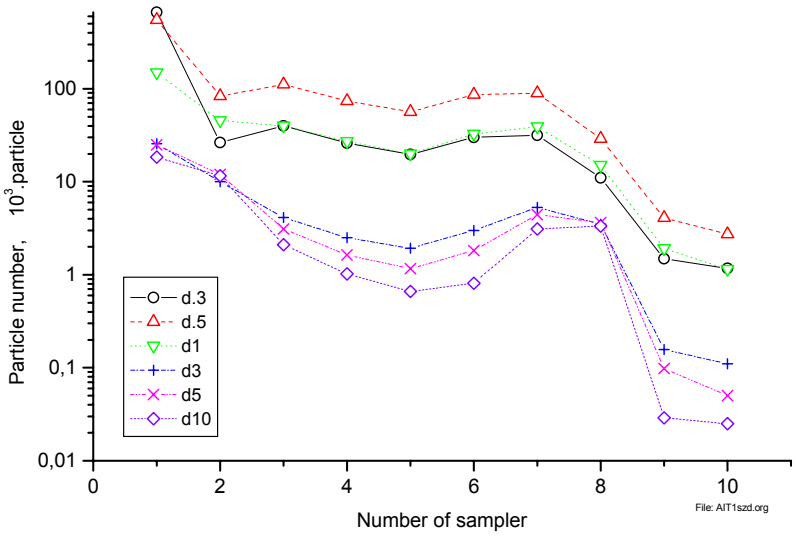

Fig. 103 Number of particles during sampling
for diameters of 0.3-0.5(d.3), 0.5-1.0(d.5), 1-3(d1), 3-5(d5), 5-10(d5) and >10(d10) μ m in the CODEX-AIT-1 test